UC Riverside
UC Riverside Electronic Theses and Dissertations

Title
Towards Magneto-Logic Gates in Graphene

Permalink
https://escholarship.org/uc/item/8x3346b7

Author
Wen, Hua

Publication Date
2014

Peer reviewed|Thesis/dissertation

eScholarship.org Powered by the California Digital Library
University of California

UNIVERSITY OF CALIFORNIA
RIVERSIDE

Towards Magneto-Logic Gates in Graphene

A Dissertation submitted in partial satisfaction
of the requirements for the degree of

Doctor of Philosophy

in

Physics

by

Hua Wen

December 2014

Dissertation Committee:

Dr. Roland K. Kawakami , Chairperson
Dr. Jing Shi
Dr. Vivek Aji

Copyright by
Hua Wen
2014

The Dissertation of Hua Wen is approved:

Committee Chairperson

University of California, Riverside

Acknowledgments

While there are many people who have helped me during the adventure of my pursuing Ph. D degree, I want to express my special thanks to my advisor, Dr. Roland Kenji Kawakami for offering me an great opportunity in performing memorable research in his lab since 2010. I was introduced into the world class researches and researchers ever since. I admire the ability to always keep energetic and excited about research that Roland has been showing to me, no matter how many hurdles are lying in the way of research. This has greatly changed my view point about how to choose the things that you really want to do. I really appreciate the fact that Roland is always available when any problem came up. Well, this is how to get things done. Without you, Roland, I would have not been here.

I would like to thank Wei Han, Kathy McCreamy and Adrian Swartz who have taught me bolts and nuts in the lab and led me into the wonderland of research. I also thank Jared Wong, Patrick Odenthal, Walid Amamou, Dante OHara, Jenru Chen, Renjing Zheng and Igor Pinchuk for enjoyable days working in Riverside which is nice and warm. In the chilling Columbus I am lucky to be working with wonderful people such as Tiancong Zhu, Andy Berger, Jyoti Katoch, Adam Ahmed, Kelly Luo and Beth Bushong. Because of you, the cold days doesn't seems so cold anymore.

Thank you my friends in Riverside, Peng Wang, Bin Cheng, Tengfei Miao, Fengling Wang, Lingli Wang, Jian Huang, Dong Gui, Xiaoxiao He, etc that makes the journey to PhD to be filled with joy.

Last but not the least, I greatly appreciate the accompanying of my wife, Xinjie Yang, who has chose to devote the most precious time of her life with me. Without you, life would have been much harder. Also I greatly appreciate my parents who are visibly aging each year. Please forgive me for the so few times I have spent to payback what I own you.

To my parents.

ABSTRACT OF THE DISSERTATION

Towards Magneto-Logic Gates in Graphene

by

Hua Wen

Doctor of Philosophy, Graduate Program in Physics
University of California, Riverside, December 2014
Dr. Roland K. Kawakami , Chairperson

Spintronics utilizes electron spin degree of freedom for novel information storage and processing beyond. The key components in spintronics include creating, manipulating and detecting spins in a spin transport channel. Single layer graphene has emerged as the leading candidate for spin transport materials due to experimentally observed high mobility, long spin lifetimes and long spin diffusion lengths at room temperature. A nonvolatile, reconfigurable universal magneto-logic gate has been proposed based on the excellent spin transport properties of graphene. Integration of these logic gates can operate at high speed and consume less power in parallel data processing applications. This thesis is trying to experimentally implement this magneto-logic gate using state-of-art lateral graphene spin valves. Firstly, current-based detection of spin transport in graphene was demonstrated in graphene spin valve. This is important because the logic output of magneto-logic gate is a current signal which depends on spin accumulation in graphene. Secondly, bias dependent spin injection in graphene was studied. Spin injection across MgO tunnel barrier was found to strongly depend on the injection bias. Thirdly, by utilizing the observed bias dependence, XOR logic operation was successfully demonstrated in graphene devices with three ferromagnetic electrodes. This provides an important step forwards towards fully demonstration of the proposed five terminal magneto-logic gate. Lastly,

successful spin injection and transport in epitaxy large area graphene was achieved. This indicates that large area graphene can be potentially used for large devices integration.

Contents

List of Figures **x**

1 Introduction **1**

1.1 Spintronics . . . 1
1.2 Graphene . . . 8
1.3 Graphene Spintronics . . . 13
1.4 Motivation and Outline . . . 18

2 Magneto-Logic Gate in Graphene **20**

2.1 Introduction . . . 20
2.2 Working Principle . . . 21
2.3 Challenges and Approaches . . . 24

3 Devices Fabrication and Transport Measurement **27**

3.1 Graphene Spin Valves Fabrication . . . 27
3.2 Electrical Measurement Setup . . . 35
3.3 Device Measurement Methodology . . . 37
3.4 Hanle Fitting . . . 42
3.5 Some Notes on Graphene Spin Valves . . . 43
3.5.1 DC and AC measurement . . . 43
3.5.2 Contact effect in graphene . . . 45
3.5.3 Graphene device cleaning . . . 45
3.5.4 MIBK vs IPA developer . . . 46

4 Current Detection of Spin Transport in Single Layer Graphene **48**

4.1 Introduction . . . 48
4.2 Experimental Results . . . 49
4.3 Theoretical Analysis . . . 53
4.3.1 Calculate spin and charge current inside channel N . . . 55
4.3.2 Calculate spin and charge current inside FM . . . 56
4.3.3 Interfacial charge and spin current . . . 57
4.3.4 Continuity conditions . . . 58
4.4 Device Optimization . . . 61
4.5 Conclusion . . . 63

5 Bias Dependence of Spin Injection in Graphene **64**
5.1 Introduction 64
5.2 Experimental Methods 65
5.3 Bias Dependence of Spin injection 66
5.4 Possible Explanation 68
5.5 Conclusion 70

6 XOR Logic Operation in Graphene **71**
6.1 Introduction 71
6.2 Logic Operation 71
6.3 Input Balancing 76
6.4 Voltage Offset 78
6.5 XOR Logic Using Current Detection 79
6.6 Frequency Dependence 82
6.7 Confined Device 82
6.8 Conclusion 86

7 Spin Transport in Large Area Graphene **87**
7.1 Introduction 87
7.2 Growth of Large Area CVD graphene 89
7.2.1 Copper foil preparation 89
7.2.2 Growth setup 90
7.3 Transfer 93
7.4 Graphene Spin Valves Fabrication 95
7.5 Spin Valve Measurement 97
7.6 Conclusion 98

8 Conclusions **99**

Bibliography **101**

List of Figures

1.1 Density of state of FM and NM around Fermi level (E_F) 2
1.2 GMR effect and qualitative model 3
1.3 Propose of spin-FET device 4
1.4 Propose of magneto-logic gate device 4
1.5 Lateral spin valve device 5
1.6 Electrical spin injection and detection in metal lateral nonlocal spin valve . . . 6
1.7 Spin precession in a perpendicular magnetic field 7
1.8 Lattice and band structure of graphene 9
1.9 Quantum Hall effect in graphene at T = 4 K 10
1.10 Spatial density fluctuations and electron-hole puddles 11
1.11 AFM image of a graphene on hBN device 12
1.12 Large area, single layer graphene grown on copper foil 13
1.13 Room temperature spin injection and detection in graphene 14
1.14 Growth of atomical smooth MgO for tunneling spin injection into graphene . . 15
1.15 Linear scale of spin relaxation time and momentum scattering time 17
1.16 Spin lifetime τ_s as a function of metal deposition on top of graphene 17

2.1 Universal and reconfigurable magneto-logic gate in graphene 21
2.2 Spin density of parallel and antiparallel configurations 23
2.3 Transient current across the middle readout electrode M 24

3.1 Exfoliation of graphene onto SiO_2 substrate 28
3.2 Optical image of the device after each metal deposition step 30
3.3 Diagram showing metal deposition steps 31
3.4 Angle deposition of MgO tunnel barrier in MBE chamber 33
3.5 Optical and MFM image of a graphene spin valve device 34
3.6 Magneto-transport measurement setup 36
3.7 Equipment setup for nonlocal spin transport measurement 38
3.8 Diagram of different measurement setup 39
3.9 Graphene spin valve properties at room temperature 41
3.10 Comparision of the two Hanle fitting results on the data 43
3.11 Some aspects about graphene spin valve measurement 44
3.12 AFM image of a graphene device 46
3.13 AFM image of a graphene after MIBK and IPA development 47

4.1 Nonlocal spin valve measurement 50
4.2 Nonlocal measurement with a variable sensing resistor R_{sense} 51

4.3 Voltage and current detection signal as a function of R_{sense} 52
4.4 Structure of spin injection and detection in a nonmagnetic channel 54
4.5 Model fit to the data 60
4.6 Simulated current signal ΔI_{NL} as a function of device parameters 62

5.1 Schematic diagram of the device and nonlocal spin transport measurement. . . 66
5.2 Spin transport measurement at different bias 67
5.3 Nonlocal signal at different bias current and gate voltages for Device A 68
5.4 Nonlocal signal at different bias current and gate voltages for Device B 69

6.1 Device structure and SEM image 72
6.2 Contacts and graphene resistance. 73
6.3 Nonlocal voltage signal for two inputs 74
6.4 Minor loop for logic operation 75
6.5 Minor loop at different gate voltages and bias current for Device C 77
6.6 Minor loop at different bias current for Device D 77
6.7 Diagram of using offset voltage source in the detection loop 79
6.8 ΔV_{sense} and ΔI_{out} as a function of R_{sense} 80
6.9 XOR logic operation 80
6.10 Repeated scans of V_{sense} as a function of magnetic field 81
6.11 Measured ΔI_{out} as a function of AC current frequency 82
6.12 Diagram of using Ar^+ to etch away graphene 83
6.13 Ar^+ sputtering at different energy 84
6.14 Ar^+ sputtering for different time 85

7.1 Growth mechanism for graphene on copper foil 88
7.2 Setup for CVD graphene growth 90
7.3 Equipments for our CVD graphene growth 91
7.4 Growth recipe for our CVD graphene 92
7.5 SEM image of copper foil and grown graphene on top 93
7.6 Transfer of as-grown graphene to SiO_2 substrate 94
7.7 Raman spectra for transferred graphene on SiO_2 95
7.8 Etch down LAG for device fabrication 96
7.9 Fabricated LAG spin valves 97
7.10 Nonlocal spin transport signal on the device 98

Chapter 1

Introduction

This chapter introduces the fundamental concepts for spintronics and graphene. with a focus on graphene spintronics. In the end the outline of this thesis is given.

1.1 Spintronics

Spin electronics, or spintronics, manipulate the intrinsic spin of electrons for electronic applications in solid-state devices[1, 2]. The main theme in this field is the creation, manipulation and detection electron spin polarization. Ferromagnetic materials are special for spintronics because it has intrinsic spin polarization inside when it's below Curie temperature. The simple model of ferromagnet (FM) is the different density of state (DOS) at Fermi level for spin-up (majority) and spin-down (minority) electrons (Fig. 1.1). Inside FM, electrons acquire an extra energy due to Zeeman splitting, $E_Z = -\mathbf{m} \cdot \mathbf{H} = g\mu_B \mathbf{s} \cdot \mathbf{H}$. This energy is positive for spin-up and negative for spin-down. This energy shift causes DOS difference at Fermi level, creating spin polarization inside FM[3, 4]. The basic understanding of spin-polarized elctron transport in FM is the two-current model where spin-up and spin-down electrons are treated independently[5, 6, 7, 8]. The total current inside FM is a sum of noninteracting spin-up and

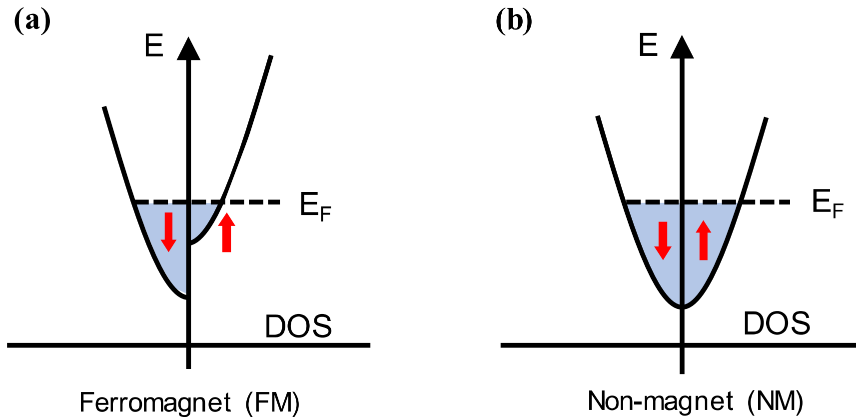

Figure 1.1: Density of state of FM and NM around Fermi level (E_F). **(a)** Non-equilibrium of spin-up and spin-down around Fermi level for FM. **(b)** Equal number of of spin-up and spin-down around Fermi level for NM.

spin-down current. This concept is also used in Chapter 4 later to describe spin injection from FM to nonmagnet (NM).

The birth of spintronics is often noted as the discovery of giant magneto-resistance (GMR) effect in Fe/Cr superlattices [9, 10]. A. Fert and P. Grünberg independently showed that electrical current can be strongly modified by spin orientation of electrons. Up to 45% of resistance drop was observed when ferromagnetic layers are tuned from anti-alignment to alignment (Fig. 1.2**(a)**). This observation was explained in terms of spin-dependent scattering between electron spin and ferromanget/nonmagnet interface[11, 12]. Namely, when spin-up electrons travel through the interface of ferromanget with majority spin-up, the scattering is less and resistance is small. If majority spin is spin-down for FM, the scattering for spin-up electrons is strong and resistance is big (Fig. 1.2**(b)**). This generates an overall lower resistance when the FM are aligned, and higher resistance when they are anti-aligned.

Similar effect was also observed in the structure of FM/I/FM, where metal spacer was replaced with insulator (I). Julliere firstly measured spin polarized tunneling in Fe/Ge-O/Fe system[13], and formulated a model for the change of conductance between parallel and

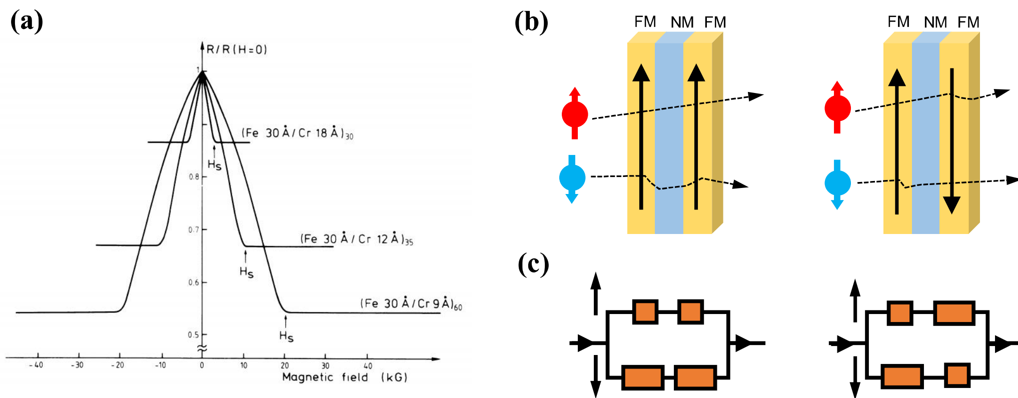

Figure 1.2: GMR effect and qualitative model. **(a)** GMR effect in Fe/Cr multilayers. Adapted from [9]. **(b)** Diagram showing the electron path for spin-up and spin-down. More scattering is expected when electrons is not aligned with FM magnetization. **(c)** Illustration of this effect in terms of parallel resistors. Smaller resistor means smaller resistance. The overall resistance is smaller for parallel alignment of two FMs.

antiparallel alignment. The corresponding tunneling magnetoresistance (TMR) for FM/I/FM magnetic tunnel junction (MTJ) is defined as $TMR = (R^{AP} - R^{P})/R^{P} = 2P_1P_2/(1-P_1P_2)$, where P_1 and P_2 are the spin polarization for the two FMs. To achieve large TMR, AlO_x was firstly widely used as the insulator[14, 15], and then the focus was shifted to MgO-based MTJs after the prediction of Δ_1 symmetry filtering in Fe/MgO/Fe system[16, 17] in 2001. Large TMR up to 600% was reported at room temperature in MgO-based MTJ[18, 19, 20, 21, 22, 23, 24]. GMR and TMR effect have revolutionized the memory technology and lead to applications in greatly improved memory devices such as MRAM (Magnetoresistance Randam Access Memory) [25, 26, 27].

While the application of spintroics in data storage has greatly advanced and generates commercial products, applications in data processing are still under fundamental investigation. In 1990 Datta and Das proposed a electron spin modulator[28](Fig. 1.3). In this device, spin polarized current was injected from a FM to a 2-dimensional electron gas (2DEG) that forms at InAlAs/InGaAs interfaces, modulated by gate tunable spin-orbirt (SO) coupling, and detected

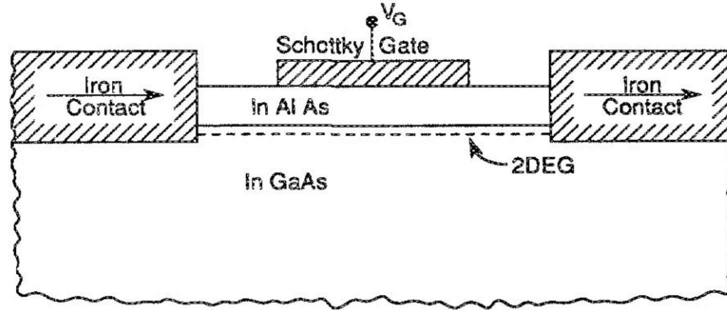

Figure 1.3: Propose of spin-FET device. Adapted from [28]. Spin current is injected from on iron contact to 2DEG, manipulated with a gate voltage and detected by another iron contact.

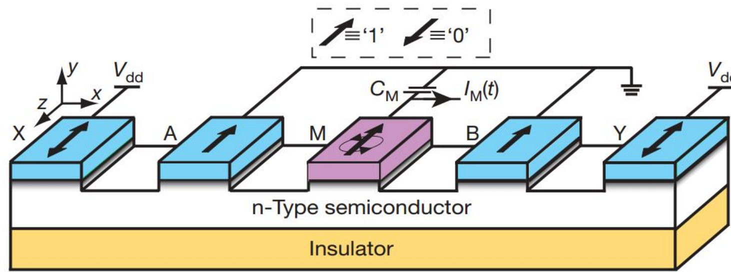

Figure 1.4: Propose of magneto-logic gate device. Adapted from [29]. Magnetization of A, B, X and Y electrodes are used as logic input states and a transient current in M electrode is used as logic output. Logic operation is OR(XOR(X, A), XOR(Y, B)).

by another FM This device is denoted as 'spin-FET', in analogy to normal field effect transistor (FET) based on charge. While the details of the device structure are still currently developing and improving, the concept of operation remains largely unchanged. Other types of spin-based logic devices has been proposed such as magnego-logic gate (MLG)[29] (Fig. 1.4) and all-spin logic device[30]. Both of these proposes are currently under development by multiple experimental research groups.

Spin injection[31, 32, 4, 12, 33, 34, 35], manipulation[36, 37] and detection are the three essential components in a typical spintronics device. Both electrical and optical methods have been developed for spin injection and detection. In this thesis, only the electrical spin injection and detection will be discussed. GMR and TMR devices are all vertical structures where

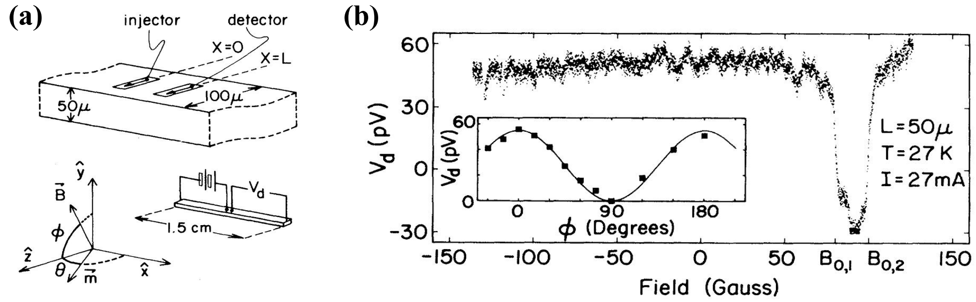

Figure 1.5: Lateral spin valve device. Adapted from [38]. **(a)** Device geometry and setup of measurements. **(b)** Magnetic field sweep from negative to positive field along x-direction. Inset: Observed Hanle-signal amplitude as a function of orientation angle ϕ of magnetic field.

spin always goes along with charge. Lateral structures are useful to study these phenomenons because the charge current and spin current can be spatially separated. This allows to study spin injection and transport separately. For this purpose, much of the spintronics effort has been focusing lateral spin transport geometry.

The first lateral spin valve (LSV) was demonstrated by Jonston and Silsbee in metal[38] (Fig. 1.5). In this device spin-polarized electrons are injected from one FM (permalloy, Py) to aluminium (Al), diffuse inside the Al spin transport channel, and are detected by the second FM electrode placed outside of the charge current loop as a voltage probe. An external magnetic field (H) is applied to manipulate spins inside Al channel. When H is applied along the FM magnetization, a step change in detected voltage is seem when one of the FM flips its magnetization direction. When H is applied perpendicular to FM, a field dependence decay of the voltage signal (Hanle effect[39]) is observed. These pioneer observations unambiguously demonstrate successful spin injection from FM to NM, spin manipulation with external magnetic field and spin detection.

Stimulated by the above work, Jedema and co-workers[40, 41] demonstrated room temperature spin injection, precession and detection in Co/Al/Co LSV (Fig. 1.6 **(a)**). In this device, spin accumulation inside Al channel is created by electrical spin injection from cobalt

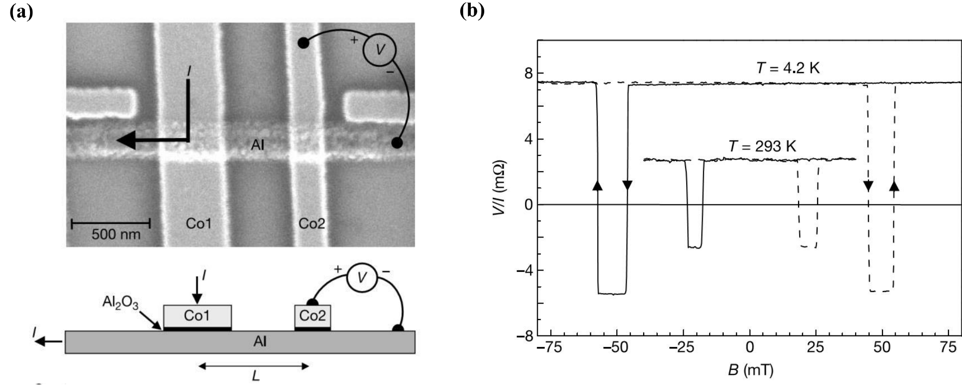

Figure 1.6: Electrical spin injection and detection in metal lateral nonlocal spin valve. Adapted from [41]. **(a)** SEM image of the device with two cobalt (Co) electrodes spacing of L = 650 nm. **(b)** Magnetoresistance V/I as a function of the in-plane magnetic field at 4.2 K and 293 K (room temperature).

(Co) to Al through A_2O_3 tunnel barrier. This unbalanced spins diffuse inside Al channel in both directions: one is into the electrical current path and the other is completely out of current loop. By placing a second Co electrodes away from the current loop, a spin-dependent voltage can be detected as a function of applied magnetic field (Fig. 1.7). This so called 'nonlocal' detection strongly suppresses artifact in the measured signal due to the complete separation of the charge current and spin current. Clear MR effect ($R_{NL} = V/I$) is seem when magnetic field is swept in plane (Fig. 1.6 **(b)**) and Hanle effect can be observed when applying out of plane magnetic field (Fig. 1.7). Microscopic models[32, 42] have been developed to explained observed MR size and Hanle precession data. Based on the dependence of MR over spin transport channel length, spin polarization (P) inside Al spin channel and spin diffusion length (λ_s) can be extracted. Based on the field-dependence of Hanle precession, spin lifetimes (τ_s) and diffusion coefficient D can be extracted (Fig. 1.7) which are related to λ_s by $\lambda_s = \sqrt{D\tau_s}$.

Microscopic study of spin injection across FM/NM interface[32, 12] and transport in lateral mesoscopic spin valve [43, 42] has been carried out in the frame of calculating spin-up and spin-down chemical potential. A more complete drift-diffusion mode for lateral microscopic

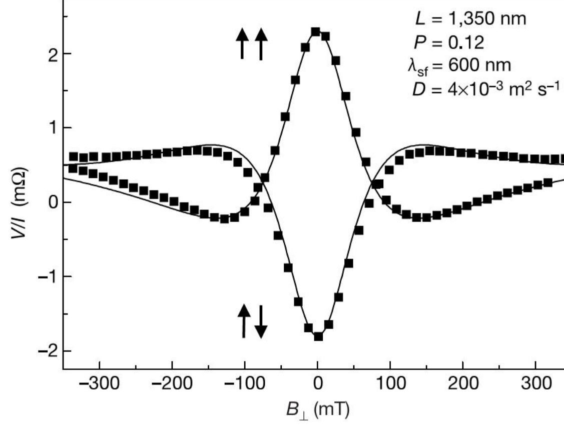

Figure 1.7: Spin precession in a perpendicular magnetic field. Adapted from [41]. Spin lifetime (τ_s), spin diffusion length (λ_s) and diffusion coefficient (D) can be obtained by fitting the data to Equ. 1.2.

spin valves has been developed by Takahashi and Maekawa[44]:

$$R_{NL}^{P/AP} = \pm 2R_N e^{-\frac{L}{\lambda_s}} \prod_{i=1}^{2} \left(\frac{\frac{P_J R_i}{R_N}}{1-P_J^2} + \frac{\frac{p_F R_F}{R_N}}{1-p_F^2} \right) \left[\prod_{i=1}^{2} \left(1 + \frac{2\frac{R_i}{R_N}}{1-P_J^2} + \frac{2\frac{R_F}{R_N}}{1-p_F^2} \right) - e^{-\frac{2L}{\lambda_s}} \right]^{-1} \tag{1.1}$$

where P/AP indicates the parallel and antiparallel alignment of spin injector and spin detector, $R_N = \rho_N \lambda_s / A_N$ is the spin channel resistivity, $R_F = \rho_F \lambda_F / A_J$ is the FM resistivity, A_J is the junction area, P_J in interfacial spin polarization, R_i is the interfacial resistance, ρ_F and λ_F are the spin polarization and spin diffusion length inside FM, respectively. This equation has worked reasonably well in the low bias region where bias dependent spin injection is not strong. More discussion about the this equation is in Chapter 4. Spin precession in external magnetic field can be fitted to a diffusive Hanle equation described by the following equation[41]:

$$\Delta R_{NL} \equiv R_{NL}^{P} - R_{NL}^{AP} = S \int_0^{+\infty} \frac{1}{\sqrt{4\pi D t}} e^{-L^2/(4Dt)} \cos(\omega_L t) e^{-t/\tau_s} dt \tag{1.2}$$

where S is Hanle amplitude, L is spacing between spin injector and spin detector, D is spin diffusion coefficient, $\omega_L = g_e \mu_B H_\perp / \hbar$ is Larmor precession frequency, τ_s is spin lifetime. Information such as τ_s and D (thus $\lambda_s = \sqrt{D\tau_s}$) can be obtained from the fitting.

In recent years the focus on spin transport channel has extended from metal (Al[41], Cu[45], Ag[46],) to include traditional semiconductor (GaAs[47, 48, 49], Si[50, 51], Ge[52]),

carbon-based materials (Alq_3[53], carbon nanotube[54], graphene[55]) and two dimensional transition metal dichalcogenide[56, 57]). Great success has been achieved in graphene where room temperature spin injection and detection[55], long spin diffusion length ($\sim 10\ \mu$m[58] or higher[59]) and long spin lifetimes[60] are experimentally demonstrated.

1.2 Graphene

Graphene, defined as a single atomic layer of carbon atoms arranged in an hexagonal honeycomb lattice structure (Fig. 1.8(**a**)), has attract scientists attention for a long time[61, 62, 63] It is the nature building block for widely available graphite and also has a unique band structure[64, 65, 66]. Theory predicts that at Fermi level in graphene, conduction band and valance band is touching at a single point, called 'Dirac point'(Fig. 1.8(**b**)). Nearby this Dirac point, electron energy scales linearly with momentum: $E = \hbar|\mathbf{k}|v_F$, where $v_F(\sim 1\times 10^6$ m/sec[67, 68, 69]) is the speed of electrons. This Dirac particle-like energy dispersion gives super high mobility ($\sim 2\times 10^5$ cm^2/V sec) of electrons in graphene[70, 71, 72].

However, single layer graphene was predicted to be not thermodynamically stable by it self[73, 74], until 2004 when Novoselov and Geim firstly isolated single layer graphene and characterized on a substrate[75]. The method to separate single layer graphene out of a big chuck of graphite was so called 'Scotch tape' methods which has been used in scanning tunneling microscopy (STM) for decades to obtain fresh graphite surface. A thick graphite was firstly detached from a graphite using an adhesive tape and thinned down by repeatedly attaching it to another adhesive tape. Finally very thin graphite was deposit onto commercially available SiO_2/Si substrate. Graphene was found to be stable in ambient environment and have superior electrical conductance compared to normal metal at similar thickness. Importantly, graphene can be easily identified by using an optical microscope. This pioneer work has in-

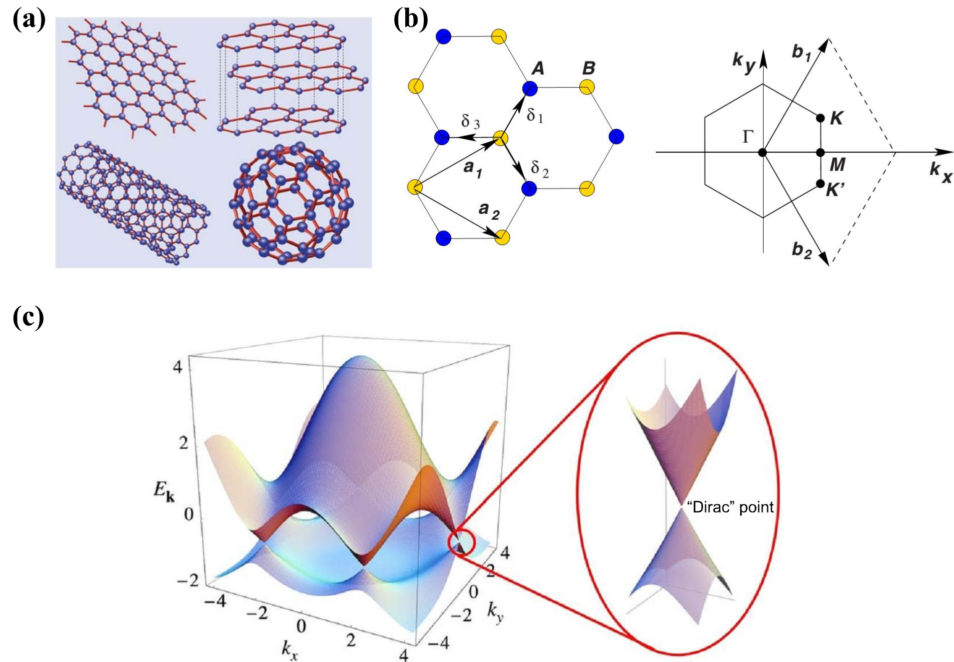

Figure 1.8: Lattice and band structure of graphene. Adapted from [62]. **(a)** 2D graphene glattice, 3D graphite, 1D carbon nanotube and 0D 'bucky' ball. **(b)** (left) Lattice of graphene with two inequivalent bases. (right) Brillouin zone of graphene in *k*-space. **(c)** Band structure of graphene. Fermi level is located at six touching point of conduction band and valance band.

spired and triggered enormous research effort on trying to understand it's electronic[62, 63] and mechanic properties[76, 77, 78, 79], large scale synthesis[80, 81] and potential applications in chemical[82, 83] or biology sensing technology[84]. More importantly, a new class of materials, true two-dimensional (2D) materials[85, 86, 87] starts to emerge and revolutionize the research and industrial society[88]. For this reason, in 2010 Novel Physics prize was awarded to Novoselov and Geim[89].

The first experimental demonstration of graphene's 2D nature was anomalous integer quantum Hall effect (QHE)[90, 91] (Fig. 1.9) in this material. The abnormal quantization index in QHE reveals the unconventional Berry phase buried inside its band structure[92]. This QHE exists up to room temperature[93], offering a new standard for determining electrical resistance and relation of other basic parameters.

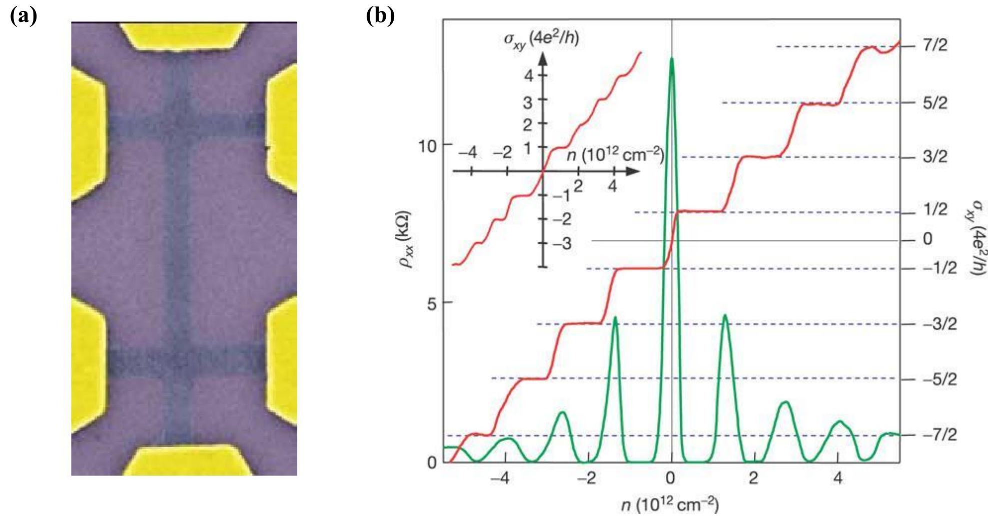

Figure 1.9: Quantum Hall effect in graphene at T = 4 K. Adapted from [90]. **(a)** Scanning electron microscope (SEM) image of a Hall bar devices (the width of the central wire is 0.2 mm). False colours are chosen to match real colours as seen in an optical microscope for large areas of the same materia. **(b)** Hall conductivity ρ_{xx} and longitudinal resistivity ρ_{xy} of graphene as a function of their carry concentration at B = 14 T and T =4 K. Inset: ρ_{xy} in bi-layer graphene where the quantization sequence occurs at integer n. The latter shows that the half-integer QHE is exclusive to single layer graphene.

Unlike metal, electronics properties of graphene can be greatly tuned when it is placed on a insulating substrate (eg. commercially available SiO_2/Si substrate), due to its low density of states around Fermi level. High electronic mobility of up to 20, 000 cm^2/V sec was demonstrated at room temperature[94, 95] of graphene on SiO_2/Si substrate. The substrate has a significant effect in the properties of graphene due to interaction with substrate and morphology. On SiO_2, carrier mobility is believed to be limited by scattering from charged surface states and impurities[96, 97, 98, 71, 99], substrate surface roughness[100, 101, 102], atomic defects[95] and SiO_2 surface optical phonons[103, 71]. STM studies shown that SiO_2 is a not an ideal substrate for graphene due to substrate-induced electron-hole paddle[104, 105] (Fig. 1.10). This creates local variation of carry density in graphene. Later works reveal that suspended graphene devices exhibits much higher mobility, up to 200, 000 cm^2/V sec[72, 106],

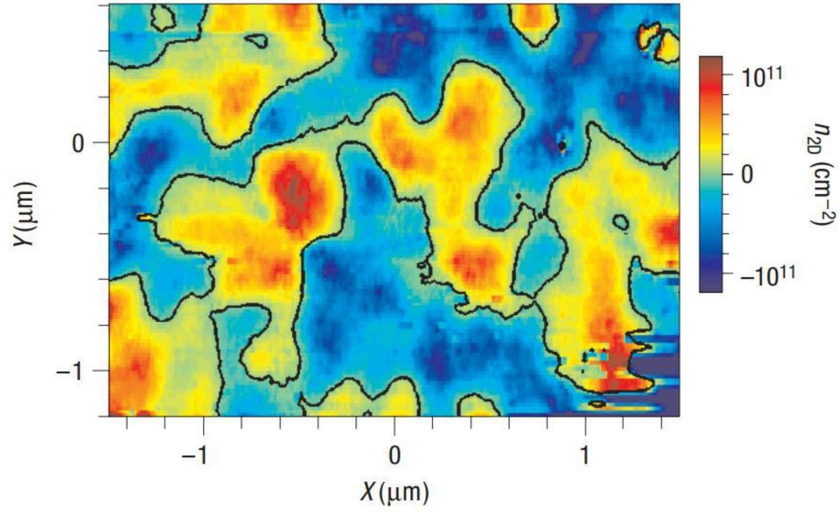

Figure 1.10: Spatial density fluctuations and electron-hole puddles. Adapted from[104]. Colour map is the spatial density variations in the graphene flake extracted from surface potential measurements at high density and when the average carrier density is zero. The blue regions correspond to holes and the red regions to electrons. The black contour marks the zero density contour.

confirming the substrate is an limiting factor for electronic performance of graphene. However, for application purposes a substrate-supported graphene device is more favorable. The search for alternative substrate was brought up in 2010 where graphene is mechanically transferred to hexagonal boron nitride (hBN) flakes which has a much smoother surface than SiO_2[107, 108] (Fig. 1.11) and very close lattice constant to graphene (2.50 Å for hBN compared to 2.46 Å for graphene). This has opened a door to achieve high mobility graphene devices, enabling to see extraordinary features in graphene electronic transport such as Hofstadter's butterfly[109] when graphene lattice aligns with bottom hBN substrate[110, 111, 112]. More important, this technique enables the unlimited stacking of 2D van der Waals materials (graphene, hBN, MoS_2) in any desired order, allowing for unforeseen device structures that was not possible before. Other substrates were also demonstrated to give superior electronic perform of graphene, such as SiC[113],mica[114], MoS_2[115].

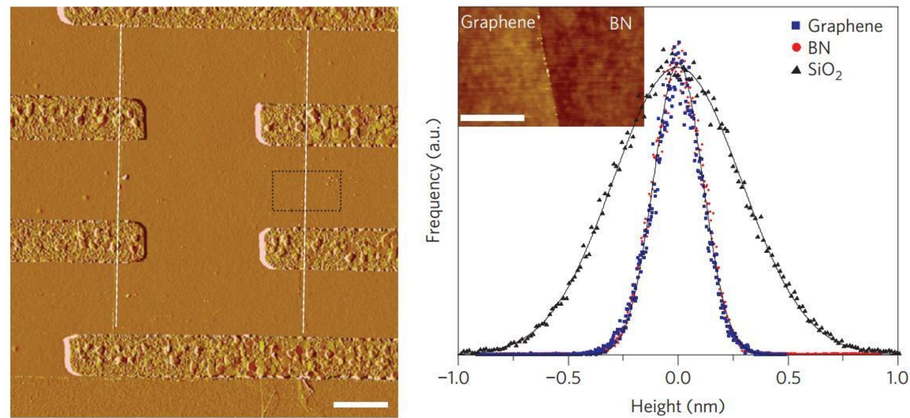

Figure 1.11: Atomic force microscope (AFM) image of a graphene on hBN device. Adapted from [107]. **(Left)** AFM image of monolayer graphene on BN with electrical leads. White dashed lines indicate the edge of the graphene flake. Scale bar: 2 μm. **(Right)** Histogram of the height distribution (surface roughness) measured by AFM for SiO_2 (black triangles), h-BN (red circles) and graphene-on-BN (blue squares). Solid lines are Gaussian fits to the distribution. Inset: high-resolution AFM image showing a comparison of graphene and BN surfaces, corresponding to the dashed square in the left. Scale bar: 2 μm.

While significant amount of the graphene research was done on exfolated flakes, the effort to synthesis large area graphene is also very active because of the requirement of electronics applications. Experimentally epitaxy graphene was first synthesized on SiC substrate by desorption of Si from SiC surface[116, 117], and later on metal substrate[118, 119, 120]. The big advantage with graphene grown on metal is the ability to transfer grown graphene to arbitrary substrate[121]. Reliable large area, single layer graphene was achieved when using chemical vapor deposition (CVD) with methane (CH_4) as precursor and polycrystalline copper (Cu) as growth substrate[80] (Fig. 1.12). The electronic properties were found to be close to exfoliated flakes, indicating high quality of epitaxy graphene. By improving growth parameter and transfer techniques[122, 123, 124], the quality of CVD-grown graphene is now comparable to that of exfoliated graphene flakes[125]. More details of large area graphene growth will be discussed in Chapter 7.

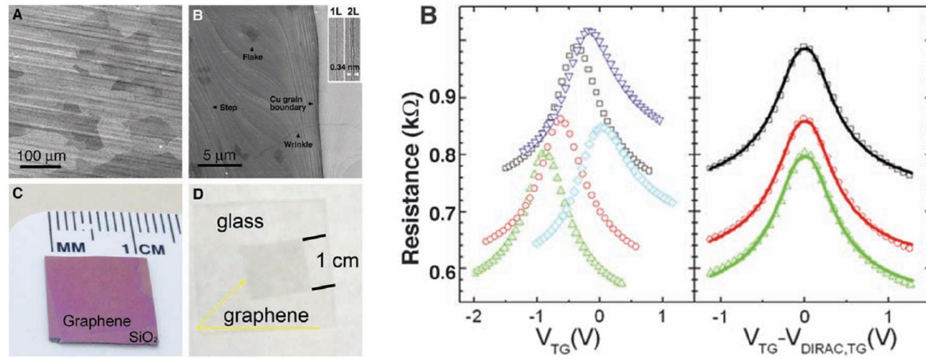

Figure 1.12: Large area, single layer graphene grown on copper foil. Adapted from[80]. **(Left)** **A**. SEM image of graphene on a copper foil. **B** High-resolution SEM image showing a Cu grain boundary and steps, two- and three-layer graphene flakes, and graphene wrinkles. Inset in **B** shows tunneling electron microscopy (TEM) images of folded graphene edges.1 L, one layer; 2 L, two layers. (**C** and **D**) Graphene films transferred onto a SiO_2/Si substrate and a glass plate, respectively. **(Right)** Device resistance vs. top-gate voltage (V_{TG}), with different backgate (V_{BG}), and vs. V_{TG} - $V_{Dirac,TG}$, with a model fit (solid line).

1.3 Graphene Spintronics

Graphene is consisting of light carbon (C) atoms, thus having low spin-orbit coupling[126, 127, 128] and small hyper-fine coupling (98.89% of C atoms are ^{12}C which has zero nuclear magnetic moments)[129, 130]. Combining with high mobility, graphene is very promising for spintronics because spin lifetimeτ_s and spin relaxation length λ_s in graphene could be very long: μs - ms for τ_s and $\sim$ 200 μm[126] for λ_s in intrinsic graphene.

The first clear demonstration of electrical spin injection and detection in graphene was achieved by Tombros and co-workers[55] in 2007 in a nonlocal detection geometry (Fig. 1.13). Electronic spins are injected from Co electrodes to exfoliated graphene falkes through a pin-hole Al_2O_3 barrier. Fig. 1.13 shows the SEM image of graphene lateral spin valve and room temperature MR indicating spin transport. Spin lifetimes were found to be $\sim$ 100 - 200 ps and spin diffusing length was 1 - 2 μm at room temperature. The magnitude of MR and λ_s are much larger than those found in metals[41].

At around the same time, there are several other groups reporting spin transport

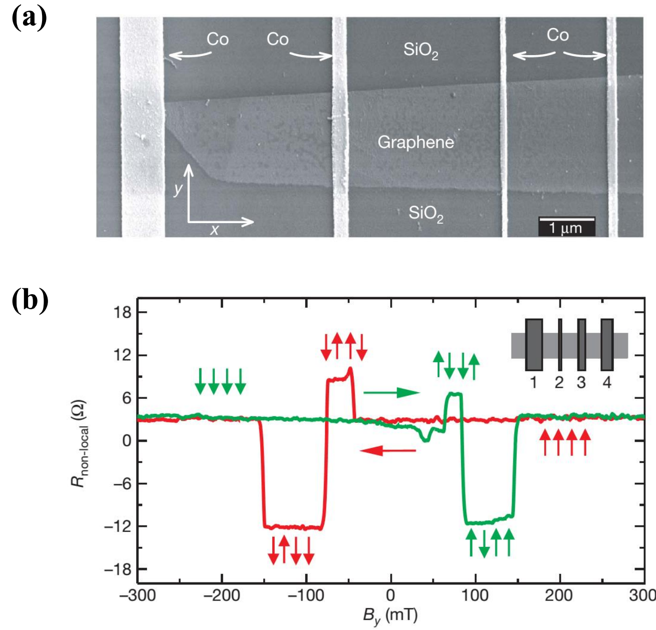

Figure 1.13: Room temperature spin injection and detection in graphene. Adapted from [55]. **(a)** SEM image of lateral spin valve on exfoliated graphene flakes. **(b)** MR as a function of in-plane magnetic field.

signatures in graphene based devices either in mesoscopic graphite[131, 132] or single layer graphene[133, 134]. This is generally considered as the starting era of graphene spintronics.

The observed τ_s and λ_s, however, are much lower than theoretical predictions. The effort in graphene spintronics has been focused on understanding spin relaxing mechanism in graphene due to momentum scattering[135, 136, 137, 138], contacted-induced relaxing[60, 139, 140], charged-impurities scattering[141, 142], localized magnetic moments[143] and spin-orbit coupling[144]. Bias dependence of spin injection[145, 146] and drift effect [147]were also carried out to better understand spin injection and transport in graphene.

One of the important advance in this field is tunneling spin injection into graphene done by Han and co-workers[60]. It has been well known that conductivity mismatch between FM and NM is a big obstacle to achieve efficient spin injection int NM[35, 34]. Graphene has a significant lower conductivity than three dimensional FM metals, causing most of the injected spins diffuse back into the FM[148]. An thin insulating layer can help with overcome

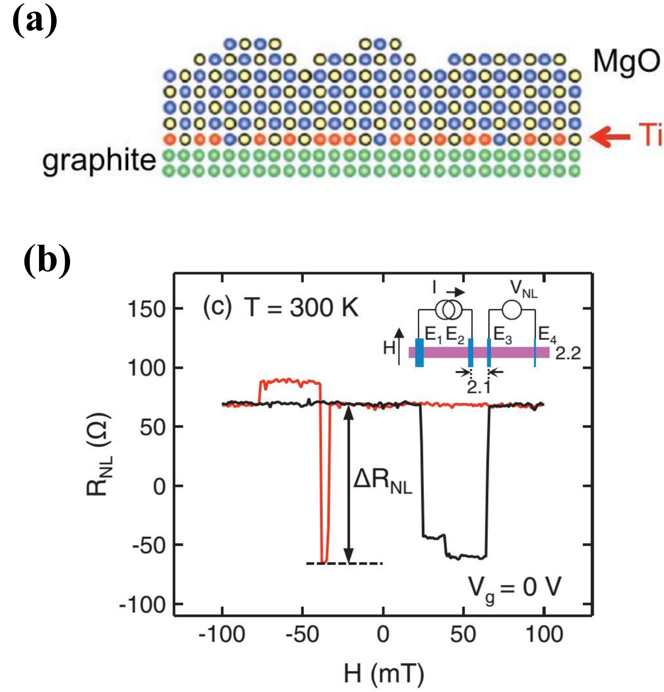

Figure 1.14: Growth of atomical smooth MgO for tunneling spin injection into graphene. Adapted from [152]. **(a)** Atomic smooth MgO grown on graphene using Ti seeding layer. **(b)** Large room temperature MR observed in graphene LSV using MgO as tunnel barrier.

this conductance mismatch issue, as demonstrated in metals[41] and semiconductors[49]. However, van der Waas nature of graphene make the epitaxy growth of insulator (mainly oxide) very challenging[149]. Atoms deposited on top tends to form clusters at room temperatures[150]. Han and co-workers developed Ti-seeded MgO growth on single layer graphene which turns outs to be atomically smooth[151] (Fig. 1.14 **(a)**). 0.5 ML of Ti was firstly deposited as anchor and $\sim$ 1 nm MgO was evaporated from ebeam evaporator in an ultra-high vaccum (UHV) chamber. By using this smooth MgO as tunnel barrier between graphene and FM, tunneling spin injecting into single layer graphene was achieved[60] (Fig. 1.14 **(b)**). Longer spin lifetimes ($\sim$ 500 ps) and spin diffusion length ($\sim$ 3 μm) has been observed. Up to ns spin lifetimes were reported with improved tunnel barrier and cleaner graphene devices[136, 138, 140, 58].

In pristine graphene spins relaxation is believed to be limited by spin-orbit coupling

and phonon scattering. More recent theoretical work on spin-orbit coupling in graphene give energy spin splitting at Dirac point about 24 - 50 μeV[153, 154, 155]. The spin relaxation mechanism in graphene has been largely explored in the contents of Elliot-Yafet (EY)[156, 157, 158] and DyakonovPerel (DP)[159]. For EY mechanism, spin flips sign with a probability during an momentum scattering event. This finite probability is due to wave function mixing of spin-up and spin-down in the present of spin-orbit coupling. The spin relaxation rate is roughly $1/\tau_s \propto 1/\tau_p$, where τ_p is the time between momentum scattering events. So the more momentum scattering is (τ_p is small), the **shorter** spin lifetime is. For DP mechanism, spin processes in a randomly fluctuating spin-orbit field created by spin-orbit coupling when space inversion symmetry is broken. The spin relaxation rate is $1/\tau_s \propto \tau_p$. So the more momentum scattering is (τ_p is small), the **longer** spin lifetime is.

Experimentally, investigating the origin of spin relaxation is a hot topic. Several groups have reported linear scaling of τ_s vs. τ_p[135, 136] (Fig. 1.15) in single layer graphene, which is consistent with EY mechanism. For bilayer graphene, τ_s was found to decrease with increasing D (or τ_p)[138, 136], suggesting DP mechanism. They are also other reports of possible DP in single layer graphene[139] and EY in few layer graphene[160]. So the exact spin relaxation in graphene is still controversial[161]. Other experiments were trying to address this issue by chemical doping of metal atoms on graphene[141, 142]. The results showed that spin lifetime is largely unchanged while momentum scattering time significantly reduced due to charged impurities scattering. Similar results were found in graphene devices which mobility was tuned from 2, 700 to 12, 000 cm^2/V sec[137].

Apart from the experimental discrepancy of spin relaxation time in graphene, overall the spin lifetime is much shorter than predicted. Possible explanation of observed short spin lifetime ($\sim$ 1 ns) was proposed[162] where pseudo-spin were accounted for extra spin relaxation.

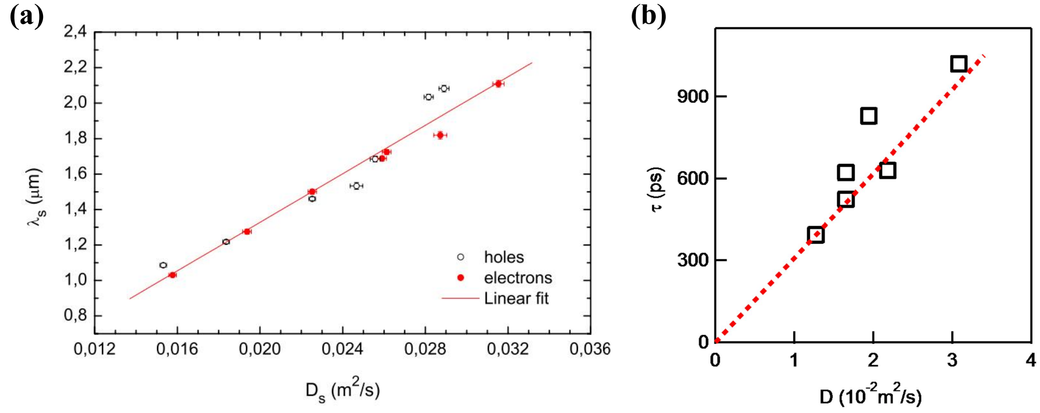

Figure 1.15: Linear scale of spin relaxation time and momentum scattering time. **(a)** Spin diffusion length $\lambda_s = \sqrt{D\tau_s}$ scales linear with diffusion coefficient D. Adapted from [135]. **(b)** Spin lifetimes τ_s scales linear with diffusion coefficient D. Adapted from [136].

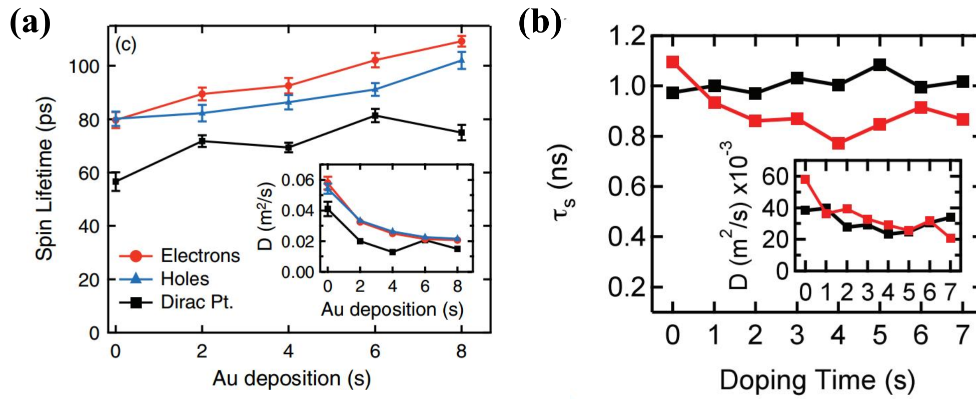

Figure 1.16: Spin lifetime τ_s as a function of metal deposition on top of graphene. **(a)** τ_s as a function of Au deposition time. Adapted from [141]. **(b)** τ_s as a function of Mg deposition time. Adapted from [142].

Resonant scattering by magnetic impurities[163] is also proposed as potential spin relaxtation mechanism.

The current research on this field extended more to understanding spin-orbit coupling[144], proximity effect[164] in graphene and potential applications in logic devices[165, 166]. A most recent review in graphene spintronics can be found at [167].

1.4 Motivation and Outline

The work in this thesis was motivated by the proposal on magneto-logic gate based on graphene[168, 166]. At the time of this proposal, the critical spin transport phenomenon has been experimentally demonstrated, including room temperature spin transport[55], efficient spin injection[60], long spin lifetime[136, 138] and long spin diffusion length[59, 169]. The proposal predicts a non-volatile and reconfigurable logic device that can be integrated to perform high speed, low power consumption search engine. It is interesting not only from application point of view, but also from basic science. For example, what is the spin dynamics at high frequency (high speed), how to implement spin transfer torque in graphene devices, what is limiting the spin lifetime and spin diffusion length in graphene and how to improve these quantities. This involves materials research, device characterization and modeling, circuit integration, etc. Seven PIs from different aspect teamed up to tackle this challenges. More details is discussed in Chapter 2.

The following of the thesis is constructed as follows:

Chapter 2 will introduce the proposal of magneto-logic gate (MLG) based on spin accumulation in graphene channel. The main work of this thesis is trying to experimentally develop this MLG with the collaboration of other groups. Challenges and approaches will be discussed.

Chapter 3 will discuss experimental details of graphene spin valve devices fabrication and measurement.

Chapter 4 will discuss the current detection of spin transport in single layer graphene which is an important advance for the readout of MLG .

Chapter 5 will discuss the bias dependence of spin injection into graphene. This will provide more complete understanding of spin injection process across the FM/Graphene

interface.

Chapter 6 will discuss the demonstration of XOR logic in graphene spin valve devices. Experimental details will be presented.

Chapter 7 will discuss our large area graphene growth and fabrication of spin valve on the grown epitaxy graphene.

Chapter 8 will summarize and conclude this thesis.

Chapter 2

Magneto-Logic Gate in Graphene

This chapter will discuss the proposed magneto-logic gate bases on spin transport in graphene[168, 166]. This is a collaborative effort among several campuses, including experimentalist and theorists. Challenges and our approaches will be discussed.

2.1 Introduction

While extensively studied in application of GMR and TMR devices has been conducted in spintronics research, they are several proposed applications using spintronic devices for logic operation purposes[28, 170, 171, 172, 173, 174, 175, 29, 176, 30]. In 2007 Dery and co-workers proposed a universal magneto-logic gate based on semiconductor GaAs[29]. In this device the logic operation is achieved by manipulating spin accumulation inside GaAs, instead of spin current flow. This device is nonvolatile and reprogramable to be basic logic gates (OR, NAND, NXOR). However, the spin transport phenomena of semiconductors at room temperature is still under development[177, 178]. After graphene has been demonstrated to be a great spin channel at room temperature[55, 167], this magneto-logic gate is revisited based on graphene[168, 166]. Due to high mobility and long spin diffusion length, graphene based

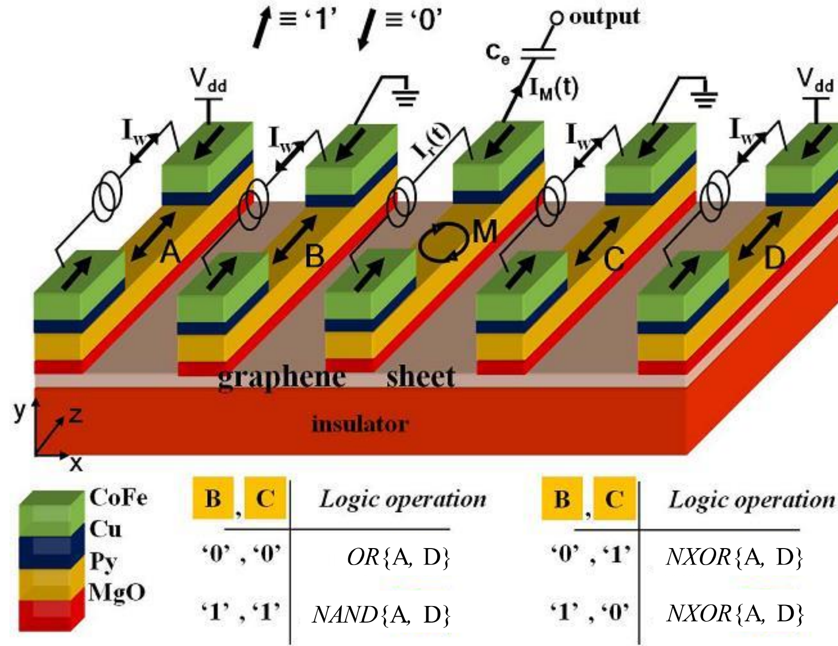

Figure 2.1: Universal and reconfigurable magneto-logic gate based on spin accumulation in graphene. Adapted from [168]. Five ferromagnetic electrodes are deposited on top of a single layer graphene. The spin accumulation profile in the sheet determines the logic results and it is governed by the magnetic direction of the biased section (A-B and C-D). Using spin transfer torque, the logic operands (magnetization direction of A-D) are encoded via the individual writing current, $I_w(t)$, across the low resistive and all metallic path (CoFe/Cu/Py/Cu/CoFe). The readout is triggered by the reading current signal, $I_r(t)$ that perturbs the magnetization of the middle contact. The binary logic output is the resulting on/off transient current $I_M(t)$.

magneto-logic gate was found to operate at high speed and low power consumption, especially for data searching[168].

2.2 Working Principle

Fig. 2.1 shows the design of a basic magneto-logic gate (MLG) based on graphene. It consists of five ferromagnetic electrodes contacting a graphene channel. Four of the electrodes (A, B C and D) are uses as input, and output is a transient current from readout electrode M. The logic input '1' and '0' corresponds the magnetization direction of the input electrodes (A, B C and D), eg. '1' means magnetization direction is up, '0' is down. Each input electrodes use

Py as the spin injector for creating spin accumulation in graphene by passing electrical current (supplied by V_{dd}) between Py and graphene through a MgO tunnel barrier. MgO is used to increase the spin injection efficiency into graphene[60]. For the input bits, The magnetization direction of the Py layer is set by passing a current (I_w) through the two fixed nanomagnets (CoFe) in which magnetizations are the opposite. Electrical current I_w will become spin polarized and flows through Py layer. Spin angular momentum in the current can be transferred to the Py. If this angular momentum is big enough, magnetization of Py can be flipped to the other direction if it is not aligned with the electron spin. This phenomena is called spin transfer torque (STT)[179, 180, 181, 182]. In this way, the input states can be controlled by an electrical current.

Spin accumulation inside graphene, especially underneath the middle output electrode M, is strongly dependent on the orientation of the input electrodes. Fig. 2.2 shows the spin accumulation under M for parallel and antiparallel configuration between A and B. Since MLG has a mirror symmetry around M, situation for C and D can be simply added in. Electrical current flows from electrode A to graphene to electrode B, so electrons flow from electrode B to graphene to A. Assuming B and A are magnetized to be up (Fig. 2.2(**a**)), electrons injected from B will have more spin-up than spin-down, causing net spin-up accumulation in graphene under B. When electrons are flowing from graphene into A (spin extraction), spin-up electrons will escape from graphene more easily than spin-down electrons[183], causing net spin-down accumulation under A. When A and B are very close (spacing is much smaller than the spin diffusion length in graphene (2-10 μm[167])), most of the spin-up electrons injected from B will be extracted from A, leaving small spin accumulation under M (Fig. 2.2(**a**)). For the case of antiparallel configuration, say A is '0' and B is '1', the spins that are extracted from A is mostly spin-down, so the overall spin-up accumulation inside graphene channel is much larger compared to A is '1' and B is '1' (Fig. 2.2(**b**)). This bigger spin accumulation will generate a

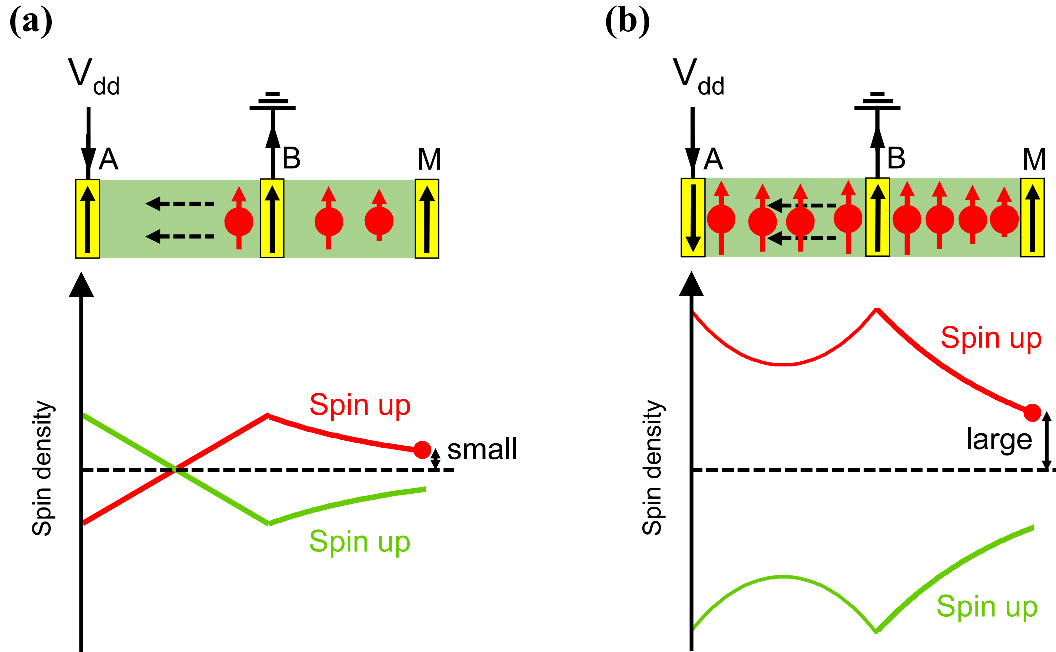

Figure 2.2: Spin density of parallel and antiparallel configurations for the input electrodes A and B. Electrical current is flowing from A to graphene to B, and electrons flow from B to graphene to A (indicated by dashed arrow). **(a)** Parallel configuration, A = B = '1'. Spin accumulation under M is small. Output is logic '0'. **(b)** Antiparallel configuration, A = '0', B = '1'. Spin accumulation under M is large. Output is logic '1'.

large output current signal when magnetization of electrode M is perturbed by STT[184].

The readout current of a MLG is shown in Fig. 2.3. In this case, a search operation is simulated. The stored bits are stored in both contacts B and C (B = C) and the search bits are stored in both A and D (A = D). Using the experimental parameters from [60], the output signal $I_M(t)$ is simulated during the search operation. The search operation is done by sending a pulse of current $I_r(t)$ for 1 ns. When readout bit M undergo a 1 ns in-plane magnetization rotation, the output current signal $I_M(t)$ can have different behaviors, depending on weather A and D are matching B and C or not. If A = B (and C = D), a non-zero transient current is obtained in the simulation (Fig. 2.3). This is labeled as logic output '1'. If A $\neq$ B (and C $\neq$ D), a constant zero transient current is obtained. This is labeled as logic output '0'. More details of the operation

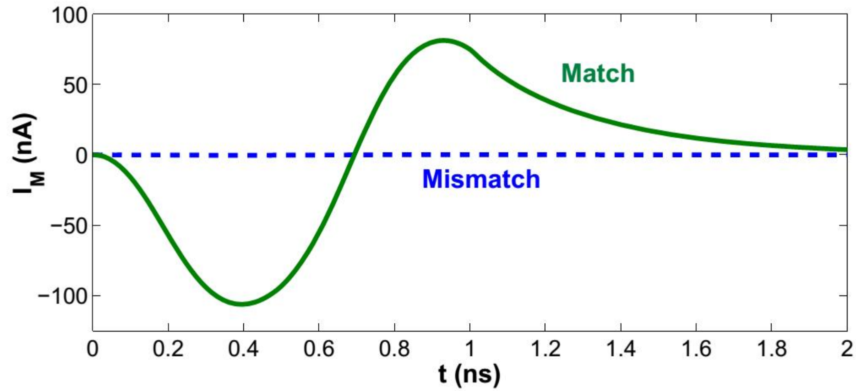

Figure 2.3: Transient current across the middle readout electrode M during a search operation. Adapted from [168]. Grean solid line indicates that the search bit matches the stored bit. Blue dashed line indicates that the search bit does not match the stored bit.

can be found in [29, 168, 166].

In order to large circuit integration, the ability to use the output of one logic gate as the input of another logic gate (fan-out) is important. However, in the proposed MLG, output current I_M ($\sim$ 100 nA) is too small to drive the input of MLG (I_w). External latches are needed for integration purposes. More details can be found in [29, 168, 166].

The multidisciplinary effect on trying to demonstrate this MLG in graphene has involved several teams: experimental materials and devices (Roland Kawakami[1], Jing Shi[2], Ilya Krivorotov[3]), device modeling (Igor Zutic[4], Lu Sham[5]) and circuit design and simulation (Hanan Dery[6], Hui Wu[7]). All the teams worked together to tackle the challenges to achieve the proposed MLG.

2.3 Challenges and Approaches

They are several critical challenges to achieve the proposed applications of this MLG.

[1]http://www.physics.ohio-state.edu/ kawakami.15/
[2]http://www.physics.ucr.edu/people/faculty/shi.html
[3]http://faculty.sites.uci.edu/krivorotovgroup/
[4]http://www.physics.buffalo.edu/faculty/IZutic.html
[5]http://physics.ucsd.edu/ ljssst/ljs.html
[6]http://www.ece.rochester.edu/people/faculty/dery_hanan/index.html
[7]http://www.ece.rochester.edu/projects/laics/people.html

The first challenge is to achieve efficient, uniform spin injection inside graphene channel. Although MgO tunnel barrier serves as the best tunnel barrier so far for spin injection into graphene, its complexity to fabricate, low yield, non uniformity[152] make it not idea for large scale fabrication of MLG. For MLG to work properly, the spin injection efficiency across all the input electrodes (A - D) needs to be similar, otherwise some input bit will dominate over the others. The other alternatives for tunnel barrier could be insulation hBN[185, 186] and Al_2O_3[187]. Over the past few years, three groups has demonstrated spin injection across 1 - 3 layers of hBN[188, 189, 190, 191], either by exfoliated or chemical vapor deposition grown hBN. The quality of this barrier still needs great improvement to render longer spin lifetimes and spin diffusion length. They are also studies on using smooth Al_2O_3 as tunnel barrier [192, 59]. It is promising but the uniformity is unclear. Currently we are working on devices where graphene is sandwiched between two layer of hBN: the bottom hBN is relative thick ($\sim$ 10 - 20 nm[107]) serving as a flat substrate, the top hBN is thin (1 - 3 atomic layers) acting as tunnel barrier. Recently we have developed growth of atomically smooth and crystalline SrO on graphene and this SrO seems to have good tunneling properties.

The second challenge is a complete understanding of spin injection and transport properties in graphene which will be important to be served as a guide to improve device performance. To tackle this problem, we did bias dependence study of spin injection across MgO (see more details in Chapter 6) and Al_2O_3 tunnel barrier. A strong bias dependence was found and was probably due to Fermi level change in the ferromagnetic electrodes. Experimental and theoretical modelling are still under development.

The third challenge is to demonstration the truth table of MLG. This is important demonstrate the working principles of MLG. Experimental strategies has to be developed to demonstrate the concept of the MLG. We have successfully demonstrated XOR logic operation in graphene spin valve devices, which is essentially half of the proposed MLG (see more details

in Chapter 6).

The fourth challenge is to achieve low energy spin torque switching of ferromagnetic electrodes. This is essential because this serves as the method to change the input states of for MLG. Our collaborators (Ilya Krivorotov's group) are working on to this while we assist with the materials deposition.

The fifth challenge is the demonstration of current readout of the MLG. The state of art detection of spins in graphene is bases on electrical voltage signal. A versatile current-based detection scheme needs to be developed to achieve current output. This problem is tackled in Chapter 4.

The sixth challenge is to achieve achieve efficient spin injection over large area graphene. To scale MLG up to the level that it can function as a stand alone working machine (eg. computer), large area graphene is needed to fabricate multiple devices on the same chip. While most of the graphene spintronics research was done on exfoliated graphene flakes, properties of the large area graphene for spin transport needs to be investigated. Chapter 7 will discuss the demonstration of successful spin transport in chemical vapor deposition grown large area graphene.

The seventh challenge is the large scale integration of the multiple MLG. This is an ongoing effort from the theory and simulation collaborators.

Chapter 3

Devices Fabrication and Transport Measurement

This chapter will describe the detailed graphene spin valve devices fabrication steps and electrical measurement procedures, including charge transport and spin transport.

3.1 Graphene Spin Valves Fabrication

1. **SiO_2 substrate preparation.** The fabrication starts with cleaving the 4” size thermally-oxided Si wafer bought from University Wafer (300 nm SiO_2 on top of 500 μm Si. Si is *p*-doped with resistivity 0.001 - 0.005 Ω·cm) using a diamond scribe (Fig. 3.1(**a**)). This is the supporting substrate for all of the graphene spin valve devices described in this thesis. After cleaving down to $\sim$ 5×7 mm size, the wafers are cleaned in sequence of sonication in the following order: 15 min acetone $\rightarrow$ 15 min acetone $\rightarrow$ 15 min isopropanol alcohol (IPA), with blew dry by compressed nitrogen gas after each sonication step. After the last sonication and blow dry, the wafers are baked at 150 °C on a hotplate for $\sim$ 1 hours to get rid of solvent and

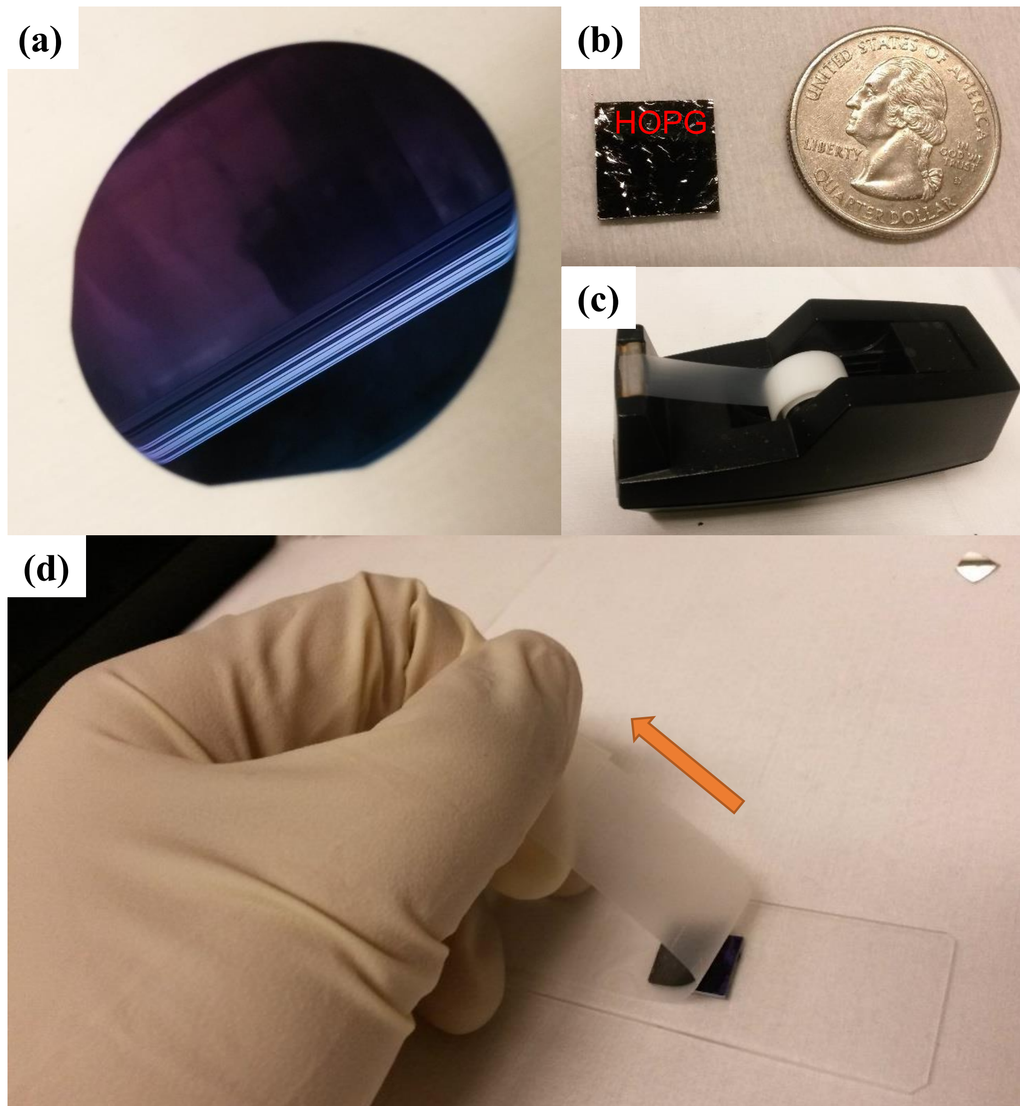

Figure 3.1: Exfoliation of graphene onto SiO_2 substrate. **(a)** Commercial available 4" SiO_2/Si wafer for supporting graphene. **(b)** 1×1 cm size HOPG crystal (left) compared to a quarter dollar (right). **(c)** Adhesive Scotch tape used for exfoliation. **(d)** Peeling off tape from SiO_2 wafer after exfoliation.

water.

2. **Preparation of tape with graphite .** While the wafer is baking, start preparing thin layers of graphite on adhesive tape (3M Scotch tape) (Fig. 3.1(**c**)). Firstly, a layer of adhesive tape is applied onto HOPG (Highly Ordered Pyrolytic Graphite, SPI Grade ZYA) crystal and peeled off. This tape will have a thick and smooth graphite sticking to it. Then repeatedly apply

another adhesive tape to this one, until a thin and smooth layer of graphite area can be seen on the tape.

3. **Graphene deposition and verification.** When Si wafer is done baking, gently lay down the tape that has thin graphite onto the wafer, and gently rub it using a carbon tip tweezers to get rid of air bubble. Thin layers graphene (single layer to multilayer) can be deposit onto Si wafer due the van de Waals force between graphene and SiO_2 surface is stronger than between graphene and graphene layers in graphite. After peeling off the tape, the Si wafer is moved to a Nikon optical microscope to hunt for single layer graphene (Fig. 3.2(**a**)). The amazing thing about graphene is that it is very stable in air even it has only one atomic layer, and this atomic layer can be optically identified by the optical contrast. Due to the interference effect, single layer graphene has a different contrast (slightly different color) compared to the bare SiO_2 substrate (Fig. 3.2(**b**)). Usually the smallest contract can be seen under the optical microscope is a good hint for single layer graphene, but not necessarily. Raman spectroscopy is needed to really distinguish single layer and possible bilayer graphene[193, 194]. Atomic Force Microscopy (AFM) alone is also not enough to determine single layer graphene. Experimentally the measured thickness for single layer graphene (confirmed by Raman) can vary from 0.5 - 2.0 nm, all depending on how strong graphene is bonded to the bottom substrate.

4. **Alignment markers.** After a nice single layer graphene (typically $\sim 2\times15$ μm, the surrounding area should be relatively clear to lay down electrodes) is identified, record the relative position of the flake respected to the top right corner of the wafer using the calibrated camera. This information will be used in later alignment mark step. Wafers with single layer graphene on top will be spin coated with MMA/PMMA bilayer resists (8.5 MAA EL9 MMA, 950 A4 PMMA from MicroChem) to achieve undercut. The coating speed for both resist are 3000 rpm (revolutions per minute) for 45 sec, using 500 rpm/min as the ramp rate. MMA is

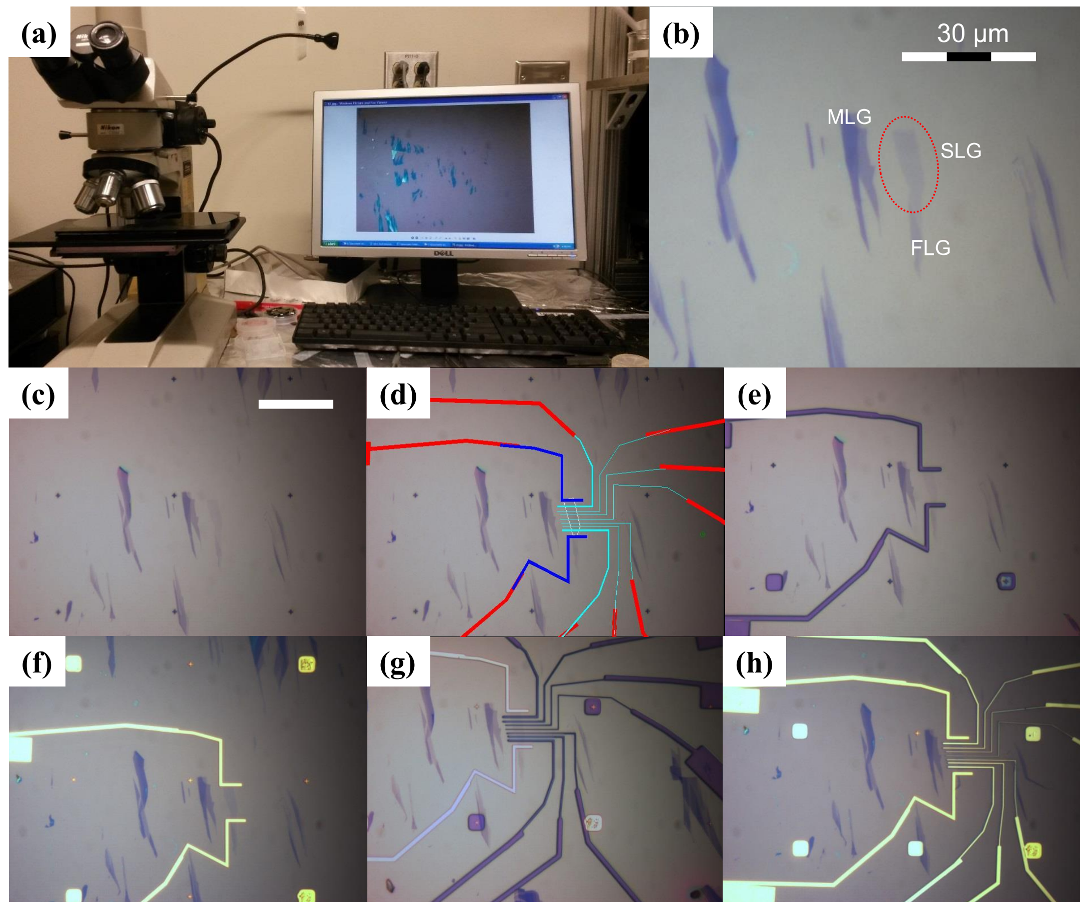

Figure 3.2: Optical image of the device after each metal deposition step. **(a)** Optical microscope to check for single layer graphene. **(b)** Exfoliated flakes with various thickness. The darker the color it is, the thicker the flake is. **(c)** Lay down alignment markers on MMA/PMMA (crosses in the image). Scale bars is 30 μm. **(d)** Design the layout of electrodes in DesignDAC software. **(e)** Use EBL to define Au electrodes. **(f)** Au contacts after metallization and lift off. **(g)** Use EBL to define Co electrodes. **(h)** Co contacts after deposition and lift off. **(d)** - **(f)** has the same image size with **(c)**.

firstly spin coated and baked at 150 °C for 2 min. PMMA is then spin coated on top of MMA and the whole substrate is baked at 170 °C for 10 - 20 min. The final thickness of MMA and PMMA is $\sim$ 300 nm and $\sim$ 200 nm, respetively. Alignment markers (crosses consisting of two perpendicular 0.1 $\times$ 2 μm bar) are lay down using electron beam lithography (EBL, from Zeiss or FEI) with electron energy of 20 or 10 keV, assisted with Nanometer Pattern Generation System (NPGS) program. The standard developer is using MIBK(Methyl isobutyl ketone) : IPA (3:1) solution for 1 min 20 sec, followed by IPA for 1 min. After this sample is blow dry with

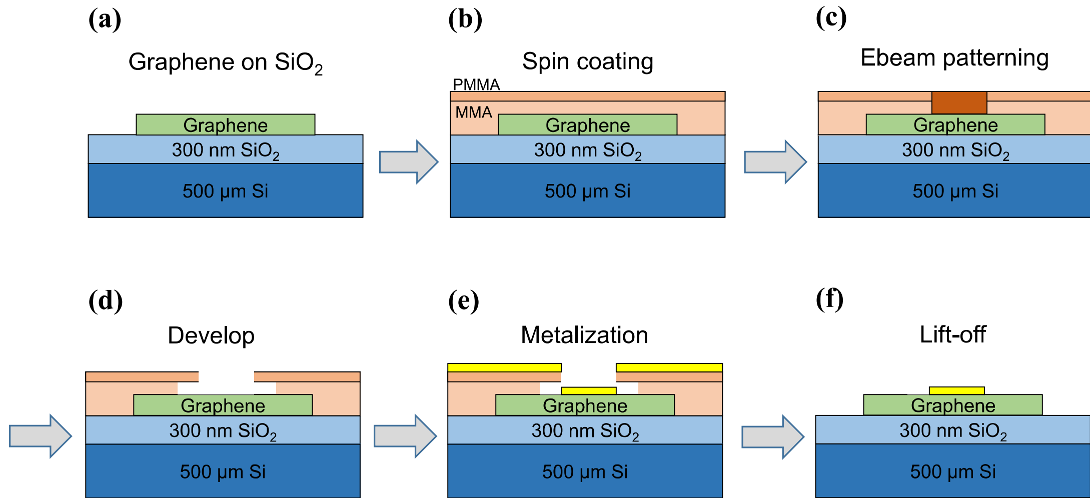

Figure 3.3: Diagram showing metal deposition steps. Double layer resist MMA/PMMA was used to form undercut in the exposed area, because MMA is easier to be developed wider than PMMA.

compressed nitrogen gas. Alignment markers are visible under optical microscope even without metallization (Fig. 3.2(**c**)).

5. **Ti/Au electrodes deposition.** Electrodes are firstly designed in DesignCAD based on optical image taken after the alignment mark step (Fig. 3.2(**d**)). For a typical graphene spin valves, we have both nonmagnetic (Ti/Au) and ferromagnetic (cobalt, Co) contacts. Nonmagnetic contacts are used for better Hanle precession measurement and elevated device yield. Ti/Au contacts have to be placed down in a separate lithography step from Co contacts. For this reason, Au (means Ti/Au) contacts pattern is firstly defined by EBL (Fig. 3.2(**e**)), then deposit in a high vacuum ($\sim 1 \times 10^{-6}$ Torr) environment from an ebeam evaporator. After Ti/Au (5/60 nm) deposition, the wafer is placed in a hot bath of Remover PG (proprietary N-Methyl Pyrrolidinone based solvent, from MicroChem) at 70 °C for $\sim$ 1 hour, followed by IPA rinse and nitrogen blow dry. The device optical image this step is show in Fig. 3.2(**f**). The schematic diagram of each of the contact deposition steps is given in Fig. 3.3.

6. **Vacuum anneal.** After the above Au contacts fabrication, the sample is annealed

in ultra-high vacuum (UHV) chamber (base presse 1×10^{-9} Torr) at 150 °C for 1 hour. This annealing step can get rid of (or partially) moisture and resist residue, and was found to increase device yield.

7. **Co electrodes patterning.** After vacuum anneal, a second MMA/PMMA ebeam resist is applied on the substrate using the same recipe described above. The alignment markers defined in Step 4 are still usable because there is Ti/Au deposited inside the crosses. These alignment markers are used to lay down Co pattern on graphene. After EBL patterning for Co electrodes and development, the sample is loaded into a molecular beam epitaxy (MBE, base pressure 1×10^{-10} Torr) chamber for tunnel barrier contacts deposition (Fig. 3.4). The width of Co electrodes is typically 150 - 500 nm in width. Each electrodes is designed to have a different width to give different coercive field.

8. **Co electrodes deposition.** Fig. 3.4**(a)** shows a picture of the MBE chamber. Reducing contacting area size between Co and graphene can lead to enhancement of spin accumulation[195]. For this reason, angle deposition is utilized to achieve this goal. Furthermore, to alleviate the conductance mismatch problem and achieve better electrical spin injection into graphene, MgO tunnel barrier is utilized[60]. Ti seeding layer, MgO tunnel barrier and Co ferromagnet are all grown *in-situ*. Firstly, 0.14 nm Ti is deposited at both 0° and 9° angle. This Ti layer is allowed to fully convert to TiO_2 by oxidizing in $\sim 5{\times}10^{-8}$ Torr molecular oxygen partial pressure. 0.9 nm MgO tunnel barrier is sequentially deposited at 9°, and 3 nm MgO masking layer is deposited deposited at 0° afterwards. Since 3 nm MgO has much bigger resistance than 0.9 nm MgO, the tunneling process happens at the 0.9 nm MgO interface. Finally, 80 nm Co is deposited at 7°. These angles are shown in Fig. 3.4**(c)**. The final contact structure is shown in Fig. 3.4**(d)**. In this deposition method, MgO is present only underneath the Co contacts. Ti is deposited from a homemade triode ebeam evaporator. MgO is evaporated from a

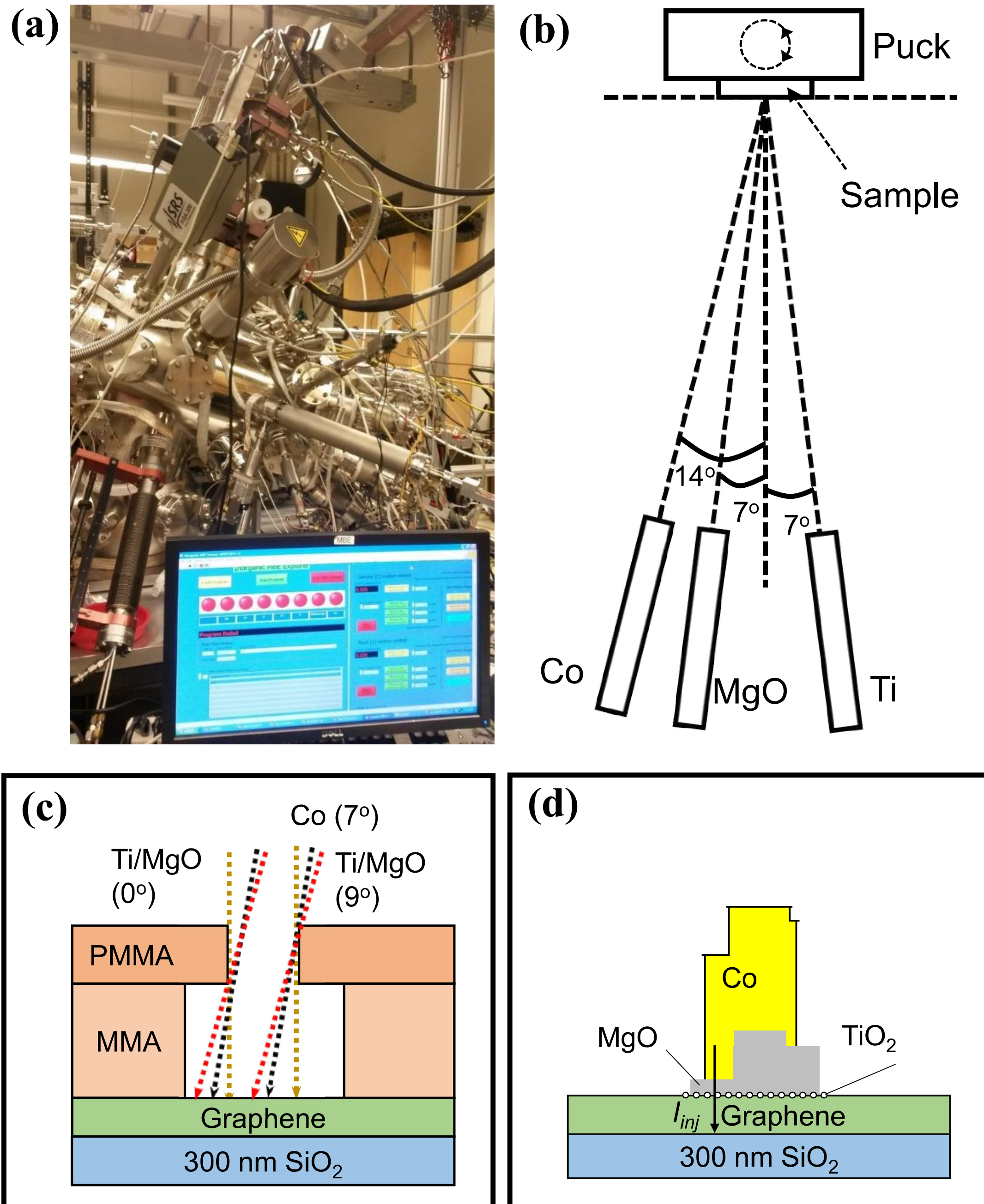

Figure 3.4: Angle deposition of MgO tunnel barrier in MBE chamber. **(a)** Picture of MBE chamber which MgO tunnel barrier and Co contacts are grown in. **(b)** Schematic diagram for relative angles of evaporators. Sample can be rotated around the axis perpendicular to the paper, thus different angle of materials deposition is achieved. **(c)** Diagram showing the angle deposition of Ti-seeded MgO tunnel barrier and Co contacts. **(d)** Final structure of the contacts after deposition.

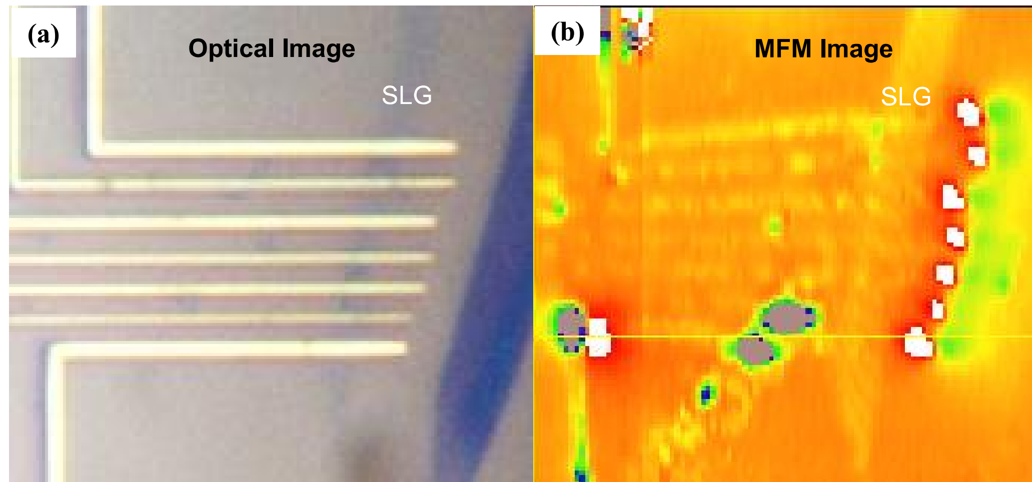

Figure 3.5: Optical and MFM image of a graphene spin valve device. Adapted from a manuscript in preparation. **(a)** Optical image of a graphene spin valve. **(b)** MFM image of the same device. The color indicates the frequency shift in MFM which corresponds to a combination of electrostatic force and magnetic force. When the image was taken, all the electrodes are magnetized in the same direction, giving a most strong magnetic force at the end of the Co electrodes.

commercial ebeam evaporator (from MDC Vacuum) where 4.8 keV energy electrons bombard a MgO crystal (12 mm diameter, 7 mm height, <100> oriented, fine ground on both sides). Co is evaporated from a homemade thermal effusion evaporator.

9. **Al_2O_3 capping.** After the Co deposition, sample is taken out from MBE chamber and loaded in an ebeam evaporator. 5 nm Al_2O_3 is deposited on top of Co, preventing it from oxidization. The device is then lift off in 70 °C Remover PG bath, followed by IPA rinse and nitrogen blow dry. A picture of final device is shown in Fig. 3.2**(h)**.

Note: We employed a 90° bend in the Co electrodes. The idea is to be able to treat the straight part of Co electrodes that is directly contacting graphene as a bar magnet. This idea is verified with magnetic force microscope (MFM) images show in Fig. 3.6, done by Dr. P. Chris Hammel's group (Department of Physics, The Ohio State University).

3.2 Electrical Measurement Setup

Magneto-transport measurement are performed on fabricated graphene spin valves. The electrical measurement system usually consists of the following components.

1. **Vacuum system.** Single layer graphene is sensitive to adsorbates in air. A good vacuum ($<1\times 10^{-5}$ Torr) is required to eliminate the hysteresis in measured quantities.

2. **Magnetic field.** External magnetic field is needed to perform basic spin transport measurement [1]. A minimum of two axis of magnetic fields are required: one is perpendicular to sample plane, the other is in sample plane. This can be achieved either by using rotatable sample, rotatable magnet, or two perpendicular magnets (Fig. 3.6(**b**)). The magnetic fields in both direction are preferred to be larger than 150 mT.

3. **Lock-in amplifier.** For graphene spin valves measurement, low frequency lock-in technic usually gives better signal-to-noise ratio (SNR), especially for high resistance contacts. DC measurement can also be used for spin valves measurement. A comparison of AC and DC measurement is show in Fig. 3.11. The lock-in used in this thesis is Signal Recovery Model 7265 Dual Phase DSP Lock-in Amplifier.

4. **Current source.** It is convenient and safer to source the device with current (set an appropriate voltage compliance). This current can be either AC or DC (AC is used in most of the experiments there). A common current source is Keithley 6221 AC and DC Current Source. We also use a homemade voltage-to-current converter as the current source. A combination of DC bias and AC modulation is desired to study bias dependence (see Chapter 5).

5. **Current shunt box.** Current shunt box is beneficial for the purpose of gradually increase the current in the device. Sudden change in the current or voltage in graphene spin

[1] In proposed mangeto-logic gate devices, no external magnetic field is required. Switching of electrodes are done using electrical current and spin transfer torque. This is an ongoing progress to integrate spin transfer torque in graphene spin valves.

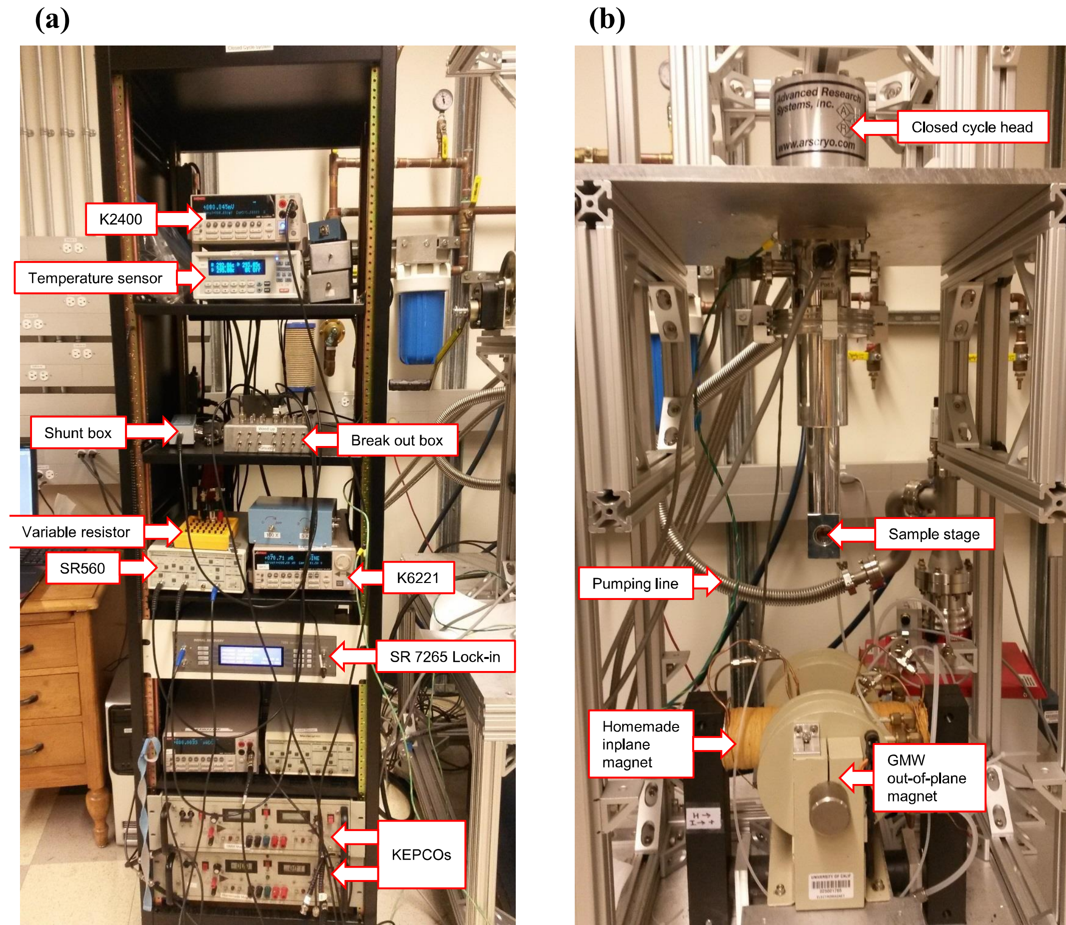

Figure 3.6: Magneto-transport measurement setup. **(a)** Electronic rack and mounted equipments. **(b)** Closed cycle system for sample containing and magnets. There are two axis of magnets which are powered by KEPCO power supplies.

valves can easily damage the contact and/or graphene. This is especially important when current source is floated (see Chapter 6). .

6. **DC voltage supply.** This is used to supply DC gate voltages on the devices to tune the carrier density inside graphene using field effect. A typical 'safe' gate voltage range is $-80 \rightarrow +60$ V for the Si wafer I was using. It if found that our wafer can handle larger negative gate voltages (can go to ~ -150 V before break down) than positive gate voltages (can go to +80 V before break down).

7. **Breakout box.** This is a standard component for connecting device to equipment using BNC (Bayonet-Neill-Concelman) connectors. There is corresponding switches (two-way

or three-way) for each connectors so the device can be connect to the system grounding point. This function is critical for preventing unexpected device break down especially for vulnerable tunnel barrier devices (discuss more in later of this chapter).

8. **SR 560 Low Noise Voltage Preamplifier.** This equipment is not absolutely necessary but it was found to improve the SNR in the measurement.

9. **Cryostat.** For temperature dependent studies (especially for temperatures lower than room temperature), a cryostat is needed to cool the sample. The cryostat used in this thesis is from Advanced Research Systems, Inc.

Fig. 3.6 shows the picture of electronics and cryostat discussed above. Fig. 3.7 shows the electronics connections for a nonlocal measurement. Electrical current is passing through E_2 and E_1, and voltage is measured between E_3 and E_4. E_1 is grounded. Back gate voltages are supplied by K2400.

3.3 Device Measurement Methodology

A easy way to understand the measurement methodology is to use a resistor network model (Fig. 3.8(**a**)). Electrodes E_1 and E_4 are Ti/Au electrodes and E_2 and E_3 are Co electrodes. They are four basic measurement configurations that are used to measure charge and spin transport properties in this graphene spin valve device. There is no different in terms of the measurement setup between using AC or DC, except for using different equipments. In the following discussion, AC is used to described the measurement as an representative example.

Config. 1 is measuring charge transport properties in graphene as a function of back gate voltages using a four probe geometry (Fig. 3.8(**b**)). Typically 1 μA AC current I_{AC} is applied between two outer Au contacts (E_1 and E_4) and AC voltage V_{AC} is detected between two Co electrodes in between (E_2 and E_3). The graphene resistance between the two Co elec-

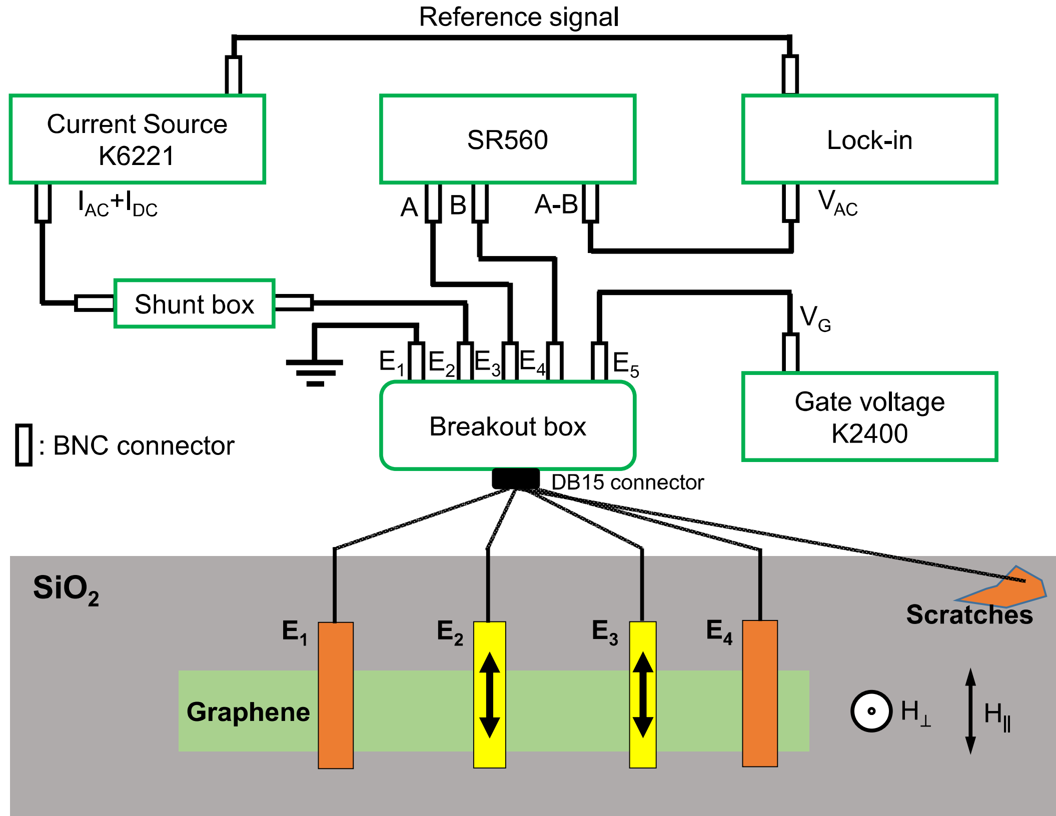

Figure 3.7: Equipment setup for nonlocal spin transport measurement with tunable back gate voltage.

trodes, R_{G23}, can be measured as $R_{G23} = V_{AC}/I_{AC}$. A typical graphene resistance is shown in Fig. 3.9(**a**). This configuration can efficiently eliminate the contact resistance, thus only measuring resistance of graphene. It has to be pointed out that these contacts are invasive, and contact induced doping and deformation in graphene could affect the measured charge and spin properties.

Config. 2 is measuring the contact resistance in a three probe geometry (Fig. 3.8(**c**)). Current $I = I_{AC} + I_{DC}$ is applied between E_2 and E_1, and voltage V_{AC} is measured between E_2 and E_4. The measured resistance $R_C = V_{AC}/I_{AC}$ is a sum of interfacial resistance of this contact, R_2 and wire resistance shared in the current and voltage loop ($\sim 100\ \Omega$). In a MgO tunnel barrier spin valves, contact resistance R_2 is on the order of several kΩ or higher. The small wire

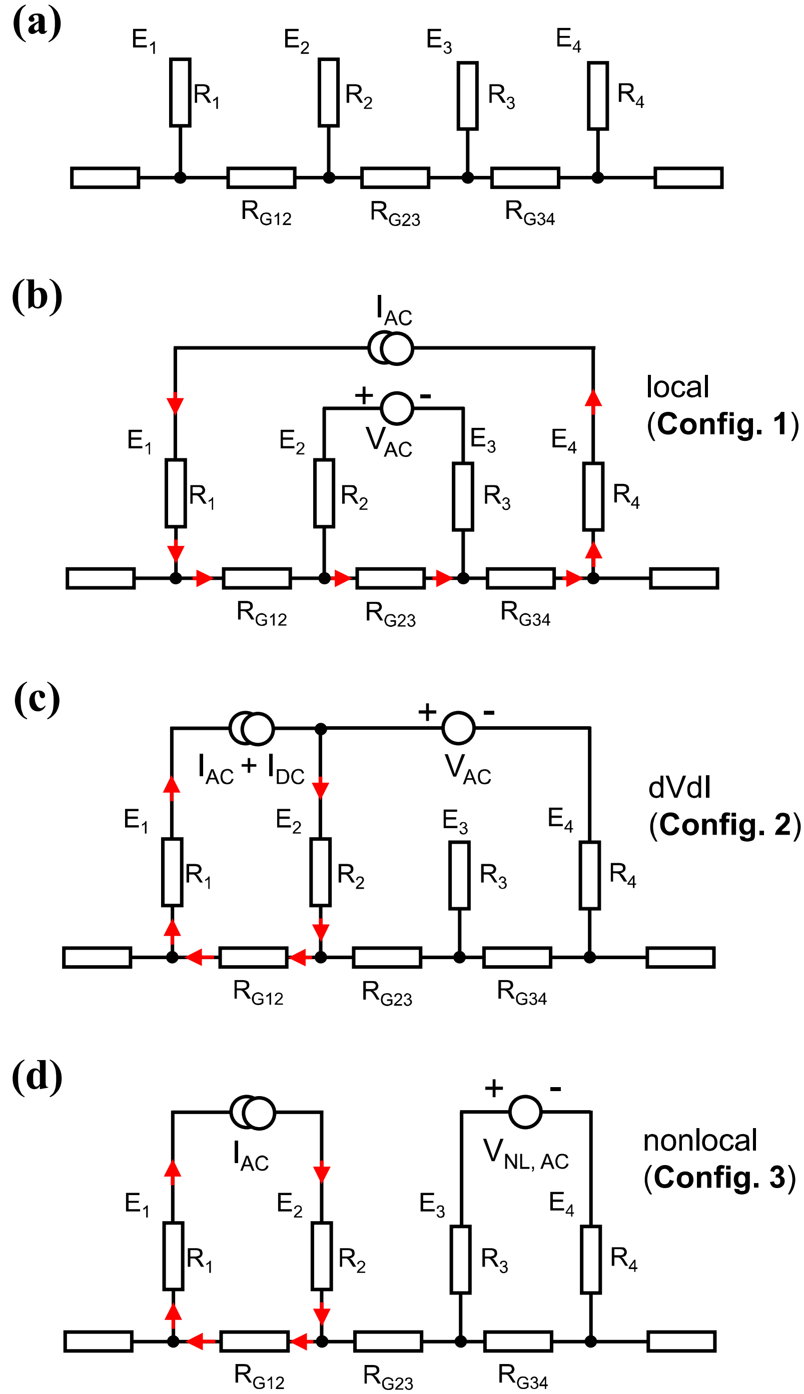

Figure 3.8: Diagram of different measurement setup. **(a)** Resistor network model for the device. R_1 - R_4 represent contact resistance (interfacial resistance) of the four contacts, E_1 - E_4, respectively. Graphene resistance between two contacts are labelled as R_{G12}, R_{G23} and R_{G34}. Red arrows indicate charge current flow with certain direction. **(b)** Local four probe measurement (**Config. 1**) to measure just graphene resistance. **(c)** Differential measurement (**Config. 2**) to measure just contact resistance. **(d)** Nonlocal measurement (**Config. 3**) to detect spin transport and precession.

resistance can be safely ignored and $R_2 \approx R_C$. R_2 is a function of DC bias current I_{DC}. For a typical tunnel barrier contact, R_2 is maximum when DC bias is zero, and smaller when DC bias gets larger (Fig. 3.9(**b**)). For graphene spin valves, this contact resistance is not so easy to control and has a significant various even on the same device undergoing the same fabrication process. It is also related to MgO thickness. Fig. 3.11(**b**) shows the measured R_C as a function of MgO tunnel barrier thickness for a assemble of samples. As can be seen, overall the contact resistance increases when MgO barrier gets thicker.

Config. 3 is measuring spin transport properties in a graphene spin valve which is the distinguishing feature from normal charge transport device. We utilize a nonlocal four probe geometry to separate spin transport path from charge transport path, as show in Fig. 3.8(**d**). Current I_{AC} is applied between E_2 and E_1 and an nonlocal voltage $V_{NL,\,AC}$ is detected between E_3 and E_4. In the low bias region (I_{AC} is small) V_{NL} is proportional to I_{AC}[2], so the figure of merit indicates the spin transport signal is usually defined as nonlocal resistance $R_{NL} = V_{NL,\,AC}/I_{AC}$. R_{NL} is a function of bias, gate voltage and temperature. An external magnetic field, H, is applied either along the long axis of Co electrodes or perpendicular to graphene plane. When H is along along Co electrodes long axis ($H_{||}$), the magnetization of Co electrodes can be switched to either direction, resulting a change of injected or detected spin accumulation. R_{NL} is found to have a sharp change when Co electrodes switches (Fig. 3.9(**c**)). The R_{NL} difference where there is a jump is defined as ΔR_{NL}, and it is related to the process that spins are injected and detected in graphene channel. A lower voltage level is always seen when E_2 and E_3 are antiparallel[3]. When H is applied out-of-plane ($H_\perp$), electron spins will process around the applied field $H_\perp$. Because spins are diffusive in graphene and reach the detector at different time, they phase will not be the

[2]The nonlinear behavior of V_{NL} with I_{AC} is further discussed in Chapter 5

[3]In some devices where the interface between Co electrodes and graphene is not so clean (possible residue from resist development), a higher voltage level can be observed for antiparallel configuration. This situation is discussed later in Chapter 5.

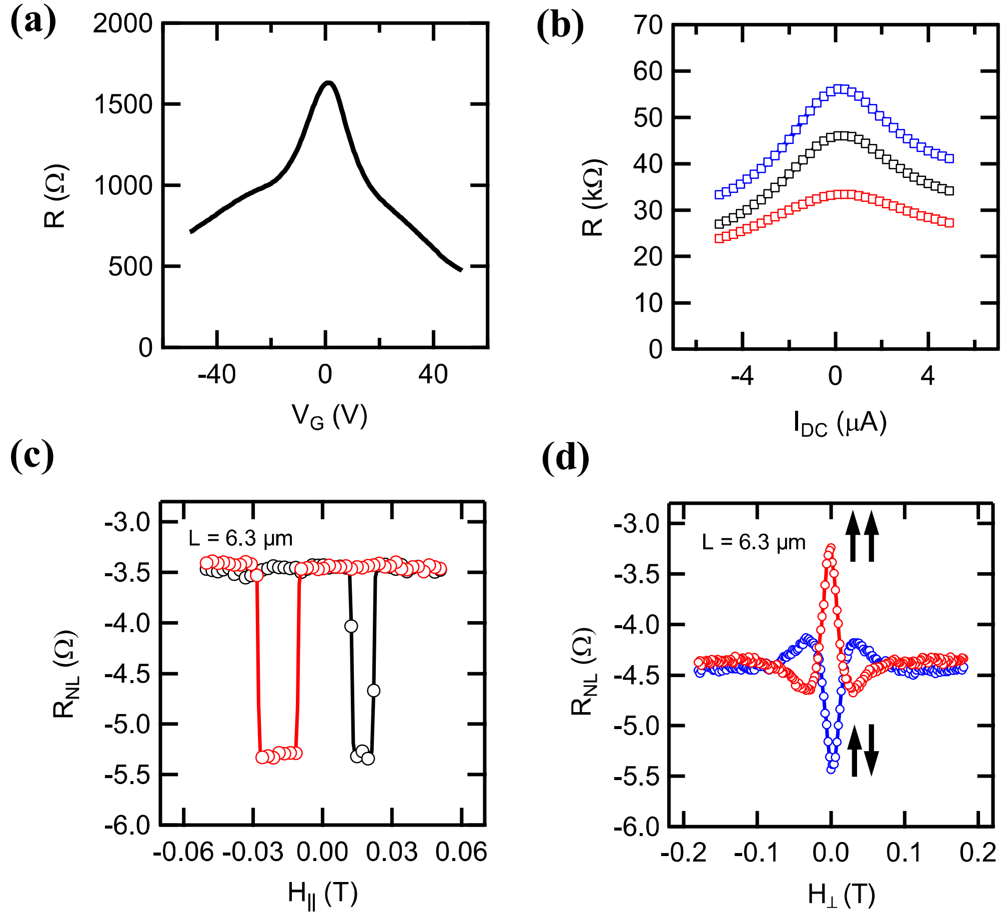

Figure 3.9: Measured graphene spin valve properties for the four different configurations at room temperature. **(a)** Measured graphene resistance in local four probe geometry as a function of gate voltage. **(b)** dVdI measurement of contact resistance for three different MgO tunnel barriers (indicated at three different color) at room temperatures. **(c)** Nonlocal MR R_{NL} measurement as a function of in plane magnetic field for a spin channel of 6.3 μm long. Black curve is sweeping magnetic field from negative to positive field, red curve is sweeping from positive to negative field. Clear two switchings is seen in both sweeping directions, indicating the measured signal is due to spins. **(d)** Nonlocal MR R_{NL} as a function of out-of-plane magnetic field. Clear Hanle precession signal is seen and the sign reverses when the injector and detector Co electrodes change from parallel configuration to anti-parallel configuration.

same. This causes an oscillation of the detected signal as well as decay of the magnitude when $H_{\perp}$ gets larger. The precession of spins can be detected up to at room temperature when spin injector and detector are set to parallel or antiparallel (Fig. 3.9(**d**)). By fitting the precession curve with existing model, important information such as spin lifetime τ_s and spin diffusion length λ_s, can be exacted from the fit.

3.4 Hanle Fitting

Theoretical models of spin precession in a diffusive materials have been developed to explain the observed Hanle precession. One commonly used model is given by the following equation[41]:

$$\Delta R_{NL} = S\int_0^{+\infty} \frac{1}{\sqrt{4\pi Dt}} e^{-L^2/4Dt} \cos(\omega_L t) e^{-t/\tau_s} dt \tag{3.1}$$

where S is Hanle amplitude, L is electrodes spacing, D is spin diffusion coefficient, $\omega_L = g_e\mu_B H_\perp/\hbar$ is Larmor precession frequency and τ_s is spin lifetime. From this equation parameters ($\tau_s, \lambda_s = \sqrt{D\tau_s}$) can be extracted. This equation considers the diffusive electron spins arrive at the detector at different time. At the same time spins precess in an external perpendicular magnetic field, so different spins acquire different phase. This causes a decay and change of sign in the detected signal. However, this model does not take the contact induced spin relaxation into account.

Recently, a new model was developed[196] to include contact induced spin relaxation. In this case the Hanle precession is described as:

$$\Delta R_{NL} = 2P^2 R_G f,$$

$$f = \mathrm{Re}\left(\left\{2\left[\sqrt{1+i\omega_L\tau_s} + \frac{\lambda_s}{2}\left(\frac{1}{r_0}+\frac{1}{r_L}\right)\right] e^{\frac{L}{\lambda_s}\sqrt{1+i\omega_L\tau_s}} + \frac{\lambda_s^2}{r_0 r_L}\frac{\sinh\left[\frac{L}{\lambda_s}\sqrt{1+i\omega_L\tau_s}\right]}{\sqrt{1+i\omega_L\tau_s}}\right\}^{-1}\right) \tag{3.2}$$

where P is the interfacial spin polarization, $R_G = \lambda_s/(W\sigma_G)$, $R_F = \rho_F\lambda_F/A_J$ is the spin resistance of ferromagnet, $r_i = (R_F + R_c^i)\sigma_G$, R_c^i is the contact resistance of contact i, and λ_s is spin diffusion length in graphene. By using this new fitting algorithm a more accurate spin lifetimes can be extracted.

When contact resistance is taken as infinite, Equation 3.2 gives exactly the same results as the Equation 3.1. When contact resistance gets smaller, the new fitting always give

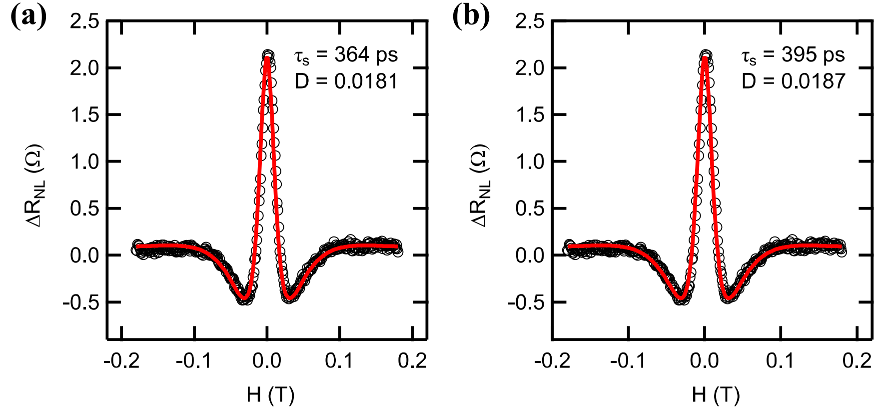

Figure 3.10: Comparision of the two Hanle fitting results on the data in 3.9**(d)**. **(a)** Hanle fitting using integral equation. **(b)** Hanle fitting using the new fitting. The unit of D in both graphs is m^2/s.

longer lifetime. An example is shown in Fig. 3.10 by comparing these two fitting results on a same data set. The contact resistance for spin injector and detector are 55 kΩ and 33 kΩ, respectively. When R_C is greater than 20 kΩ, the difference is small. Significant difference shows up when $R_C <1$ kΩ.

3.5 Some Notes on Graphene Spin Valves

3.5.1 DC and AC measurement

In our low measurement frequency region (10 Hz - 200 Hz), AC measurement is like a quasi-DC measurement. In the linear region AC measurement gives the same results as DC measurement. This is show in Fig. 3.11**(c) - (f)**. While AC measurement has much better SNR, the measured MR value for low current (1 μA) agrees well with DC measurement. When there is a DC bias, AC measurement is essentially probe the differential change in the spin accumulation at particular bias. So AC should be a differential measurement of DC, which is demonstrated in Fig. 3.11**(f)**.

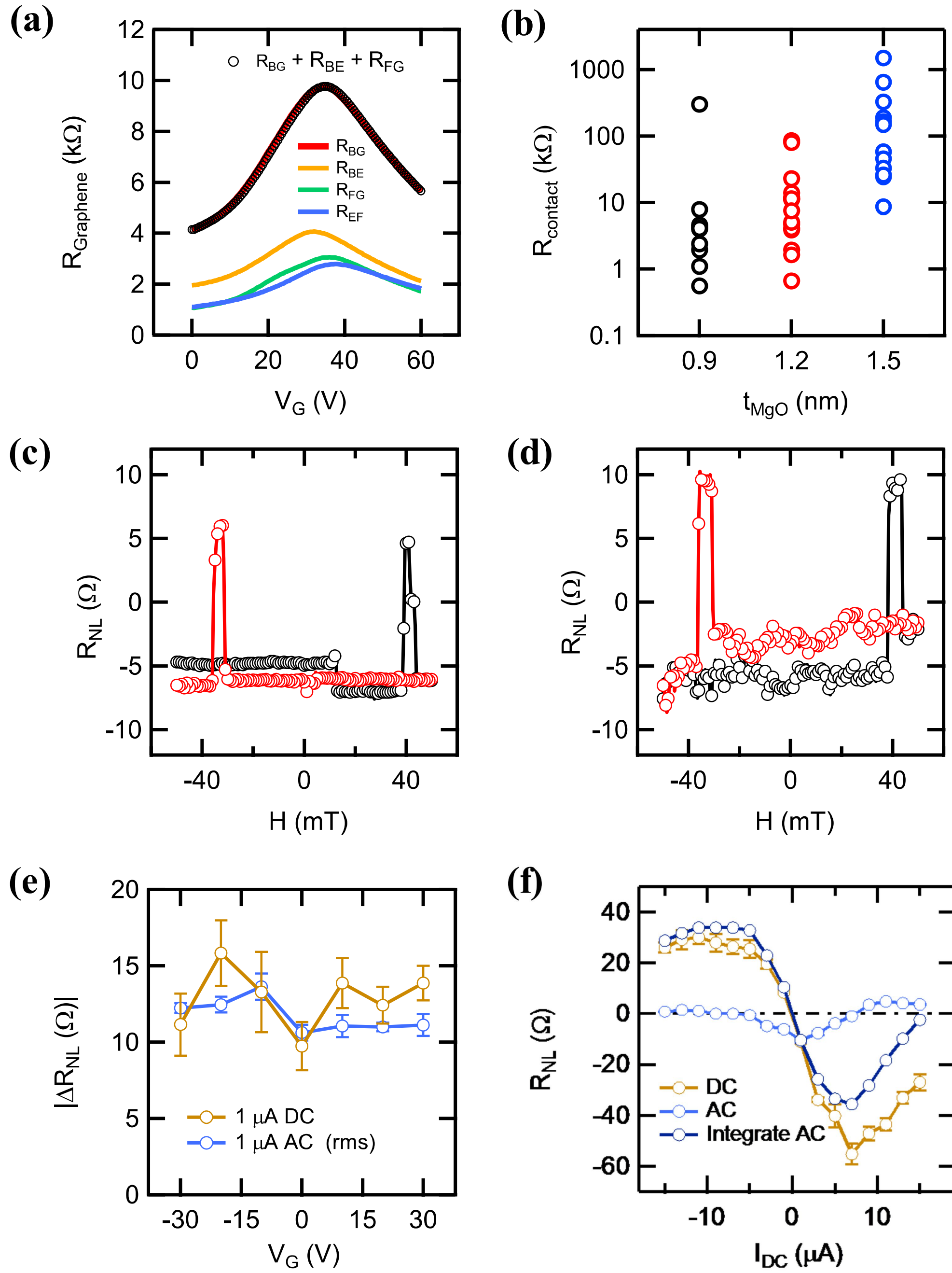

Figure 3.11: Some aspects about graphene spin valve measurement. **(a)** Measured graphene resistance discussed in section 3.3. Yellow, green and blue are three sequentially spaced graphene resistance measured using local four probe configuration. Red curve is measured resistance over all of the three graphene channel. **(b)** Contact resistance at zero bias for three different MgO tunnel barriers thickness (indicated at three different color) at room temperatures. **(c)** - **(d)** Non-local MR R_{NL} measured using 1 μA AC and 1 μA DC current at the same gate voltage and bias. **(e)** Measured ΔR_{NL} as a function of applied gate voltage for DC and AC measurement. **(f)** Measured ΔR_{NL} as a function of applied DC bias for DC and AC measurement.

3.5.2 Contact effect in graphene

I also want to note about graphene resistance measurement. Hall probe geometry is often used to get better measurement of graphene mobility. However, it is not compatible with graphene spin valves. Partially contacted Co electrodes has been seen to give Hall like signals when electrodes switches[55]. This is due to the strain field at the end of the Co electrodes, consistent with Fig. 3.5. So in all of our graphene spin valves, Co electrodes always cross the whole graphene flake. Nevertheless, four probe local measurement of graphene resistance is still quite good, though the contact may induce scattering in the graphene right underneath the contact. This is show in Fig. 3.11**(a)**. Here the measured resistance of a long graphene channel can be obtained in two ways: one is directly doing four probe measurement and get the resistance, the other is doing four probe measurement on each segment of the long graphene channel and sum up the resistance. The results shows they agree with each other very well.

3.5.3 Graphene device cleaning

After removing the ebeam resist (MMA, PMMA), the resist residue is unavoidably left on the graphene surface. It was shown that after lift-off atomic resolution on graphene on SiO_2 is not possible due to the polymer residue, and recovers after proper Ar/H_2 annealing[100]. So it is important to have clean graphene surface to achieve higher mobility electronic devices[107] and high sensitivity gas sensors[82].

Fig. 3.12 shows the AFM image of a graphene device on 300 nm SiO_2 substrate. Before applying any resist, as-exfoliated graphene on SiO_2 substrate shows flat surface with no observable residue. After life-off, clear residue can be seem on top of graphene. These residue are usually 2 -3 nm in height and several hundred nm in size. Ar/H_2 anneal on this device is done in tube furnace. Ar flow of 797 sccm and H_2 flow of 931 sccm was used as the gas flow.

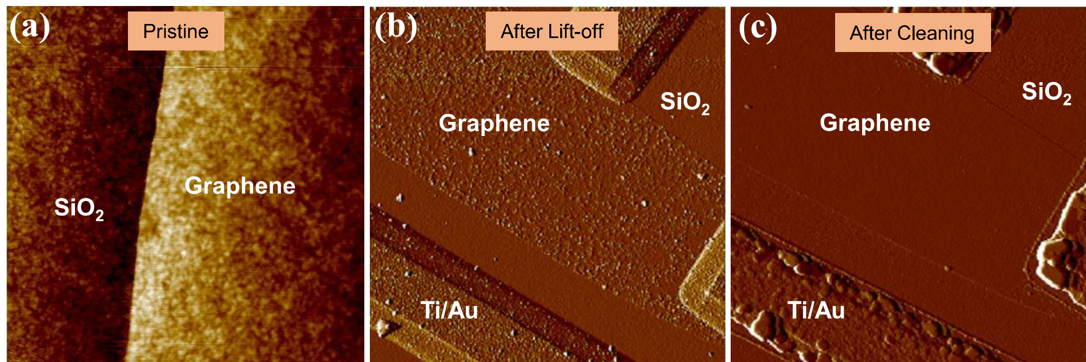

Figure 3.12: AFM image of a graphene device. **(a)** AFM image (Height Sensor) of a exfoliated graphene flake. RMS roughness of graphene flake and SiO_2 substrate are 0.204 nm and 0.212 nm, respectively. Size of the image is 1 μm. **(b)** AFM image (Amplitude Error) of a fabricated graphene device using MMA/PMMA resist and Remover PG to lift-off. Graphene is the middle stripe. Lots of residue can be seem on top of graphene. SiO_2 is relatively cleaner. Size of the image is 5 μm. **(c)** AFM image (Amplitude Error) of the same graphene device after Ar/H_2 anneal. Most of the residue on graphene is gone after anneal. Graphene surface is as flat or flatter than SiO_2 substrate. It should be noticed that Ti/Au electrodes has some deformation after the anneal. Size of the image is 5 μm.

Anneal temperature is 370 °C (thermocouple temperature outside the quartz tube is $\sim$ 350 °C) lasting for 3 hour. Temperature was found to be important to achieve the best annealing. During temperature ramping same Ar/H_2 flow was maintained. Fig. 3.12**(c)** shows the AFM image after anneal. Clean graphene surface was recovered.

It should be noted that this 370 °C Ar/H_2 anneal does affect metal contacts on graphene. Co contacts were found to loss spin sensitivity after Ar/H_2 at similar temperature[197].

3.5.4 MIBK vs IPA developer

The most common developer for exposed MMA/PMMA ebeam resistis is MIBK:IPA (1:3) developer, where MIBK is the main developer and IPA is added to reduce the development time for high precision. In our experiments, this developer (named as ‘MIBK Developer’) was found to introduce significant residue on the graphene surface (Fig. 3.13**(a)**). The size of AFM image is 1$\times$1 μm. Large amount of residues can be seen of size $\sim$ 50 - 200 nm, and $\sim$ 1 - 4 nm in height. These residues could be the reason to explain the big variation in graphene spin

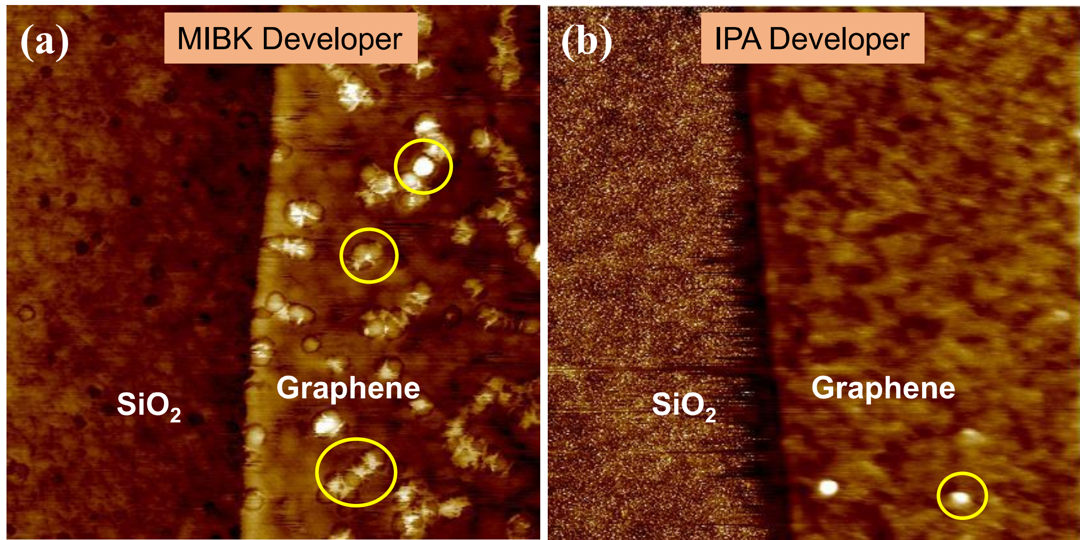

Figure 3.13: AFM image of a graphene after MIBK and IPA development. **(a)** AFM image (Height Sensor) of a graphene and SiO_2 surface after develop using MIBK Developer. Yellow circles indicate some of the residue on graphene surface. Size of the image is 1 μm. **(b)** AFM image (Height Sensor) of a graphene and SiO_2 surface after develop using IPA Developer. The surface has much less residue compared to **(a)**. Yellow circles indicate one of the residue on graphene surface.Graphene is the middle stripe.

valves.

It is interesting to note that IPA is a very slow developer for ebeam resist. Water does not develop at all. However, a mixture of IPA and water (named as 'IPA Developer') is an excellent developer for ebeam resist[198, 199], with better sensitivity and contrast. For this reason, mixture of IPA:water (3:1 volume ratio) was used to develop a graphene sample (Fig. 3.13**(b)**). The development time is 1 min 50 sec. Then sample is quickly removed out of the developer and blow dry with nitrogen. In the AFM image, only a small amount of residue was found. The rest is close to pristine graphene. How is this going to improve the device performance still needs more investigation.

Other ways to improve development include using ultrasonic during development[200], using cold developer[201] to give smaller patterns, etc.

Chapter 4

Current Detection of Spin Transport in Single Layer Graphene

This chapter will discuss the demonstration of current detection of spin transport in graphene[165], which is an important step towards realization of proposed magneto-logic gate. One-dimensional drift diffusion model is developed to explains the observed behavior. Detailed derivation of this model will be given. Based on this model, the optima device parameters are discussed.

4.1 Introduction

Graphene, a single atomic layer of carbon, has emerged as a leading candidate for spintronic applications due to its long spin diffusion length at room temperature[55, 202, 60, 138, 59, 197]. In addition, the incorporation of tunnel barriers into the junction between ferromagnetic electrodes and graphene has led to efficient spin injection[60]. Together these provide the physical basis for novel spintronic devices and circuits that integrate logic and non-volatile memory[203, 29, 204, 166]. This is especially attractive for applications that involve processing

large amounts of data such as searching, sorting, or data compression because the integration of logic and memory will avoid the von Neumann bottleneck, the high computational overhead associated with shuttling data back and forth between the central processing unit (CPU) and the memory through a small data bus[205].

One proposed implementation of spin-based logic has been developed by Dery and coworkers[29, 166]. This involves magnetologic gate (MLG) with five ferromagnetic electrodes on a graphene spin channel. All of the critical spin transport processes have been demonstrated in the traditional nonlocal spin valve measurement[55, 202, 60, 138, 59, 197] except for the current-based detection of spin accumulation. For the proposed spintronic circuits, a current-based detection scheme is required because it enables hundreds of MLG devices to connected together prior to the spin-to-CMOS conversion[168, 166].

In this chapter, we report the current-based detection of spin accumulation in graphene nonlocal spin valves. By using a variable shunt resistor (R_{sense}), we systematically tune the spin detection from a voltage-based measurement ($R_{sense} \to +\infty$) to a current-based measurement ($R_{sense} \to 0$). Spin signals with good signal-to-noise are observed throughout the entire range. The results are analyzed within the framework of one-dimensional drift-diffusion modeling. These results provide the experimental and theoretical foundation for current-based detection of nonlocal spin transport.

4.2 Experimental Results

We utilize a nonlocal spin valve (Fig. 4.1(**a**)) consisting of a single layer graphene spin channel on SiO_2(300 nm)/Si substrate, two inner ferromagnetic electrodes that act as spin injector and spin detector (electrodes E_2 and E_3, respectively), and two outer non-magnetic Ti/Au electrodes (electrodes E_1 and E_4). The ferromagnetic contacts consist of a Co electrode

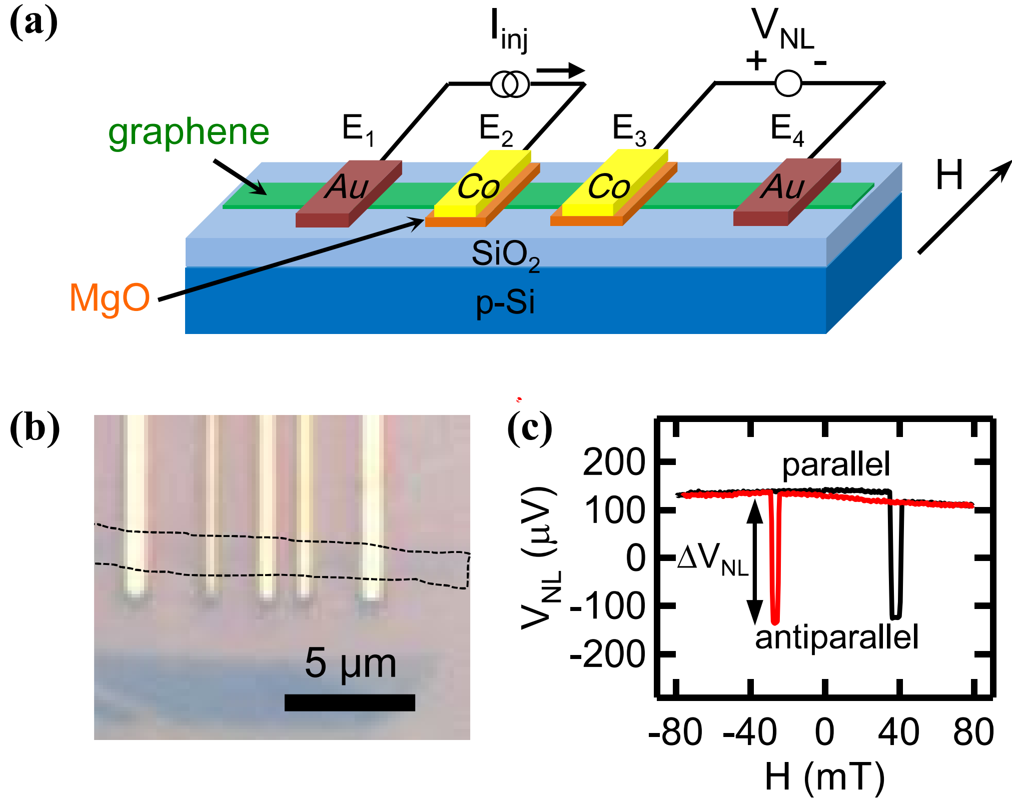

Figure 4.1: Nonlocal spin valve measurement. **(a)** Device structure for nonlocal graphene spin valves. **(b)** Optical image of a spin valve with three inner Co electrodes (only two are used for measurement) and two outer Au electrodes. The dashed black line indicates the boundary of the single layer graphene. **(c)** Nonlocal spin signal. The black curve is obtained by sweeping magnetic field H from - 80 mT to + 80 mT and red curve is obtained by sweeping H from + 80 mT to - 80 mT.

on a Ti-seeded MgO tunnel barrier on graphene[60]. The devices are fabricated by electron-beam lithography and the process is described in detail in [136, 152] and Chapter 3. An optical microscope image of a completed device is shown in Fig. 4.1(**b**).

We begin by performing the traditional nonlocal spin valve measurement[38, 40] at T = 10 K. A current source across electrodes E_1 and E_2 provides a current (I_{inj}) to inject spin-polarized electrons into the graphene at E_2. These spins diffuse as a pure spin current toward detector electrode E_3, where it is detected as the 'nonlocal' voltage (V_{NL}) across electrodes E_3 and E_4. The voltage is measured with standard lock-in techniques using $I_{inj} = 10\ \mu$A AC (13 Hz)

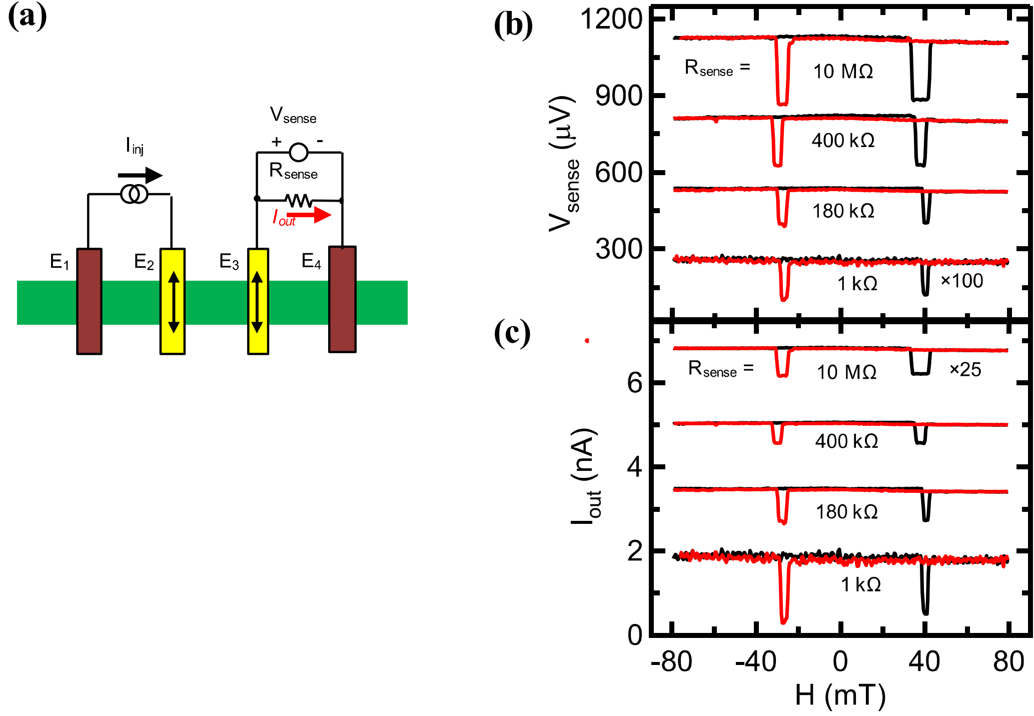

Figure 4.2: Nonlocal measurement with a variable sensing resistor R_{sense}. **(a)** Device structure with an additional sensing resistor R_{sense} between E_3 and E_4. **(b)** Measured voltage V_{sense} across resistor R_{sense} for different R_{sense} values (top to bottom): 10 MΩ, 400 $k\Omega$, 180 $k\Omega$, and 1 $k\Omega$. **(c)** I_{out} plotted as a function of magnetic field for different R_{sense} values.

as the excitation. By sweeping an in-plane magnetic field to reverse the magnetizations of the ferromagnetic electrodes, the parallel and antiparallel magnetization alignments of the injector (E_2) and detector (E_3) are achieved. The difference in V_{NL} between the parallel ($V_{NL,P}$) and antiparallel ($V_{NL,AP}$) states represents the spin transport signal ($\Delta V_{NL} = V_{NL,P} - V_{NL,AP}$). There is generally a non-zero average background level, $(V_{NL,P}+V_{NL,AP})/2$, that is unrelated to spin and therefore subtracted out. Fig. 4.2**(c)** shows the nonlocal voltage as the magnetic field is ramped up (black line) and ramped down (red line). The higher level for V_{NL} corresponds to the parallel magnetization state, while the lower level corresponds to the antiparallel magnetization state. The observed change in V_{NL} is 250 μV, which corresponds to a nonlocal magnetoresistance of 25 Ω when normalized by the 10 μA injection current.

To investigate the current-based detection of the nonlocal spin signal, we add a vari-

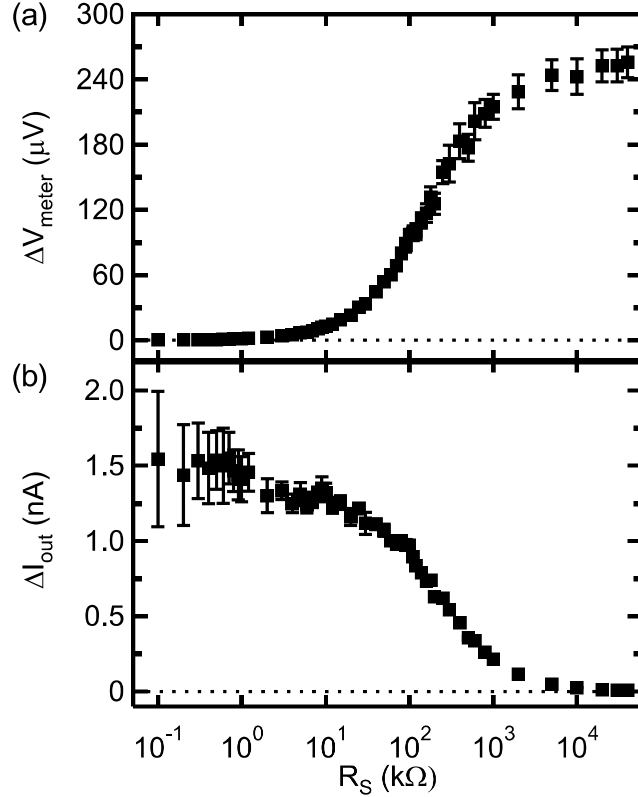

Figure 4.3: Voltage and current detection signal as a function of R_{sense}. **(a)** Detected voltage signal (ΔV_{sense}) as a function of R_{sense}. **(b)** Detected current signal (ΔI_{out}) as a function of R_{sense}.

able shunt resistor (R_{sense}) in parallel to the voltmeter, whose measured voltage can be different from V_{NL} and is denoted as V_{sense} (Fig. 4.2(**a**)). In the limit of $R_{sense} \rightarrow +\infty$, this reverts to the standard nonlocal measurement and $V_{sense} = V_{NL}$. In the limit of $R_{sense} \rightarrow 0$, the resistor acts as a low impedance current meter with current given by $I_{out} = V_{sense}/R_{sense}$ (Fig. 4.2(**a**)). Fig. 4.2(**b**) shows the spin transport measurement (V_{sense} vs. H) for four different values of R_{sense} (10 MΩ, 400 $k\Omega$, 180 $k\Omega$, and 1 $k\Omega$). The curves are offset for clarity and the data for R_{sense}=1 $k\Omega$ is magnified by 100$\times$. Notably, as R_{sense} gets smaller, the magnitude of the voltage-based spin signal also reduces. Fig. 4.2(**c**) shows the same data after converted to an output current (I_{out}). In this case, as R_{sense} gets smaller, the current-based spin signal ΔI_{out} becomes larger. Note that in Fig. 4.2(**c**) the data for R_{sense} =10 $M\Omega$ has been magnified by 25$\times$.

For a quantitative understanding of the current-based measurement, we perform the

spin transport measurement as a detailed function of R_{sense}.Fig. 4.3**(a)** shows ΔV_{sense} as a function of R_{sense}, while Fig. 4.3**(b)** shows ΔI_{out} as a function of R_{sense}. When R_{sense} is high, the spin signal ΔV_{sense} is large and ΔI_{out} is small, while for low R_{sense}, the spin signal ΔV_{NL} is small and ΔI_{out} is large. The crossover between the two limits occurs at $R_{sense} \sim 180\ k\Omega$, and the values of ΔV_{sense} and ΔI_{out} converge to stable levels away from this crossover region. For large values of R_{sense}, V_{sense} approaches the voltage-based spin signal ΔV_{NL}. For small value of R_{sense}, ΔI_{out} approaches a finite value which is the current-based spin signal, which we denote as ΔI_{NL}.

4.3 Theoretical Analysis

We investigate the current-based measurement theoretically by employing the one-dimensional drift-diffusion analysis following the approach of Takahashi and Maekawa[44]. Fig. 4.4 shows the structure for the spin injection and detection. FM electrode F1 is the spin injector and F2 is the spin detector. N is the nonmagnetic spin transport channel (graphene channel in our case). Assuming the length of N in x direction is long compared to spin diffusion length in N, so the spin density decay to zero at each end of N. The width of F1 and F2 are w_F, the width of N is w_N. Distance between F1 and F2 is L. FMs are 3D contacts with dimension $A_J = w_F \times w_N$ in $x-y$ plane. In z direction, FM is thick enough so the spins decay to zero inside FM when away from $z = 0$. The derivation below is following the procedure discussed in [44], except there is an extra equation needs to be added.

Electron spins are injected into N by passing electrical current I_{inj} from F1 to the left end of N. A voltage V_{NL} (voltage detection) or current signal I_{out} (current detection) can be detected between F2 and the right end of N. Considering spin-σ ($\sigma =\uparrow,\downarrow$) current flow inside a material, the corresponding current $\mathbf{j}_\sigma$ can be written as:

$$\mathbf{j}_\sigma = -\frac{\sigma_\sigma}{e}\nabla\mu_\sigma \tag{4.1}$$

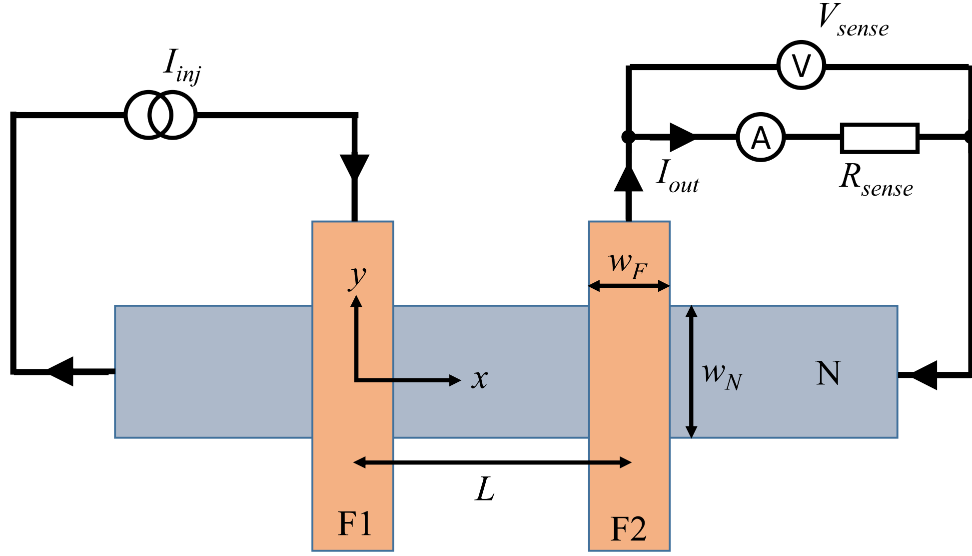

Figure 4.4: Structure of spin injection and detection in a nonmagnetic channel (N) using two ferromagnets, F1 and F2. F1 is injector and F2 is detector. Electrical current (I_{inj}) is injected from F1. Current signal (I_{out}) is detected from F2.

where σ_σ is the conductivity for spin σ, $\mu_\sigma = \varepsilon_\sigma + e\phi$ is the electrochemical potential for spin-σ. The continuity equations for charge and spin in the steady state are:

$$\nabla \cdot (\mathbf{j}_\uparrow + \mathbf{j}_\downarrow) = 0 \tag{4.2}$$

$$\nabla \cdot (\mathbf{j}_\uparrow - \mathbf{j}_\downarrow) = -e\delta n_\uparrow / \tau_{\uparrow\downarrow} + e\delta n_\downarrow / \tau_{\downarrow\uparrow} \tag{4.3}$$

where $\delta n_\sigma = N_\sigma \delta\varepsilon_\sigma$ is the spin-σ density deviation from equilibrium. Using detailed balancing condition $N_\uparrow/\tau_{\uparrow\downarrow} = N_\downarrow/\tau_{\downarrow\uparrow}$, the above two equations can be rewritten as:

$$\nabla^2(\sigma_\uparrow \mu_\uparrow + \sigma_\downarrow \mu_\downarrow) = 0 \tag{4.4}$$

$$\nabla^2(\mu_\uparrow - \mu_\downarrow) = \lambda^{-2}(\mu_\uparrow - \mu_\downarrow) \tag{4.5}$$

where $\lambda = \sqrt{D\tau_s}$, $\tau_s = \frac{1}{2}(\tau_{\uparrow\downarrow}^{-1} + \tau_{\downarrow\uparrow}^{-1})$ and $D^{-1} = (N_\uparrow D_\downarrow^{-1} + N_\downarrow D_\uparrow^{-1})/(N_\uparrow + N_\downarrow)$. Use λ_N and λ_F to note the spin diffusion length in N and FM, respectively. In nonmagnet N: $\sigma_N^\uparrow = \sigma_N^\downarrow = \frac{1}{2}\sigma_N$, $D_\uparrow = D_\downarrow$. In ferromagnets F1 and F2: $\sigma_F^\uparrow \neq \sigma_F^\downarrow$, $D_\uparrow \neq D_\downarrow$.

It has to be pointed out that due to the 2D nature of graphene, conductivity σ_N is defined different from conductivity σ_F inside FM. In the conventional 3D materials, the resistance is give by $R = \rho \frac{L}{A} = \frac{L}{\sigma A}$, and σ has the unit of $[\Omega^{-1}m^{-1}]$. in the case of graphene, resistance is defined as $R = \rho_G \frac{L}{W} = \frac{L}{\sigma_G W}$. Here σ_G has the unit of $[\Omega^{-1}]$.

4.3.1 Calculate spin and charge current inside channel N

Spins are electrically injected (I_{inj}) from F1 to nonmagnet (N) across a junction area $A_J = w_F \times w_N$. On the left of N (x<0), there is spin polarized current I_{inj} flowing from F1 to the left end of N. For region x>0, there is only diffusive spin current. This diffusive spin current is pickup at $x = L$ by F2. In the current detection region, there is a charge current I_{out} flowing from F2 to outside current detection loop to the right end of N. Based on the the Eqs. 4.4 and Eqs. 4.5, one can construct the electrochemical potential inside N and FM. In the N, when contact dimension is much smaller than λ_N, spin transport inside N can be treated as uniform in y direction. So μ_N is only a function of x:

$$\mu_N^\sigma(x) = \begin{cases} \frac{eI_{inj}}{\sigma_N w_N}x + \sigma a_1 e^{x/\lambda_N} + \sigma a_2 e^{(x-L)/\lambda_N}, & x < 0 \\ \sigma a_1 e^{-x/\lambda_N} + \sigma a_2 e^{(x-L)/\lambda_N}, & 0 < x < L \\ \frac{eI_{out}}{\sigma_N w_N}(x-L) + \sigma a_1 e^{-x/\lambda_N} + \sigma a_2 e^{-(x-L)/\lambda_N}, & x > L \end{cases} \tag{4.6}$$

In the case that channel N is graphene, the electrical current I^σ for spin-σ is given by $I^\sigma = -\frac{\sigma_N^\sigma w_N}{e}\nabla\mu_N^\sigma(x)$. So the current inside graphene for $x < 0$ region is given by:

$$I_N^\sigma = -\frac{\sigma_N^\sigma w_N}{e}\left[\frac{eI_{inj}}{\sigma_N w_N} + \frac{\sigma a_1}{\lambda_N}e^{x/\lambda_N} + \frac{\sigma a_2}{\lambda_N}e^{(x-L)/\lambda_N}\right] \tag{4.7}$$

For $0 < x < L$:

$$I_N^\sigma = -\frac{\sigma_N^\sigma w_N}{e}\left[-\frac{\sigma a_1}{\lambda_N}e^{-x/\lambda_N} + \frac{\sigma a_2}{\lambda_N}e^{(x-L)/\lambda_N}\right] \tag{4.8}$$

For $x > L$:

$$I_N^\sigma = -\frac{\sigma_N^\sigma w_N}{e}\left[\frac{eI_{out}}{\sigma_N w_N} - \frac{\sigma a_1}{\lambda_N}e^{-x/\lambda_N} - \frac{\sigma a_2}{\lambda_N}e^{(x-L)/\lambda_N}\right] \tag{4.9}$$

Spin current is calculated as $I^s = I^{\uparrow} - I^{\downarrow}$. On the left of contact 1 inside channel N, the total charge current is $-I_{inj}$, the spin current is:

$$I^s|_{x\to 0^-} = -\frac{\sigma_N w_N}{e\lambda_N}(a_1 + a_2 e^{-L/\lambda_N}) \tag{4.10}$$

On the right of contact 1, the total charge current is 0, the spin current is:

$$I^s|_{x\to 0^+} = -\frac{\sigma_N w_N}{e\lambda_N}(-a_1 + a_2 e^{-L/\lambda_N}) \tag{4.11}$$

On the left side of contact 2, the total charge current is 0, the spin current is:

$$I^s|_{x\to L^-} = -\frac{\sigma_N w_N}{e\lambda_N}(-a_1 e^{-L/\lambda_N} + a_2) \tag{4.12}$$

On the right side of contact 2, the total charge current is $-I_{out}$, the spin current is:

$$I^s|_{x\to L^+} = -\frac{\sigma_N w_N}{e\lambda_N}(-a_1 e^{-L/\lambda_N} - a_2) \tag{4.13}$$

4.3.2 Calculate spin and charge current inside FM

Inside FM, the spins decay along z axis. Define the positive direction of the current is along $+z$ (away from $x-y$ plane). So the total charge current in contact 1 is $-I_{inj}$, the total current in contact 2 is $+I_{out}$. Inside F1 and F2, electrochemical potential for spin-up and spin-down can be written as:

$$\mu_{F1}^{\sigma}(z) = \frac{eI_{inj}}{\sigma_F A_J} z + eV_1 + \sigma b_1 \frac{\sigma_F}{\sigma_F^{\sigma}} e^{-z/\lambda_F} \tag{4.14}$$

$$\mu_{F2}^{\sigma}(z) = -\frac{eI_{out}}{\sigma_F A_J} z + eV_2 + \sigma b_2 \frac{\sigma_F}{\sigma_F^{\sigma}} e^{-z/\lambda_F} \tag{4.15}$$

where V_1 and V_2 are the electrochemical potential drop across the interface 1 and 2, respectively. Inside F1 close to the contact 1 interface ($z \to 0^+$), the spin-σ current $I_{F1}^{\sigma} = -\frac{\sigma_F^{\sigma} A_J}{e} \nabla \mu_{F1}^{\sigma}(z)$ is:

$$I_{F1}^{\sigma}|_{z\to 0^+} = -\frac{\sigma_F^{\sigma} A_J}{e}\left(\frac{eI_{inj}}{\sigma_F A_J} - \frac{\sigma b_1}{\lambda_N}\frac{\sigma_F}{\sigma_F^{\sigma}}\right) \tag{4.16}$$

The total charge current is $I_{F1}^c = I_{F1}^\uparrow + I_{F1}^\downarrow = -I_{inj}$. The spin current $I_{F1}^s = I_{F1}^\uparrow - I_{F1}^\downarrow$ is:

$$I_{F1}^s = -p_F I_{inj} + \frac{2b_1\sigma_F A_J}{e\lambda_N} \quad (4.17)$$

where $P_F = \frac{\sigma_F^\uparrow - \sigma_F^\downarrow}{\sigma_F^\uparrow + \sigma_F^\downarrow}$ is the spin polarization of the FM. Calculating in the same way, the charge current at interface 2 is $I_{F2}^c = I_{F2}^\uparrow + I_{F2}^\downarrow = I_{out}$. The spin current inside F2 is:

$$I_{F2}^s = p_F I_{out} + \frac{2b_2\sigma_F A_J}{e\lambda_N} \quad (4.18)$$

4.3.3 Interfacial charge and spin current

Interfacial spin-flip scattering is neglected, so spin-up and spin-down current are conserved at the interface. The interfacial current I_i^σ is given by:

$$I_i^\sigma = \frac{G_i^\sigma}{e}(\mu_{Fi}^\sigma|_{z=0^+} - \mu_{Ni}^\sigma|_{z=0^-}) \quad (4.19)$$

where $G_i^\uparrow + G_i^\downarrow = G_i = 1/R_i$, G_i is the conductivity for spin-σ, R_i is the interfacial resistance. **Note: in this definition, the direction of the current is assumed to be along $-z$, so it has a negative sign compared to the current in FM when using continuity condition in the next section.** Interfacial current polarization is given by $P_i = \frac{G_i^\uparrow - G_i^\downarrow}{G_i^\uparrow + G_i^\downarrow}$. Spin-$\sigma$ current at interface 1 can be written as:

$$I_1^\sigma = \frac{G_1^\sigma}{e}\left[eV_1 + \sigma b_1 \frac{\sigma_F}{\sigma_F^\sigma} - \sigma(a_1 + a_2 e^{-L/\lambda_N})\right] \quad (4.20)$$

At interface 2:

$$I_2^\sigma = \frac{G_2^\sigma}{e}\left[eV_2 + \sigma b_2 \frac{\sigma_F}{\sigma_F^\sigma} - \sigma(a_1 e^{-L/\lambda_N} + a_2)\right] \quad (4.21)$$

The interfacial charge and spin current are give by $I_i^c = I_i^\uparrow + I_i^\downarrow$, $I_i^s = I_i^\uparrow - I_i^\downarrow$, respectively. So the charge current at the two interfaces are:

$$I_1^c = I_1^\uparrow + I_1^\downarrow = G_1 V_1 + \frac{b_1\sigma_F}{e}\left(\frac{G_1^\uparrow}{\sigma_F^\uparrow} - \frac{G_1^\downarrow}{\sigma_F^\downarrow}\right) - \frac{G_1 P_{J1}}{e}(a_1 + a_2 e^{-L/\lambda_N}) \quad (4.22)$$

$$I_2^c = I_2^\uparrow + I_2^\downarrow = G_2 V_2 + \frac{b_2\sigma_F}{e}\left(\frac{G_2^\uparrow}{\sigma_F^\uparrow} - \frac{G_2^\downarrow}{\sigma_F^\downarrow}\right) - \frac{G_2 P_{J2}}{e}(a_1 e^{-L/\lambda_N} + a_2) \quad (4.23)$$

The spin current at the two interfaces are:

$$I_1^s = I_1^{\uparrow} - I_1^{\downarrow} = G_1 P_1 V_1 + \frac{b_1 \sigma_F}{e}\left(\frac{G_1^{\uparrow}}{\sigma_F^{\uparrow}} + \frac{G_1^{\downarrow}}{\sigma_F^{\downarrow}}\right) - \frac{G_1}{e}(a_1 + a_2 e^{-L/\lambda_N}) \tag{4.24}$$

$$I_2^s = I_2^{\uparrow} - I_2^{\downarrow} = G_2 P_2 V_2 + \frac{b_2 \sigma_F}{e}\left(\frac{G_2^{\uparrow}}{\sigma_F^{\uparrow}} + \frac{G_2^{\downarrow}}{\sigma_F^{\downarrow}}\right) - \frac{G_2}{e}(a_1 e^{-L/\lambda_N} + a_2) \tag{4.25}$$

4.3.4 Continuity conditions

The equations are connected through charge and spin current conservation. The spin-σ current is conserved across the two interfaces: $I_{FM} = I_{interface} = I_N$. Define the $+z$ and $+x$ direction as positive for the current. Based on Eqs. 4.10 and Eqs. 4.11, the spin current inside the N at interface 1 that goes from N to interface 1 is $I^s|_{x\to 0^-} - I^s|_{x\to 0^+} = -\frac{2\sigma_N w_N a_1}{e\lambda_N}$. Similarly, based on Eqs. 4.12 and Eqs. 4.13, spin current that goes into interface 2 is $I^s|_{x\to L^-} - I^s|_{x\to L^+} = -\frac{2\sigma_N w_N a_2}{e\lambda_N}$. The continuity of spin current across interface 1 gives:

$$-\frac{2\sigma_N w_N a_1}{e\lambda_N} = -p_F I_{inj} + \frac{2b_1 \sigma_F A_J}{e\lambda_N} = -\left[G_1 P_1 V_1 + \frac{b_1 \sigma_F}{e}\left(\frac{G_1^{\uparrow}}{\sigma_F^{\uparrow}} + \frac{G_1^{\downarrow}}{\sigma_F^{\downarrow}}\right) - \frac{G_1}{e}(a_1 + a_2 e^{-L/\lambda_N})\right] \tag{4.26}$$

At interface 2:

$$-\frac{2\sigma_N w_N a_2}{e\lambda_N} = p_F I_{out} + \frac{2b_2 \sigma_F A_J}{e\lambda_N} = -\left[G_2 P_2 V_2 + \frac{b_2 \sigma_F}{e}\left(\frac{G_2^{\uparrow}}{\sigma_F^{\uparrow}} + \frac{G_2^{\downarrow}}{\sigma_F^{\downarrow}}\right) - \frac{G_2}{e}(a_1 e^{-L/\lambda_N} + a_2)\right] \tag{4.27}$$

The continuity of charge current at interface 1 gives:

$$I_{inj} = G_1 V_1 + \frac{b_1 \sigma_F}{e}\left(\frac{G_1^{\uparrow}}{\sigma_F^{\uparrow}} - \frac{G_1^{\downarrow}}{\sigma_F^{\downarrow}}\right) - \frac{G_1 P_1}{e}(a_1 + a_2 e^{-L/\lambda_N}) \tag{4.28}$$

The continuity of charge current at interface 2 gives:

$$-I_{out} = G_2 V_2 + \frac{b_2 \sigma_F}{e}\left(\frac{G_2^{\uparrow}}{\sigma_F^{\uparrow}} - \frac{G_2^{\downarrow}}{\sigma_F^{\downarrow}}\right) - \frac{G_2 P_2}{e}(a_1 e^{-L/\lambda_N} + a_2) \tag{4.29}$$

Define the following quantity: $R_N = \frac{\lambda_N}{\sigma_N w_N}, R_F = \frac{\lambda_F}{\sigma_F A_J}$, which are the spin resistivity of channel N and FM, respectively. The above six equations can be rewritten in the following form:

$$I_{inj} = \frac{V_1}{R_1} + \left(\frac{1+P_1}{1+P_F} - \frac{1-P_1}{1-P_F}\right)\frac{b_1}{eR_1} - \frac{P_1}{eR_1}\left(a_1 + a_2 e^{-L\lambda_N}\right) \tag{4.30}$$

$$-I_{out} = \frac{V_2}{R_2} + \left(\frac{1+P_2}{1+P_F} - \frac{1-P_2}{1-P_F}\right)\frac{b_2}{eR_2} - \frac{P_2}{eR_2}\left(a_1 e^{-L\lambda_N} + a_2\right) \tag{4.31}$$

$$b_1 = \frac{1}{2}P_F e R_F I_{inj} - \frac{R_F a_1}{R_G} \tag{4.32}$$

$$b_2 = -\frac{1}{2}P_F e R_F I_{out} - \frac{R_F a_2}{R_G} \tag{4.33}$$

$$\frac{2a_1R_1}{eR_N} = P_1V_1 + \left(\frac{1+P_1}{1+P_F} + \frac{1-P_1}{1-P_F}\right)\frac{b_1}{e} - \frac{1}{e}\left(a_1 + a_2 e^{-L/\lambda_N}\right) \tag{4.34}$$

$$\frac{2a_2R_2}{eR_N} = P_2V_2 + \left(\frac{1+P_2}{1+P_F} + \frac{1-P_2}{1-P_F}\right)\frac{b_2}{e} - \frac{1}{e}\left(a_1 e^{-L/\lambda_N} + a_2\right) \tag{4.35}$$

Plus Ohm's law for the whole detection loop:

$$V_2 = (R_{sense} + R_2 + R_{right})I_{out} \tag{4.36}$$

where R_{right} is the resistance of channel N that is on the right of contact 2. This part carry electrical current I_{out}, so it is counted in the Ohm's law. Based on the seven equations, one can solve all the seven unknows $(a_1, a_2, b_1, b_2, V_1, V_2, I_{out})$. For the case of antiparallel configuration, in the equations related to F2, change $\sigma_F^{\uparrow} \to \sigma_F^{\downarrow}, \sigma_F^{\downarrow} \to \sigma_F^{\uparrow}$, One can solve for $\Delta I_{out} = I_{out}^{P} - I_{out}^{AP}$ and $\Delta V_{sense} = V_{sense}^{P} - V_{sense}^{AP}$:

$$\Delta I_{out} = \frac{\Delta V_{NL}}{(R^* + R_{right} + R_{sense})} \tag{4.37}$$

$$\Delta V_{sense} = \frac{\Delta V_{NL} R_{sense}}{(R^* + R_{right} + R_{sense})} \tag{4.38}$$

where

$$\Delta V_{NL} = 4I_{inj}R_N e^{-\frac{L}{\lambda_N}} \prod_{i=1}^{2}\left(\frac{\frac{P_iR_i}{R_N}}{1-P_i^2} + \frac{\frac{P_FR_F}{R_N}}{1-P_F^2}\right) \times \left[\prod_{i=1}^{2}\left(1 + \frac{\frac{2R_F}{R_N}}{1-P_F^2} + \frac{\frac{2R_i}{R_N}}{1-P_i^2}\right) - e^{-\frac{2L}{\lambda_N}}\right]^{-1} \tag{4.39}$$

$$R^* = \frac{R_2}{1-P_{J2}^2} + \frac{P_F^2 R_F}{1-P_F^2} - \left[2R_N\left(1 + \frac{2R_F/R_N}{1-P_F^2} + \frac{2R_1/R_N}{1-P_1^2}\right)\left(\frac{P_FR_F/R_N}{1-P_F^2} + \frac{P_2R_2/R_N}{1-P_2^2}\right)^2\right] \times \left[\prod_{i=1}^{2}\left(1 + \frac{2R_F/R_N}{1-P_F^2} + \frac{2R_i/R_N}{1-P_i^2}\right) - e^{-2L/\lambda_N}\right]^{-1} \tag{4.40}$$

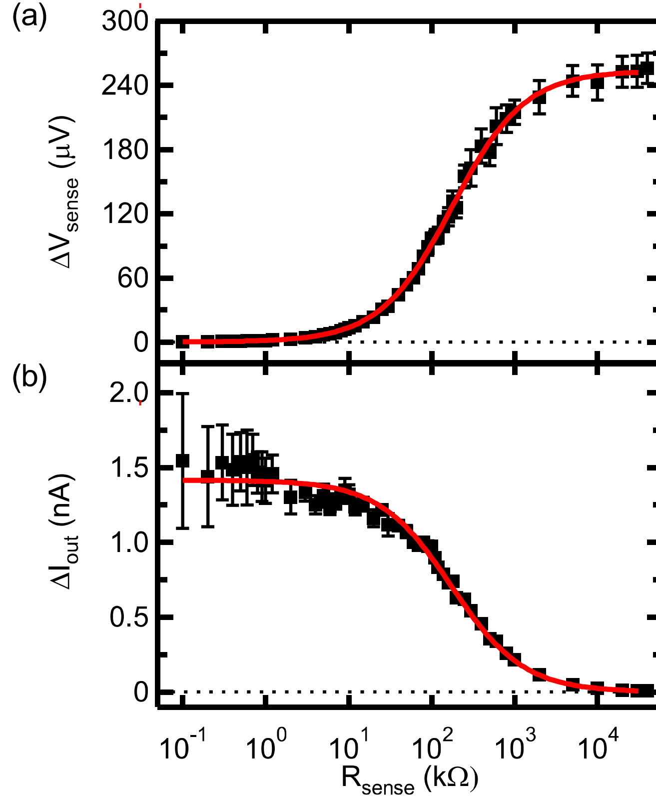

Figure 4.5: Model fit to the data. **(a)** Red curve is fit to data using Eqs. 4.38. **(b)** Red curve is fit to data using Eqs. 4.37.

In the limit of $R_{sense} \to +\infty$, the measured voltage signal $\Delta V_{sense} \to \Delta V_{NL}$ (Eqs. 4.39) which is the normal nonlocal voltage equation derived by Takahashi and Maekawa[44]. Otherwise, $\Delta V_{sense} < \Delta V_{NL}$.

Let's analyse the data in Fig. 4.3 using the above equations. Graphene is the non-mangetic spin transport channel N. For this sampe, w_N = 1.3 μm, w_F = 50 nm[60], L = 3 μm, σ_N = 0.94 mS, $\rho_F = \sigma_F^{-1} = 6 \times 10^{-8}\ \Omega \cdot m$, $\lambda_F = 0.06\ \mu m$[206], $A_J \sim 0.065\ \mu m^2$ [60, 165], $\lambda_N \sim 2\ \mu m$. In the Fig.4.1, spin injector is E_2 and spin detector is E_3. So in this case, injector contact resistance R_2 = 15 $k\Omega$, detector contact resistance R_3 = 118 $k\Omega$. Since $R_3 \gg R_N$, we are in the tunneling limit, thus $\Delta V_{NL} = I_{inj} R_N P_{J2} P_{J3} e^{-L/\lambda_N}$ and $R^* = R_3$. The data in Fig. 4.3 **(a)** and 4.3 **(b)** are fitted using Eqs. 4.37 and Eqs. 4.38 with ΔV_{NL} and the effective series resistance $R^* + R_{right}$ as the two fitting parameters. For this device, R_{right} includes the graphene resistance

between electrodes E_3 and E_4, the contact resistance of E_4, plus any wire resistance (usually much smaller than contact resistance). The best fit is shown by the red curves in Fig. 4.5, which agree well with the data. The best fit parameters are ΔV_{NL} = 249 μV and $R^* + R_{right}$ = 175 kΩ. The latter is similar to the measured 2-probe resistance across E_3 and E_4, which is $\sim$117 $k\Omega$. The discrepancy is possibly due to the fact that the resistance measurement was performed at a current bias of 1 μA, while I_{out} is on the order of 1 nA. From the fitting parameters, we can calculate the corresponding current-based spin signal as $\Delta I_{NL} = \Delta I_{sense}(R_{sense} \to 0)$ = 249 μV/175 $k\Omega = 1.42$ nA. The agreement between the data and fitting curves shows that the drift-diffusion model provides a reasonable description of our experimental results.

4.4 Device Optimization

For the logic operation the output current signal prefers to be larger. Based on the Eqs. 4.37, simulated is performed using the above device parameters. Let's go back and use index 1 for injector and index 2 for detector. R_1, R_2, P_1, P_2, R_{right} are treated as variable parameters. The maximum ΔI_{out} (when $R_{sense} = 0$) is denoted as ΔI_{NL}. The simulated results for ΔI_{NL} at different device parameters is shown in Fig. 4.6.

In **(a)**, R_1 is set to 200 Ω (transparent contact)[148]. Interfacial polarization P_1 = 0.01. R_{right} = 4.9 $k\Omega$. Let R_2 varies from 20 Ω to 3 MΩ. Plot ΔI_{NL} as a function of R_2 for different interfacial polarization P_2 (0.01, 0.05, 0.10, 0.20, 0.30). As expected, when P_2 is bigger, there is more spin current flows into the FM, causing a bigger detected current. Interestingly, there is an optimum current signal when R_2 is close to the spin resistivity of graphene $R_N = \frac{\lambda_N}{\sigma_N w_N}$. This can be understood as follows. When R_2 is very small compared to R_N, the spin detection efficiency is small, the spin accumulation in the F2 is small, causing a small current signal. When R_2 is very large compared to R_N, the detected spins saturate. The nonlocal voltage saturates, but the

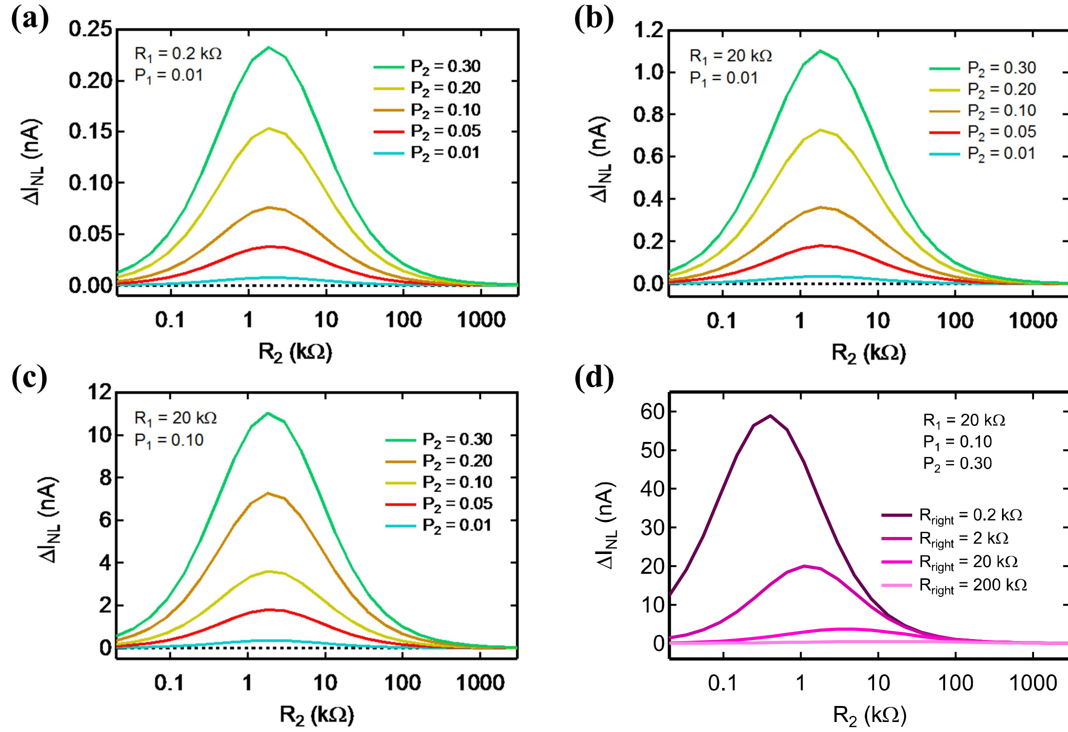

Figure 4.6: Simulated current signal ΔI_{NL} as a function of device parameters (R_1, R_2, P_1, P_2). **(a)** ΔI_{NL} as a function of R_2 for P_2. R_1 is a typical transparent contact with low spin injection efficiency (P_1). **(b)** ΔI_{NL} as a function of R_2 for P_2. R_1 is a typical tunneling contact with low spin injection efficiency (P_1). **(c)** ΔI_{NL} as a function of R_2 for P_2. R_1 is a typical tunneling contact with high spin injection efficiency (P_1). **(d)** ΔI_{NL} as a function of R_2 for R_{right}. R_1 is a typical tunneling contact.

current is small because the big resistance in the detection loop. This provide us a routine to improve the current.

In **(b)**, change R_1 to 20 $k\Omega$ (tunneling contact) and $P_1 = 0.01$. Plot ΔI_{NL} as a function of R_2 for different interfacial polarization P_2. The overall trend is the same with **(a)**, but the current is about 4 times as in **(a)**.

In **(c)**, set R_1 to 20 $k\Omega$ and $P_1 = 0.10$ (typical for tunneling contact). The overall trend for ΔI_{NL} is the same with **(a)**. Since P_2 is 10 times larger than P_{J2} in **(b)**, the amplitude of current is also 10 times bigger.

In **(d)**, set $R_1 = 20\ k\Omega$, $P_1 = 0.10$, $P_2 = 0.30$. Plot ΔI_{NL} as a function of R_2 for different R_{right} (200 Ω, 2 $k\Omega$, 20 $k\Omega$, 200 $k\Omega$). Overall, the smaller R_{right} gives bigger current, simply by

reducing the resistance in the detection loop but not changing the spin detection efficiency (may affect spin distribution when dimension is very small).

4.5 Conclusion

We have successfully demonstrated the current-based detection of nonlocal spin transport in graphene spin valves, which is critical for spintronic devices that are based on current readout. By adding a variable sensing resistor in parallel to the conventional nonlocal voltage detector, we systematically tune between voltage-based detection and current-based detection. The observed behavior is well described by a one-dimensional drift-diffusion model. We also point out the optimum device parameters to obtain the maximum output current. These results take an important step toward realizing spin-based logic in graphene.

Chapter 5

Bias Dependence of Spin Injection in Graphene

This chapter will discuss experimental observation of bias dependence of spin injection into graphene in lateral spin valve geometry. Possible reasons are discussed.

5.1 Introduction

To achieve efficient electrical spin injection from ferromagnet to nonmagnet, which is the essential ingredient in spintronics research, it is important to understand how the bias voltage (or current) affects the spin injection process. Experimentally bias dependence has been extensively studied in vertical structures[207, 208, 209, 210, 211, 212, 213, 18, 19, 214, 215, 216], lateral structures[217, 218, 49, 219, 220, 221, 222, 223], and especially in lateral graphene spin valves[202, 146, 145, 224]. Spin injection efficiency or spin polarization has been found to be dramatically dependent on the applied voltage bias across ferromagnetic injector and contacting nonmagnetic spin channel. Theoretical explanations have been proposed to describe the observations, including FM density of state effect[213], localized and delocalized states[183],

resonant surface states[225], detailed properties of interface and channel[226], shape of the potential barrier[227] and electrical drift effect[228, 229]. However, there is lack of study of bias dependence across reliable tunnel barriers in graphene spin valves which is crucial to understand the properties of spin injection and relaxation.

In the later of the chapter, bias dependence of spin injection across Co/MgO tunnel barrier contacts is reported in graphene spin valve. Nonlocal spin signal is found to strongly dependent on the bias current applied across the injecting contact.

5.2 Experimental Methods

Graphene spin valve device is fabricated using the process described in Chapter 3.The final device structure is shown in Fig. 5.1(**a**). Single layer graphene is exfoliated onto 300 nm SiO_2 substrate. Ti/Au (5/60 nm) electrodes are defined at the two ends of graphene flake. Ti-seeded MgO tunnel barrier is deposited in UHV chamber, followed by 80 nm Co deposition on top of MgO. For device A shown in this chapter, MgO thickness is 0.9 nm. Electrical current I_{inj} is injected through Co contact E_2 to graphene, and return to Ti/Au contact E_1. This electrical current is AC modulated DC current, $I_{inj} = I_{AC} + I_{DC}$. I_{AC} has rms value of 1 μA. I_{DC} goes from 0 to 10 μA. The positive bias current direction is defined as current going from E_2 to graphene to E_1. Nonlocal voltage is detected between E_3 and E_4 using a lock-in amplifier. I_{inj} generates a spin accumulation underneath E_3 that is AC modulated. Only this AC modulation part of spin accumulation can be detected by lock-in. In our case, I_{AC} is normally smaller than I_{DC}. Measured nonlocal voltage signal $V_{NL,AC}$ is probing variation of spin accumulation over a small energy window.

It may be better to understand in this way. I_{AC} generates an AC modulated nonlocal voltage $V_{NL,AC}$. I_{DC} generates a constant DC nonlocal voltage $V_{NL,DC}$. When injecting both AC

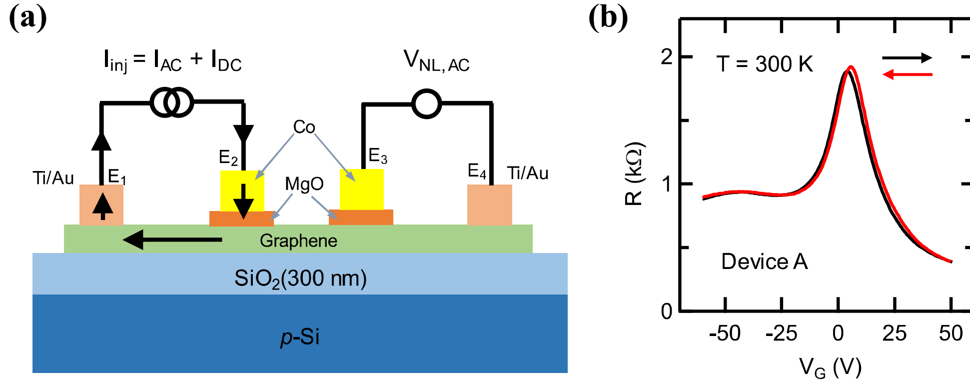

Figure 5.1: Schematic diagram of the device and nonlocal spin transport measurement. **(a)** Structure of the graphene spin valve device. Electrical current $I_{inj} = I_{AC} + I_{DC}$ injects spin through Co electrode E_1. Spin is detected in Co electrode E_2 using a lock-in amplifier. Only AC part of the nonlocal voltage is detected by lock-in. Positive bias current is defined as current going from Co to graphene, that is electrodes going from graphene to Co. **(b)** Measured graphene resistance as a function of back gate voltage at 300 K for Device A. Black curve is sweeping V_G from -60 V to +50 V. Red curve is sweeping V_G from +50 V to -60 V. Small hysteresis is observed for the sample.

and DC current, $I_{inj} = I_{AC} + I_{DC}$, there are both AC and DC response in the nonlocal voltage $V_{NL} = V_{NL,AC} + V_{NL,DC}$. Lock-in can only pick up $V_{NL,AC}$. Measured nonlocal resistance in this case is defined as $R_{NL,AC} = V_{NL,AC}/I_{AC}$.

5.3 Bias Dependence of Spin injection

Co/MgO/Graphene contact is firstly characterized using a three probe measurement. $I_{inj} = I_{AC} + I_{DC}$ is applied between E_2 and E_1, AC voltage V_{AC} is measured between E_2 and E_3 using lock-in amplifier. Contact resistance of E_2 is measured as $R_C = V_{AC}/I_{AC}$. Fig. 5.2(**a**) shows the measured contact resistance as a function of bias current for contact E_2 in Device A. High contact resistance and nonlinear behavior is observed, indicating this is a tunnel barrier contact. Also, the bias voltage across the MgO barrier is plot as a function of bias current. It is pointed out that the derivative of V_{bias} vs. I_{DC} curve is the measured contact resistance R_C in (**a**). At bias current I_{DC} = 10 μA, the voltage drop across the MgO barrier can be 0.44 V. This corresponds

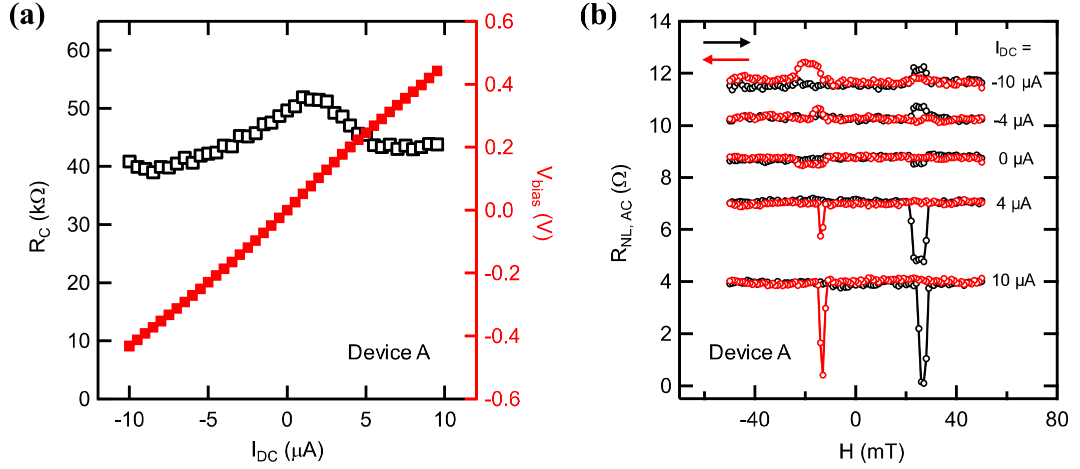

Figure 5.2: Spin transport measurement at different bias. **(a)** Black open squares are measured contact resistance R_C of E_2 in Device A as a function of bias current. Red solid squares is the corresponding bias voltage across MgO tunnel barrier at each bias current. **(b)** Nonlocal resistance $R_{NL,AC}$ as a function of magnetic field that is along the axis of Co electrodes. The bias current is (from top to bottom) -10, -4, 0, 4 and 10 μA. The curves are shifted vertically for clarity. Gate voltage is 0.

0.44 eV Fermi level shifting compared to zero bias situation.

Next, nonlocal spin transport in investigated. Fig. 5.2**(b)** shows the measured nonlocal resistance $R_{NL,AC} = V_{NL,AC}/I_{AC}$ as a function of swept in-plane magnetic field at different bias. The spin signal $\Delta R_{NL,AC}$ is defined as $\Delta R_{NL,AC} = R^{P}_{NL,AC} - R^{AP}_{NL,AC}$ and indicates how big the spin accumulation varies at particular bias current. It can be seem that $\Delta R_{NL,AC}$ is strongly dependent on the applied bias. At $I_{DC} = -10$ μA, $\Delta R_{NL,AC}$ is negative, meaning increasing the injected current causes the resulted spin accumulation to be smaller. This strong modulation is distinct from trivial behavior that spin accumulation scales linear with injected current. Similar nonlinear behavior in bias dependence has been seem in transparent contacts and other type of tunnel barriers (Al_2O_3 barrier(unpublished)).

Fig. 5.3**(a)** is a detailed measurement of $\Delta R_{NL,AC}$ at different bias current and gate voltages for Device A. For this device, no significant gate voltage dependence is observed. At positive bias, $\Delta R_{NL,AC}$ increases with increasing I_{DC}, and tends to saturate at high bias. At

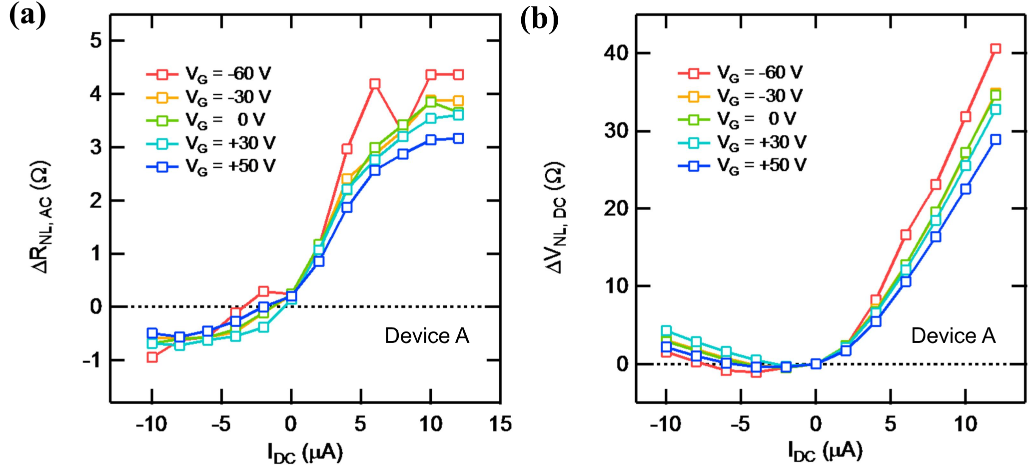

Figure 5.3: Nonlocal signal at different bias current and gate voltages for Device A. (**a**) $\Delta R_{NL,AC}$ as a function of bias current I_{DC} at different gate voltages, -60, -30, 0, +30 and 50 V. (**b**) DC response $\Delta V_{NL,DC}$ as a function of bias current I_{DC}. $\Delta V_{NL,DC}$ is obtained by integrating $\Delta R_{NL,AC}$ over I_{DC}.

negative bias, $\Delta R_{NL,AC}$ quickly becomes and remains negative. This behavior is reproducible at all gate voltages. Fig. 5.3(**b**) is plotting the integrated $\Delta V_{NL,DC}$ as a function of I_{DC}. $\Delta V_{NL,DC}$ can be interpreted as the overall detected spin accumulation at injection current I_{DC}. $\Delta V_{NL,DC}$ is strongly nonlinear.This could be due to asymmetry of spin injection and extraction, or density of state change in Co at Fermi level or something else.

Similar behavior is seem in Device B. For this device, MgO barrier is 1.2 nm thick. Contact resistance for E_2 is 44 - 86 kΩ and shows typical tunnel barrier behavior. Contact resistance for E_3 is 23 - 33 kΩ. Fig. 5.4 shows measured $\Delta R_{NL,AC}$ and $\Delta V_{NL,DC}$ as a function of DC bias current. Device B displays quantitatively the similar behavior as Device A.

5.4 Possible Explanation

The observed behavior of $\Delta R_{NL,AC}$ can not be explained by the simple 1D drift-diffusion equation discussed in Chapter 4. Takahashi-Maekawa equation[44](Eqs. 4.39) pre-

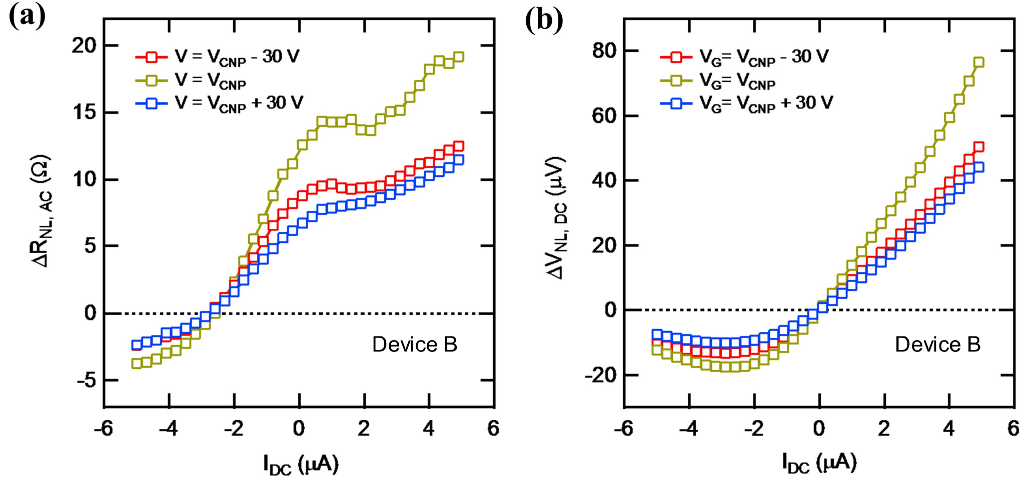

Figure 5.4: Nonlocal signal at different bias current and gate voltages for Device B. **(a)** $\Delta R_{NL,AC}$ as a function of bias current I_{DC} at three gate voltages: $V_{CNP}-30$ V, V_{CNP} and $V_{CNP}+30$ V. $V_{CNP}=-2$ V. **(b)** DC response $\Delta V_{NL,DC}$ as a function of bias current I_{DC}. $\Delta V_{NL,DC}$ is obtained by integrating $\Delta R_{NL,AC}$ over I_{DC}.

dicts no bias dependence. Spin accumulation is linearly dependent on the injection current. The possible factors that can affect the observed behavior are the following:

1. Electrical field effect. Inside graphene, there is an electrical field when there is electrical current passing through, due to finite resistance of graphene. It is given by $E_G = I\rho_G/w_G$, where I is current, ρ_G is graphene resistivity, w_G is the graphene width. Taking the typical value of our device, $\rho_G \sim 5$ kΩ at Dirac point, $w_G = 2$ μm, I = 10 μA, E_G is estimated to be $\sim 2.5\times10^4$ V/m or less (away from Dirac point). This effect needs to be further explored.

2. Cobalt DOS effect. In the two devices discussed above, the change of bias voltage across the MgO barrier is 0.3 - 0.4 eV. This could have significant effect on the Fermi level. Spin polarization in cobalt is strongly dependent on the location of Fermi level[230, 231]. Such big change in Co Fermi level could results significant change in spin polarization, causing a significant change in $\Delta V_{NL,DC}$.

3. Spin injection and extraction. Positive and negative bias correspond to spin extraction and injection situation of electrons. When it is in the spin injection process, the spin

polarization of tunneling electrons is determined by the Fermi level spin polarization of cobalt. In the spin extraction process, electrons coming from graphene could tunnel to hot electron states that could have significant different spin polarization.

Further study needs to be done to investigate the origin of the observed bias dependence. This includes study bias dependence in another FM (Fe, Py, Ni, etc.) and different barrier (Al_2O_3, SrO, hBN, etc.).

5.5 Conclusion

In this chapter, a strong bias dependence of spin injection in graphene spin valve is examined. DC bias current is modulated by an AC current as spin injection current across MgO tunnel barrier. By detecting AC response of spin accumulation in nonlocal geometry, a strong bias-dependent spin injection process is observed. There is clearly a nonlinear behavior in the electrically injected current and generated spin accumulation. This behavior can not be explained by simple drift-diffusion equation. Possible causes are proposed but further detailed analyse is still needed.

Chapter 6

XOR Logic Operation in Graphene

In this chapter, the demonstration of XOR logic operation in graphene spin valve devices is discussed. This result is essential as a proof-of-principle demonstration of previously mentioned magnetic logic gate (MLG) devices in Chapter 2.

6.1 Introduction

The five terminal MLG proposed in Chapter 2 can be decomposed to two parts, each part has three ferromagnetic electrodes and operates as XOR logic device. Before demonstrating the full operation of this MLG, it is crucial to do a proof of principle demonstration of XOR logic with three ferromagnetic electrodes. In this chapter, starting with traditional graphene spin valve devices, step by step demonstration of XOR logic operation is demonstrated.

6.2 Logic Operation

Graphene spin valve devices were fabricated as described in Chapter 3. Ti/Au contacts are fabricated on the two ends of exfoliated graphene flake to be used as reference electrodes. Multiple Co/MgO tunnel barrier contacts are fabricated in between with spacing 1 - 3 μm.

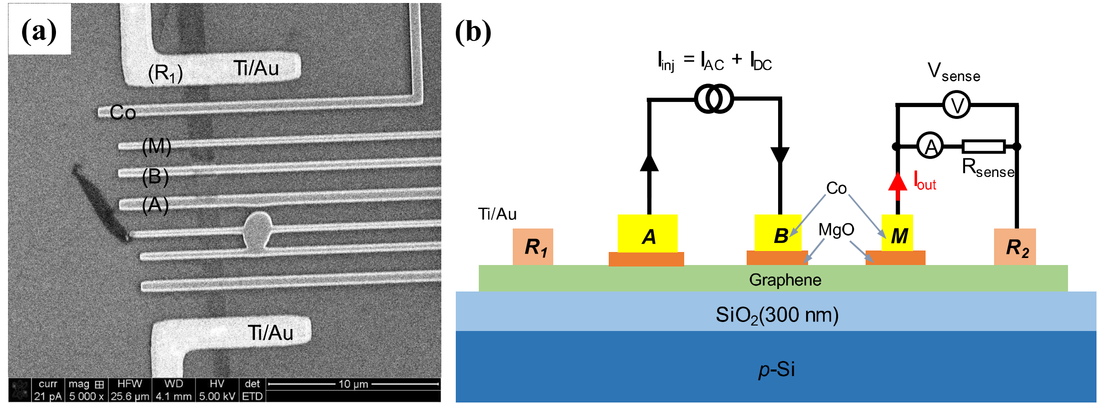

Figure 6.1: Device structure and SEM image. **(a)** SEM image of a typical graphene spin valve device with two Ti/Au contacts at the two ends, and multiple Co contacts in between. **(b)** Schematic of device structure. The two Ti/Au contacts and three ferromagnetic cobalt contacts are used in measurement.

Fig. 6.1**(a)** shows SEM image of one of the fabricated device. Ti/Au electrodes are 1 μm wide and Co electrodes are 200 - 500 nm wide. Single layer graphene can be identified as the vertical dark strip in the middle. There are two electrodes shorted by an unexpected exposure and Co deposition, which are not used in the experiments. Fig. 6.1**(b)** shows the diagram of a typical measurement on the device. Three Co electrodes (A, B and M) and one Ti/Au electrodes (R_2) are used in a logic operation. R_1 is used for charge transport characterization. Magnetization of A and B are used as logic input, and voltage (or current) signal coming out of M is used as output. The output signal is a voltage signal (V_{sense}) when $R_{sense} \to +\infty$ and is a current signal (I_{out}) when $R_{sense} \to 0$. Co electrodes A and B are made wider than M to have smaller switching field. All the measurement are done at room temperature.

Contact properties are firstly characterized before the logic operation. Fig. 6.2**(a)** shows the contact resistance measured in three probe geometry (see Chapter 3) at different bias for Device C. For this device, all the contact resistances are $\sim$ 3 - 5 kΩ, indicating possible pinhole contacts. Four probe graphene resistance is measured in Fig. 6.2**(b)**. Clear bipolar transport is observed for both graphene channels AB and BM. Graphene width w_G is 1.5 μm.

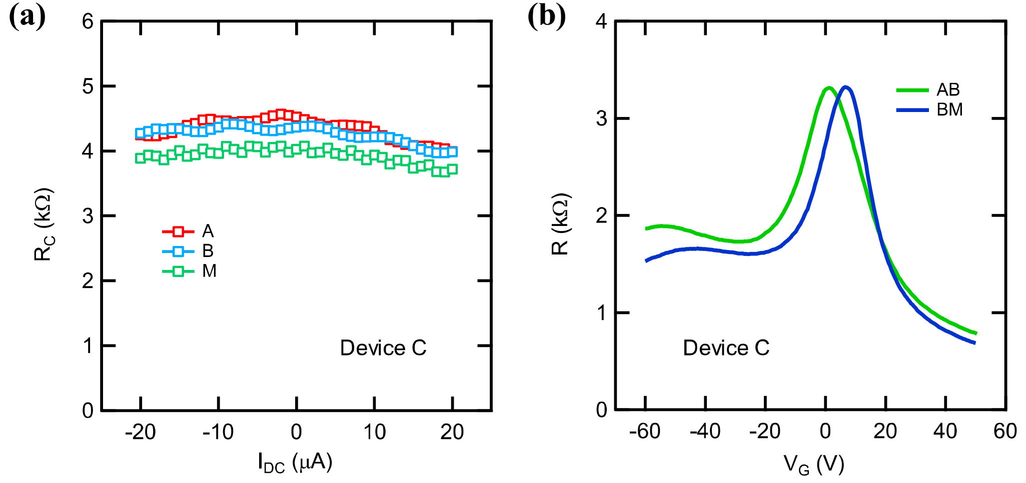

Figure 6.2: Contacts and graphene resistance. **(a)** Measured contact resistances as a function of bias I_{DC} for electrodes A, B and M for Device C. **(b)** Measured graphene resistance as a function of back gate voltage V_G for channel AB and BM. L_{AB} = 1.9 μ, L_{BM} = 1.6 μm.

Center-to-center distance between A and B is L_{AB} = 1.9 μm, and L_{BM} = 1.6 μm. The small hump at around -45 V is possibly due to contact induced doping[140], so the graphene underneath the contact can have a different Dirac point than graphene between two contacts.

Normal nonlocal spin valve measurement is done by passing electrical current through one FM to a NM (eg. from B to R_1). Nonlocal signal is detected between another FM and another NM (eg. between M and R_2). In this geometry, there is only one FM injecting spin and one FM detecting spin. So in the scan of in-plane magnetic field, only two nonlocal voltage jumps ('switchings') will be observed in one sweeping direction. This is shown in Fig. 6.3(top curve) for Device C. Nonlocal voltage is plot as a function of scanned in-plane magnetic field. Injection current is I_{inj} = 5 μA. The two switchings are corresponding to B and M. Note the asymmetry of the switching field for positive and negative direction. This is probably due to the pinned domains at the 90° bends in the Co electrodes. Because of this, it is not deterministic to say which electrode corresponds to which voltage jump without further experiments.

Next, electrical current is flowing through two FMs. This situation is shown in

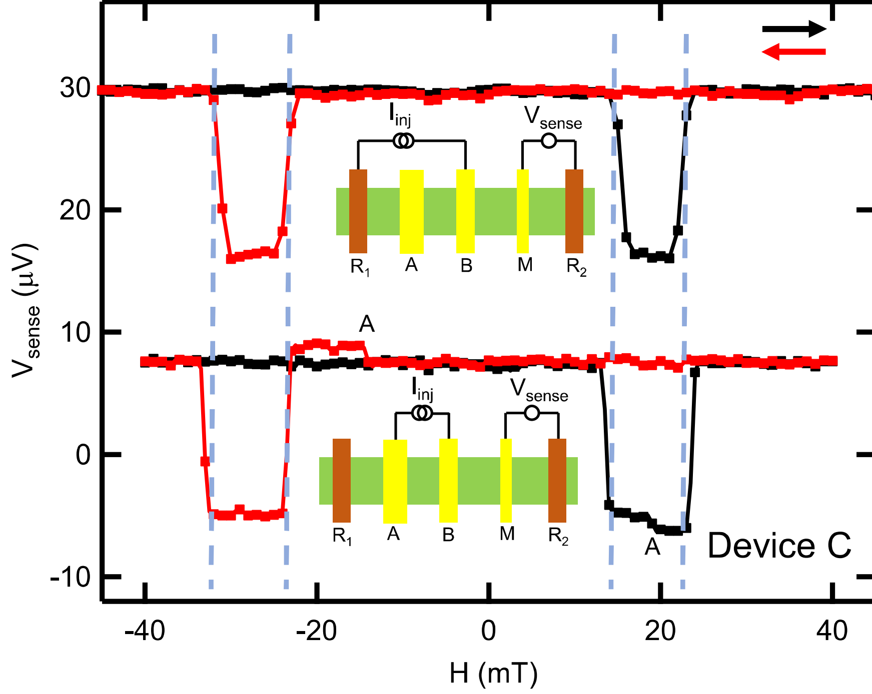

Figure 6.3: Nonlocal voltage signal for two inputs. **Top curve:** V_{sense} as a function of magnetic field for B as the spin injector and M as the spin detector. **Bottom curve:** V_{sense} as a function of magnetic field for both A and B as the spin injectors and M as the spin detector. The measured voltage change due to the switching of A is noted as 'A' for both up sweep and down sweep.

Fig. 6.3(bottom curve). I_{inj} is flowing through both B and A with opposite current flowing direction. Both A and B is going to inject (or extract) spins inside graphene channel. So in the detected voltage signal V_{sense}, there are three switchings in one direction sweep of magnetic field. Two of the switching fields match the curve on top. The extra one is coming from switching one A. Since A is further away from detector M, the generated voltage signal is smaller than B.

To perform logic operation, the output electrode M is set to be fixed. Inputs A and B are allowed to change ($\uparrow$ or $\downarrow$) by magnetic field. Fig. 6.4 shows the minor loop when both A and B are used as spin injectors. M is fixed to be pointing $\uparrow$. This is achieved by firstly applying large positive field to magnetize M to $\uparrow$. Then in the following measurement, negative magnetic field is limited to be smaller than the switching field of M. This is possible only if both A and B

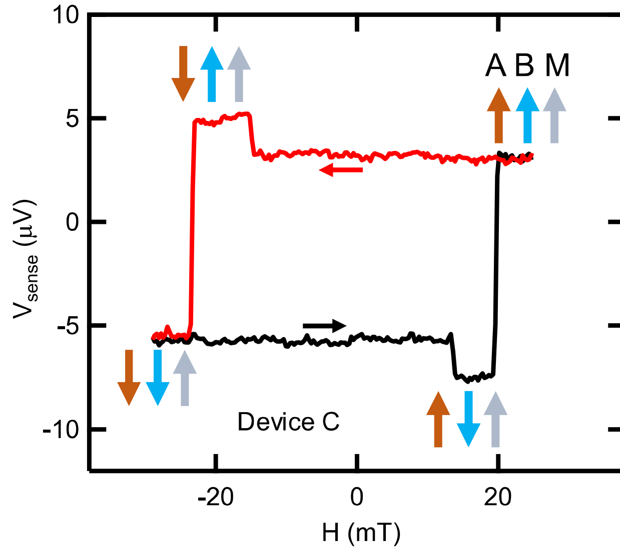

Figure 6.4: Minor loop for logic operation. In-plane magnetic field is swept from -29 mT to +25 mT (black curve) and +25 mT to -29 mT (red curve). Magnetization states of A, B and M are labeled at each voltage level. M is fixed to be $\uparrow$.

switch at lower field than M.

Magnetic field is firstly swept from -29 mT to +25 mT. The starting magnetization status for A, B and M is $\downarrow\downarrow\uparrow$. With increasing magnetic field at +13.6 mT, A switches from $\downarrow$ to $\uparrow$, causing a detected voltage drop. At field +19.6 mT, B switches from $\downarrow$ to $\uparrow$, causing a detected voltage increase. This voltage level ($\uparrow\uparrow\uparrow$ state) remains until field is swept from +25 mT to -14.9 mT when A switches from $\uparrow$ to $\downarrow$, and a higher voltage level is seem. At -23.3 mT, B switches, causing a big detected voltage drop, back to the starting voltage.

The expected behavior for the device mentioned above is XOR logic. That is, when input $A = B$ (A and B are in parallel state), the output is zero (logic '0'). When input $A \neq B$ (A and B are in antiparallel state), the output is non zero (logic '1'). For the proper logic operation, the output '1' should be significant different than '0' (well above the noise level). However, in Fig. 6.4, they are four output levels which creates two issues. One is that for parallel state inputs, the output levels are not the same for $\uparrow\uparrow$ and $\downarrow\downarrow$. The second is that for the antiparallel state, the output level are also not the same for $\uparrow\downarrow$ and $\downarrow\uparrow$. Specifically, output for parallel state

is either +3.3 μV(↑↑) or -5.7 μV(↓↓), and output for antiparallel is either +4.9 μV(↓↑) or -7.5 μV(↑↓). The difference of parallel and antiparallel is not so big. This is because of the fact that A is further away from M than B, so spin injected by A is less influential to the detected signal than spin injected by B. The way to overcome these issues is given by the next section.

6.3 Input Balancing

To overcome the issue discussed above, the output signal levels for parallel states (↑↑ and ↓↓) need to be the same. Firstly, gate voltage was found to have some effect on the relative contribution from A and B (Fig. 6.5(**a**)). For Device C, +50 V gives the smallest voltage gap between ↑↑ and ↓↓. Next, when V_G is set to +50 V, bias current was found to have a significant effect on the detected signal(Fig. 6.5(**b**)). When $I_{DC} = -35$ μA, the voltage level for ↑↑ and ↓↓ are the same. Here, positive bias current is defined as current from input B to graphene to input A. The behavior of bias dependence is in consistent with bias dependent spin injection discussed in Chapter 5. It is noticed that the nonlocal signal ΔR_{NL} gets bigger for positive bias and smaller for negative bias(Fig. 5.3). Taking the fact that A and B has different bias direction at all times, applying positive bias on A means negative bias on B. While contribution from A can be enhanced by getting more positive bias, contribution from B is depressed because of the more negative bias. Initially at I_{DC} = 0, input B has a much bigger contribution to the detected signal than input A. With increasing negative bias, the different of the voltage contribution between B and A gets smaller. Eventually at $I_{DC} = -35$ μA, contribution from A and B match up to give the same voltage level for parallel input states ($A = B$, meaning ↑↑ or ↓↓).

Bias tuning of minor loop for another Device D is shown in Fig. 6.6(**a**). Define the signal due to input B is ΔV_B, the signal due to input A is ΔV_A. A detailed plot of ΔV_A and ΔV_A as

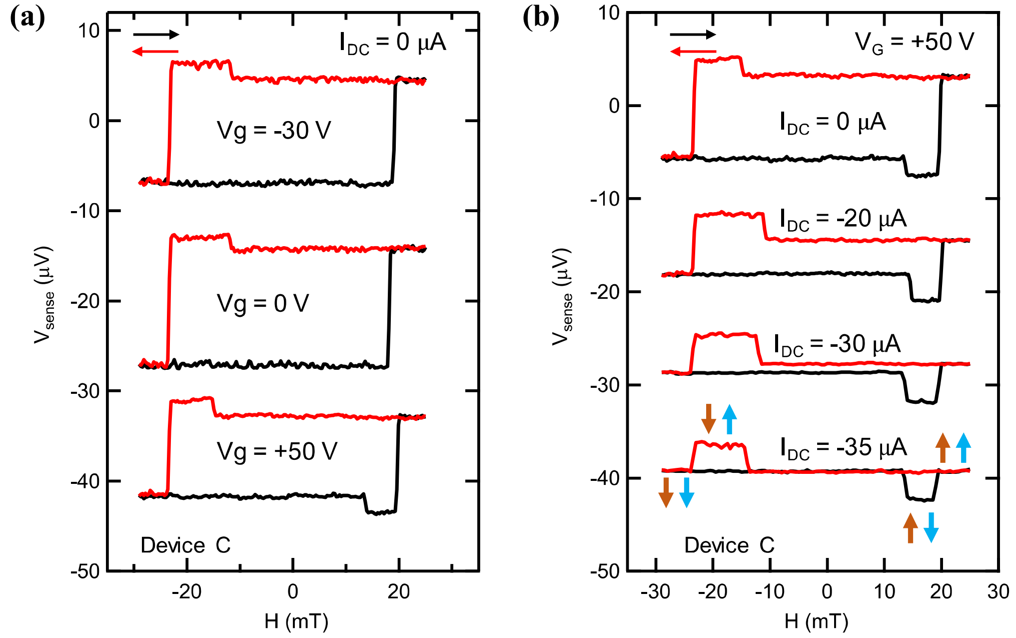

Figure 6.5: Minor loop at different gate voltages and bias current for Device C. I_{inj} = 5 μ **(a)** Minor loop of V_{sense} as a function of magnetic field at different gate voltages (-30 V, 0 V and + 50 V) for zero bias ($I_{DC} = 0$). There is offset in the curves for clarity. **(b)** Minor loop of V_{sense} as a function of magnetic field at different bias (I_{DC} = 0, -20, -30, -35 μA) for V$_G$ = + 50 V. There is offset in the curves for clarity. The input configuration (magnetization of A and B) is labeled in the bottom curve.

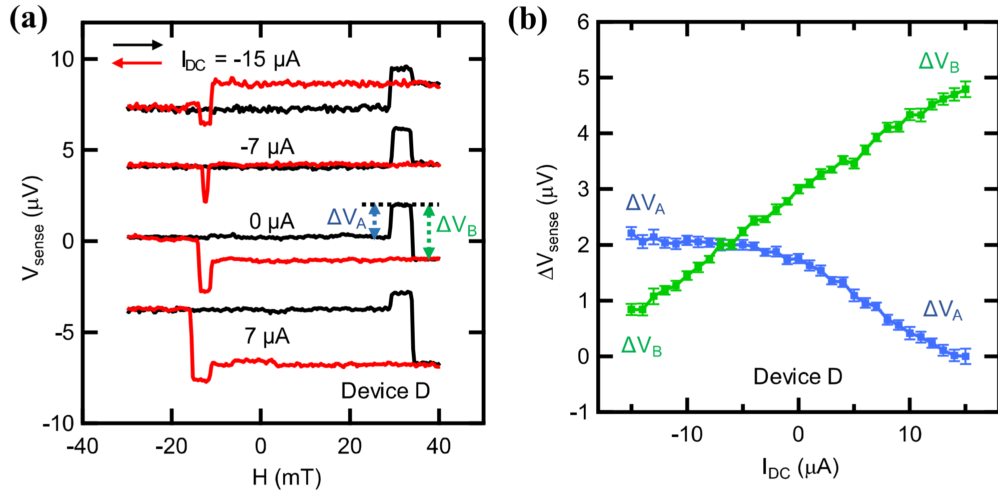

Figure 6.6: Minor loop at different bias current for Device D. I_{inj} = 1 μA. **(a)** Minor loop of V_{sense} as a function of magnetic field at different bias current (-15, -7, 0, +7 μA). There is offset in the curves for clarity. **(b)** Detailed plot of voltage signal ΔV_A and ΔV_B as a function of bias current I_{DC}.

a function of bias current I_{DC} is plot in **(b)**. In this situation, negative bias in the plot is 'positive' bias for junction A. This is the reason why ΔV_A and ΔV_B behavior the opposite way in the plot.

6.4 Voltage Offset

Ideally, the detected nonlocal voltage background is zero, meaning $V_{background} = (V_{sense}^{P} + V_{sense}^{AP})/2 = 0$. Experimentally there is always a non zero background which depends on gate voltages, bias current, AC current frequency, etc. The exact origin is unclear. So far, we have ignored this background in the detected nonlocal signal. To achieve an absolute zero output when input is in parallel state, an offset voltage source is added in the detection circuit. The diagram is shown in Fig. 6.7**(a)**. Since the injected current has AC components I_{AC}, and lock-in can only detecting AC response of spin signal, this offset voltage V_{offset} needs to be exactly the same frequency and in phase with I_{AC}. This is achieved by doing the following: using Keithley 6221 as AC and DC current source, and using external reference mode of lock-in to lock to Keithley 6221. Then set lock-in oscillator output to be in-phase with reference signal. Use this oscillator output as the V_{offset}. The resolution of V_{offset} is 1 μV which is the resolution of lock-in output. At the mean time, make sure the two ends of Keithley 6221 current output are floated to the ground. In Fig. 6.7**(a)**, electrode R_2 is taken as ground point.

Fig. 6.7**(b)** shows a series of V_{sense} taken at different V_{offset} at optimal bias condition (I_{DC} = -7 μA) for Device D. Define the signal magnitude as $\Delta V_{sense} = |V_{sense}^{AP} - V_{sense}^{P}|$. It is very clear that V_{offset} only changes the voltage level of V_{sense}, leaving V_{offset} unchanged. And the value of V_{offset} is translated to the same amount of shift of detected V_{sense}. By using V_{offset}, the output level for logic '0' output can be manually tuned to zero.

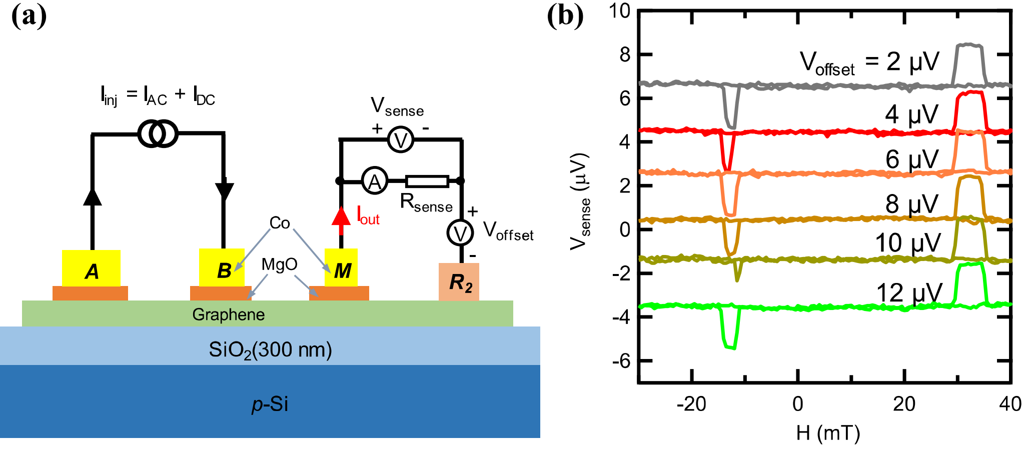

Figure 6.7: Diagram of using offset voltage source in the detection loop. **(a)** Setup for the measurement when V_{offset} is added. **(b)** V_{sense} as a function of magnetic field at different V_{offset}. V_{sense} level can be readily tuned by V_{offset}.

6.5 XOR Logic Using Current Detection

The output voltage needs to be converted to current for MLG operation. To this end, R_{sense} is systematically tuned from large to small, as discussed in Chapter 4. Fig. 6.8 shows the measured ΔV_{sense} and corresponding current ΔI_{out} as a function of R_{sense} for Device B. $\Delta I_{out} = \Delta V_{sense}/R_{sense}$. Fit ΔV_{sense} using Equation 4.38, and fit ΔI_{out} using Equation 4.37. The fitted nonlocal voltage ΔV_{NL} is $\sim$ 1.9 μV, R_{total} is $\sim$ 40 kΩ. Here $R_{total} = R^* + R_{right}$, giving by Equation 4.40. For Device B, contact resistance of M (R_M) is 33 kΩ, much larger than the graphene resistance. So $R^* \sim R_M$, $R_{total} \sim R_M + R_{right}$. Two probe resistance between M and R_2 includes R_M, R_{R_2} and graphene resistance between M and R_2. The measured value is 36 kΩ using 1 μA current, close to the fitted value. It is noticed that when $R_{sense} < R_{total}/10$, there is not much change in the measured current.

Fig. 6.9**(a)** shows the measured current output I_{out} at different input configuration. When inputs A and B are '00'(↓↓) or '11'(↑↑), I_{out} = 0. When inputs A and B are '01'(↓↑) or '10'(↑↓), $I_{out} \neq 0$. This is essentially XOR logic gate. The truth table for this logic operation is

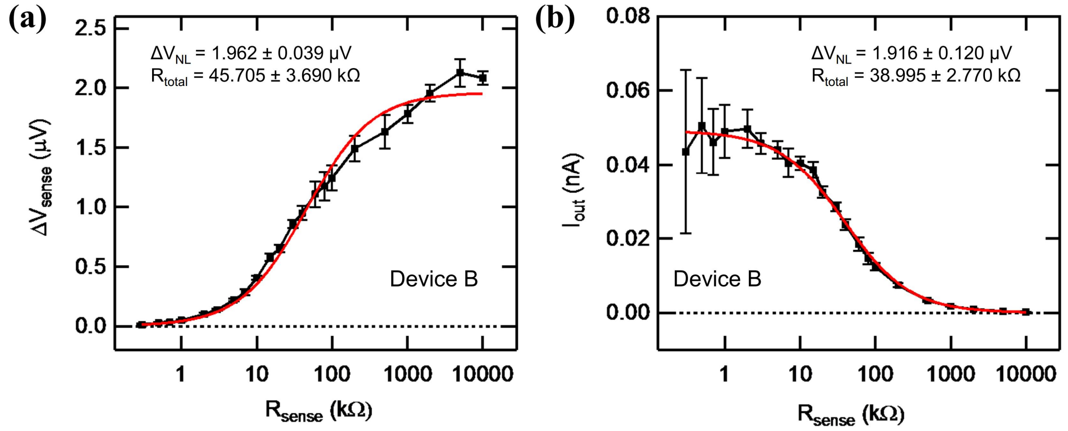

Figure 6.8: ΔV_{sense} and ΔI_{out} as a function of R_{sense}. **(a)** ΔV_{sense} as a function of R_{sense}. Red curve is the fit to Equation 4.38. **(b)** ΔI_{out} as a function of R_{sense}. Red curve is the fit to Equation 4.37.

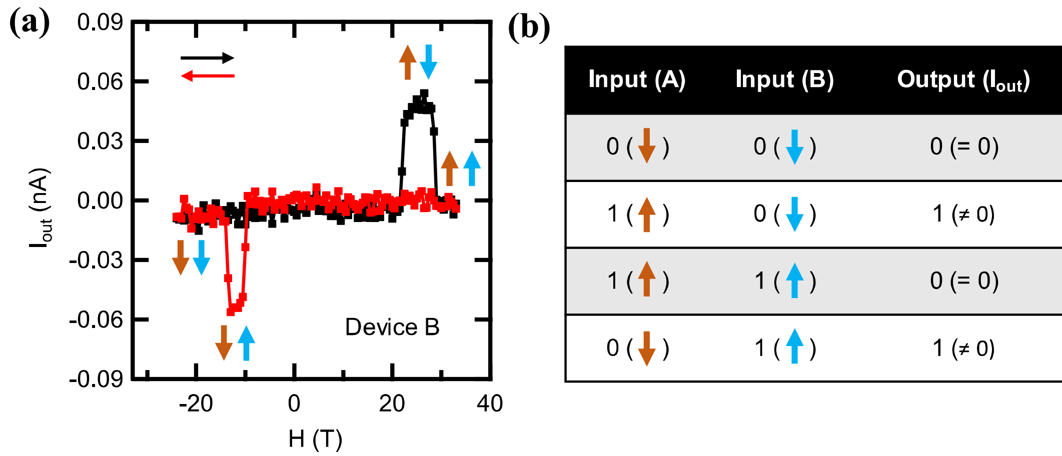

Input (A)	Input (B)	Output (I_{out})
0 (↓)	0 (↓)	0 (= 0)
1 (↑)	0 (↓)	1 (≠ 0)
1 (↑)	1 (↑)	0 (= 0)
0 (↓)	1 (↑)	1 (≠ 0)

Figure 6.9: XOR logic operation. **(a)** I_{out} at different magnetization configuration of A and B. Different magnetization is set by magnetic field. **(b)** Truth table for XOR logic operation.

in Fig. 6.9(**b**).

All the above demonstration is at room temperature (295 K). At this temperature, due to the 90° bends of Co electrodes, switching field of Co electrodes are not so well defined. This is best illustrated in Fig. 6.10 for Device B. Magnetization of M is set to ↑. Taking R_{sensen} to be 10 MΩ, measure V_{sense} as a function of magnetic field for 20 times at the optimal bias current. V_{sense} was found to be either positive or negative in the positive sweep of the magnetic field. This 'randomness' is due to the fact that switching order of A and B is not well defined. 19

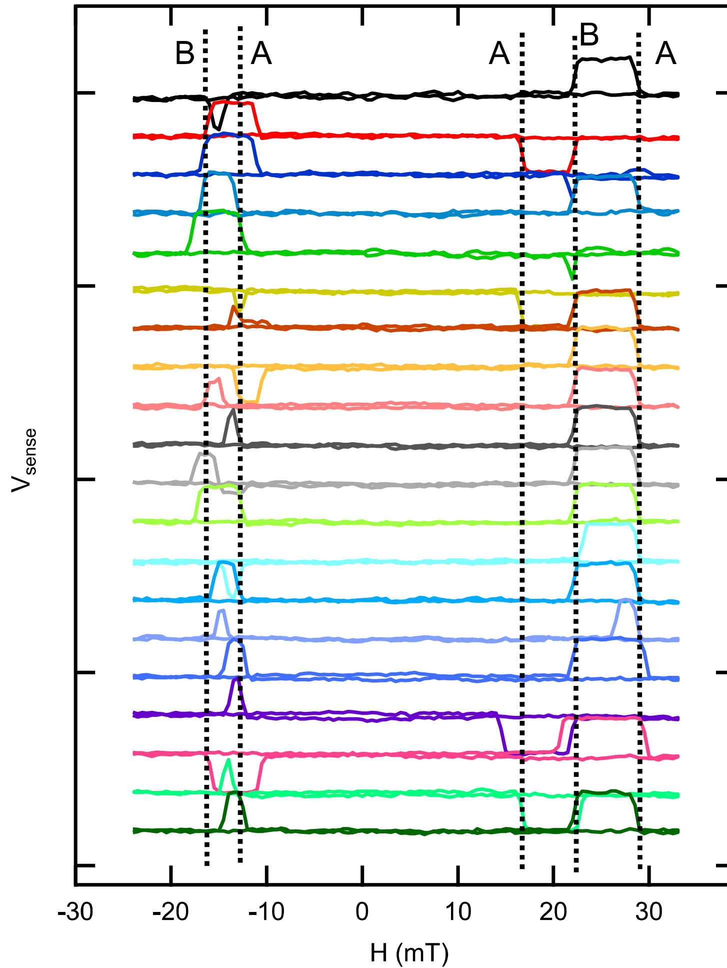

Figure 6.10: Repeated scans of V_{sense} as a function of magnetic field for Device B. The black dotted line is a guild to eyes to locate the switching field for A and B.

out of 20 times, B switches at +22 mT. 14 out of 20 times A switches at +29 mT, and 3 out of 20 times A switches at +16 mT. Note that the width of A is 360 nm and the width of B is 270 nm. However, A does not necessarily switches at smaller magnetic field than B. Even though the exact switching field for A and B is kind of random, the sign of the signal at all cases is reasonable considering the operation of XOR logic. For example, whenever A switches earlier than B, V_{sense} shows a drop. Whenever B switches earlier than A, V_{sense} shows an increase. So the sign of V_{sense} is not really random, and the reason behind it is the switching order of the two inputs. The switching order is more defined at low temperatures.

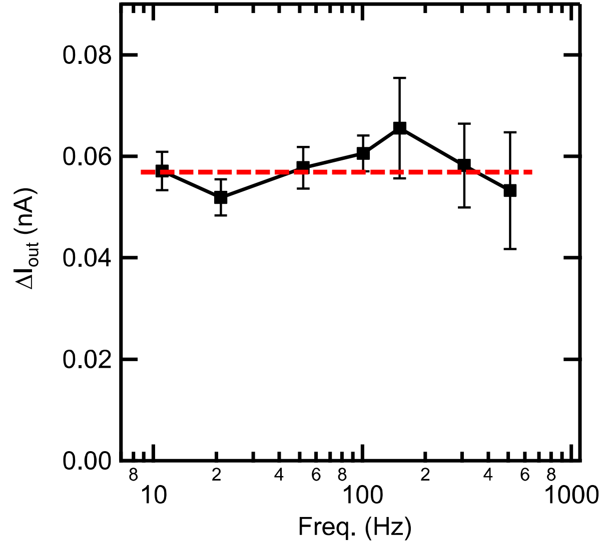

Figure 6.11: Measured ΔI_{out} as a function of AC current frequency. Red dotted line is a horizontal line to to guild the eyes. Frequency range is 11 - 509 Hz.

6.6 Frequency Dependence

For application purposes, high operating speed of the device is desired. Frequency dependence of the XOR logic operation for Device B is investigated. Frequency from 11 Hz to 509 Hz is measured. The optima bias for all the frequencies are the same. Output signal ΔI_{out} was found to be independent of frequency in the measured range. For frequency higher than 509 Hz, noise is too big to measure any signal. This big noise could come from the tunnel barrier contacts.

6.7 Confined Device

In the final logic operation, the offset voltage V_{offset} increases the complicity of the device. It was used to get rid of the background level at parallel states ('00' and '11') because the antiparallel signal is not very different from parallel signal. If the signal level in antiparallel states ('10' and '01') is much larger than parallel states, the offset voltage is not necessary. It was

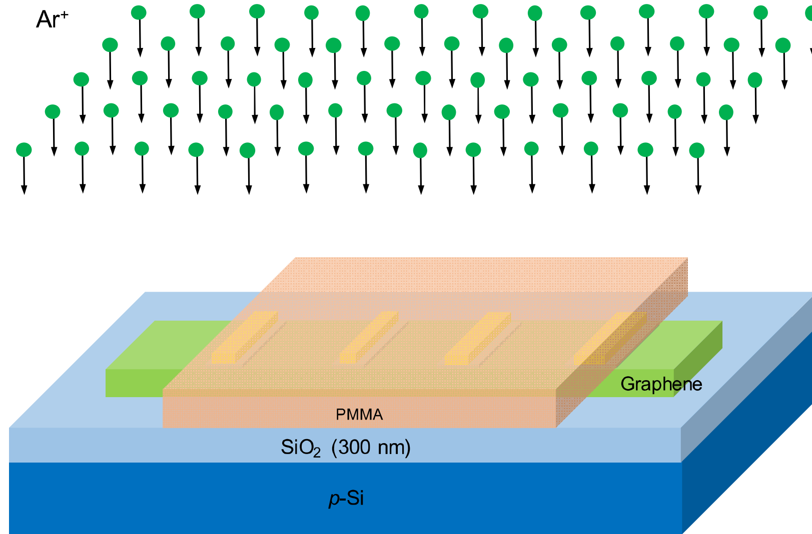

Figure 6.12: Diagram of using Ar^+ to etch away graphene. Graphene that is not covered by PMMA is exposed to energetic Ar^+.

pointed out by Dery and coworkers[203] that in a confined device, $V^{AP}/V^P \sim (\lambda_G/d)^2$, where V^{AP} and V^P are the voltage signal for antiparallel and parallel configuration, λ is graphene spin diffusion length, d is the spacing between A and B. This concept works if spins are confined in graphene channel between A and B. This requires that no graphene should be present outside the spin channel. Experimentally this confinement effect has been observed in metal system[232].

There are several ways to fabricate confined graphene device[233]. The first way is to remove graphene outside the contact after fabricating the device, using high energy ions[234]. In this thesis, Ar^+ (with energy range 0 - 3000 eV) sputtering was utilized to etch away graphene. After device fabrication, PMMA is spun coated and baked at 170 °C for 20 min. Then ebeam lithography is used to define a 'window' for sputtering, followed by development. The device is wire bonded to a sample paddle and loaded into the *insitu* chamber where both electrical measurement and Ar-sputtering can be done simultaneously. Fig. 6.12 is the diagram for the experimental setup to etch sway the graphene that is outside of the electrodes.

Fig. 6.13**(a)** shows an optical image of such device. Five Ti/Au contacts, E_1 to E_5,

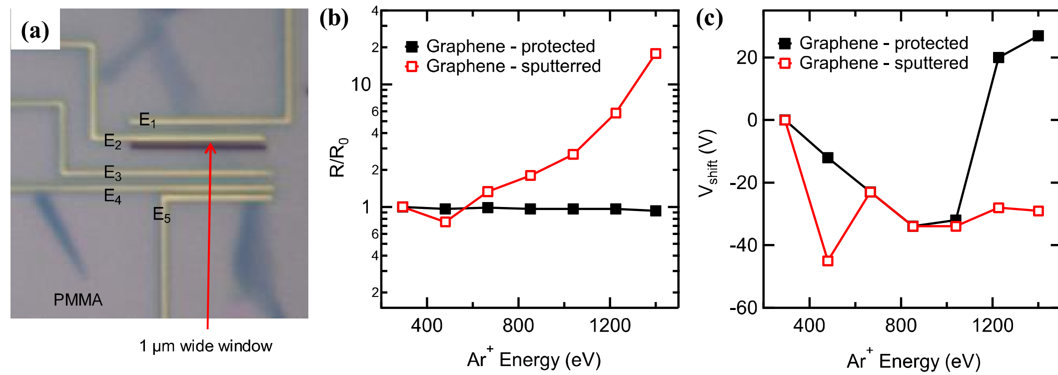

Figure 6.13: Ar^+ sputtering for different energy. Sputter time is 10 sec for each Ar^+ energy. **(a)** Optical image of the device. **(b)** Relative maximum graphene resistance after each sputtering step. **(c)** Dirac point voltage shift after each sputtering step.

were lay down on a single layer graphene. In between E_2 and E_3, there is 1 μm wide window where graphene is exposed to the outside. The rest is covered with PMMA. Energetic Ar^+ particles are accelerated with a high voltage and bombard exposed graphene. In the first experiment, sputter time was fixed to be 10 sec for each energy. Ar^+ energy was changed from 293 eV to 1400 eV. After each sputtering, gate dependent graphene resistance was measured to extract Dirac point voltage and maximum graphene resistance. Fig. 6.13(**b**) shows the maximum resistance after each sputtering step. For the graphene protected under PMMA, the resistance was not changing, showing PMMA is a good protecting layer. For graphene that was sputtered, there was an increase in resistance when Ar^+ energy is above 666 eV. A sharp increase was observed for Ar^+ energy is above 1200 eV. This increase in resistance is consistent with vacancy induced scattering in graphene[235, 234, 236]. Ar^+ was also found to introduce charge transfer in graphene, and this is shown in Fig. 6.13(**c**). There was a shift of Dirac point for both protected and sputtered graphene due to electron doping by Ar^+.

The effect of sputter time on graphene properties is investigated using Ar^+ energy of 657 eV on another device. The results is shown in Fig. 6.14. Two probe resistance was measured for graphene protected by PMMA and graphene that is sputtered by Ar^+. In Fig. 6.14(**a**), the

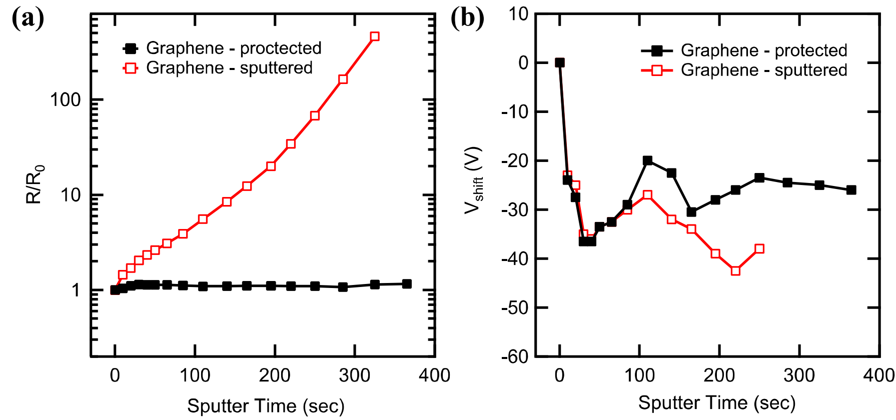

Figure 6.14: Ar^+ sputtering for different time. Ar^+ energy is 657 eV. **(a)** Relative maximum graphene resistance after each sputtering step. **(b)** Dirac point voltage shift after each sputtering step.

relative maximum graphene resistance was plot for both types of graphene. As can be seem, the resistance of graphene that was protected by the PMMA remained unaffected by Ar^+. The resistance of graphene that was exposed to Ar^+ almost increase exponentially with sputter time. After $\sim$ 300 sec, graphene resistance has increased more than 100 times compared to before sputtering. Fig. 6.14**(b)** shows the Dirac point voltage shift after sputtering. Still, electron doping due to Ar^+ is observed by. Interestingly, this electron doping seems saturated after 30 sec sputtering.

Once the optimum sputtering energy and sputter time have been figured out, next step is to fabricate a graphene spin valves device, apply the PMMA mask covering graphene that is not being exposed, and remove the outer graphene using appropriate Ar^+ energy.

The second way to fabricate confined devices is to start with small graphene pieces ($\sim$ 1 μm $\times$ 1 μm). This requires etching down the graphene size and fine alignment of ferromagnetic electrodes on top of graphene. At the time of writing this thesis, this is ongoing progress.

6.8 Conclusion

Experimental demonstration of XOR logic operation was achieved in a graphene spin valve devices. Two ferromagnetic electrodes were used as input and a current signal was used as output. The input states were changed by external magnetic field. A DC bias was used to tune the two inputs to contribute equal in the output signal. The proper logic operation was by optimizing this DC bias. This work opens the possibility for applicable spintronic logic device in graphene.

Chapter 7

Spin Transport in Large Area Graphene

This chapter will discuss the growth, transfer and etching of large area epitaxy graphene grown by chemical vapor deposition. Spin valve devices fabrication and spin transport measurement on this epitaxy graphene will also be discussed.

7.1 Introduction

Exfoliated graphene flakes can not be used for for large scale integration, although it is perfect for fundamental research where the dimension of the device is typically on the order of $\sim \mu$m. One of the goal of the proposed MLG is to be able to fabricate multiple devices on the same chip. Thus large area graphene (LAG) is important for MLG integration purposes.

LAG has been grown on various substrates, including metals (Cu[237, 80], Ni[238, 120, 119], Pt[239], Ru[240], Ir[241]), semiconductor (SiC[242, 243], Ge[244]) and insulators (MgO[245], Al_2O_3[246], SiO_2[247]), and has also been chemically reduction from graphene oxide[248]. The best epitaxy graphene so far is recently achieved in chemical vapor deposition

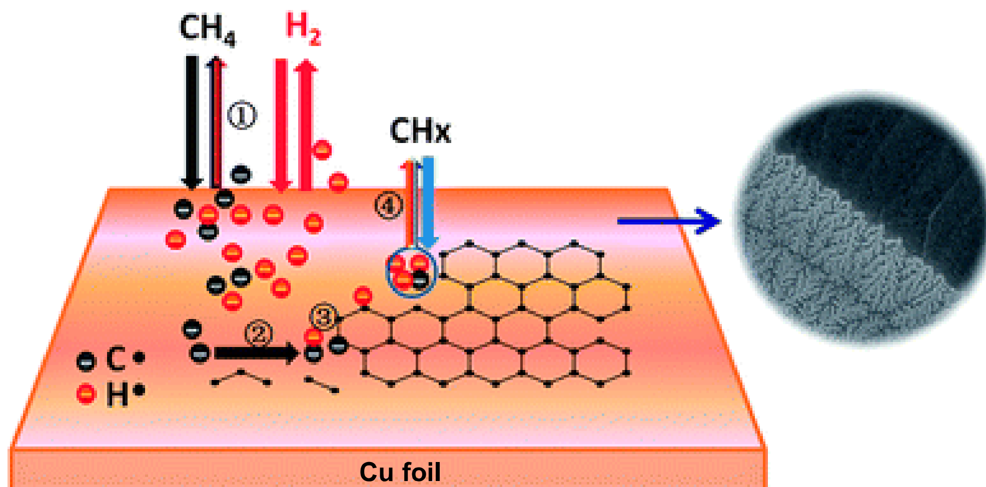

Figure 7.1: Growth mechanism for graphene on copper foil. Adapted from [249]. CH_4 is used as graphene growth precursor, providing the source of C. Copper is used as catalyst to decompose CH_4 to CH_x (x=0 - 3).

(CVD) growth on Ge(110) substrate[244] where single crystal graphene was grown on the wafer scale. However this growth is challenging due to complicated substrate preparation processes. The most common methods to grow LAG is using chemical vapor deposition (CVD) growth on Cu substrate which has given similar quality compared to exfoliated graphene[80, 125]. In this thesis CVD growth of graphene on polycrystalline Cu foil is utilized.

The growth mechanism of CVD graphene on copper substrate is shown in Fig. 7.1. Crystal direction of the Cu substrate was found to to important for monolayer graphene growth[250]. Cu(111) surface was found to promote uniform and continuous coverage. Gas precursors, methane (CH_4) and hydrogen is continuously flowing through a tube furnace where a copper foil is placed in the center of the tube furnace. When copper foil is heated to growth temperature (~1000 °C) CH_4 decomposes to CH_x (x = 0 - 3) on copper foil surface where copper atoms act as catalyst. Carbon atoms firstly starts to accumulates around active sites on copper surface (mainly defect sites). These atoms rearrange to form hexagonal carbon lattice and continue to grow bigger when more carbon atoms attach to the edge of existing graphene. H_2 in

the precursors is believed to selectively etch the edge of graphene domains during the growth process of graphene. H_2 flow rate was find to be important to achieve high quality graphene growth[251, 252, 253]. Since polycrystalline copper has different in-plane crystal orientations, graphene grown on top will also has different crystal orientations. When two domains merger together a line defect will form as grain boundary. Thus the size of the single crystal domains depends on the size of the copper domain as well as the average distance between two closest nucleation sites. To achieve larger graphene domains a low flow of methane[254] and enclosure copper foil (Cu 'bag')[123] has been shown to be helpful. The growth recipe in this thesis was adopted from from [254] and [123].

They has been several studies of graphene spin valves fabricated on epitaxy graphene, including Barbaros' group[255] and van Wees' group [130]. No significant different in spin transport was found between flake graphene and CVD grown graphene in both ^{12}C and ^{13}C form.

7.2 Growth of Large Area CVD graphene

7.2.1 Copper foil preparation

We use 25 μm thick, 99.8% (metals basis) purity copper foil from Alfa Aesar (Item #13382). A piece of $\sim 5\times8$ cm size flat copper foil is cut out first. This will be used as the copper bag. A second piece of $\sim 2\times3$ cm is cut on which desired graphene will grow. Both copper pieces are rinsed in diluted HCl solution (HCl:water = 1:3) for 1 min followed by 5 min sonication in IPA. After IPA step the pieces are taken out and blow dried with compressed nitrogen .

The big copper piece is then folded to form an enclosed bag structure. The small copper piece is inserted inside the copper bag. It is important to place some spacers in between

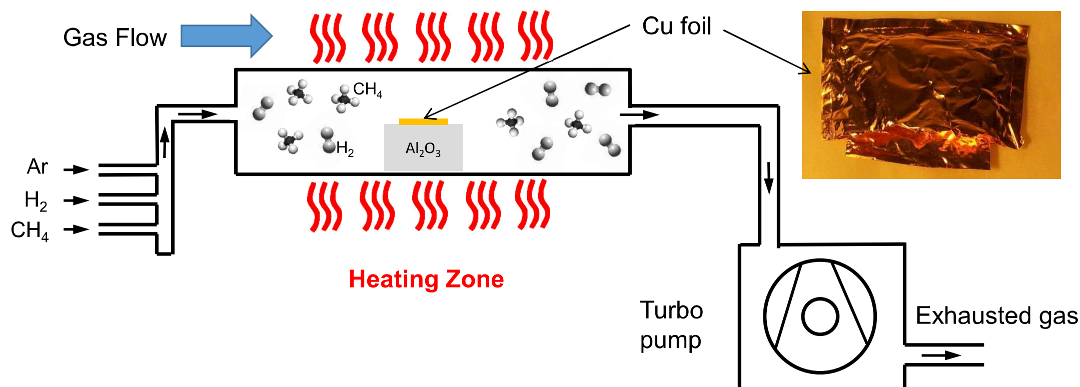

Figure 7.2: Setup for our CVD graphene growth. Gas flows from left to right. Top right is the image of copper bag we typical use for LAG growth.

the small copper piece and the bottom of the copper bag, otherwise they will fuse together. Roughly 6 piece of Al_2O_3 substrate with $1\times1\times0.1$ cm size was used as the spacer. Finally, all the edges of the copper bag are folded up and tightened with a tweezers. The picture of the bag is shown in Fig. 7.2(**top right**).

7.2.2 Growth setup

After the bag is ready, it is loaded into our tube furnace for growth. The diagram for our CVD growth setup is show in Fig. 7.2. Flows of Ar, H_2 and CH_4 are regulated by flow meters (one flow meter for each gas) and mixed up in a manifold. The mixed flow is let into a tube furnace where the a copper bag is placed in the center on top of an Al_2O_3 supporting substrate. Furnace is heated up to growth temperature (1000 °C) using resistive heating. The outlet gas is pumped out using a turbo pump operating at low speed (37 k rmp). Exhausted gas from the turbo is introduced into the building exhaust line.

The corresponding equipment used is show in Fig. 7.3. The gases are supplied with gas cylinders (from Praxair) with regulators. Each gas is then passed through a mks Mass-Flo controller where the flow of each gas can be controlled separately. Our tube furnace is from MHI (H18-40-HT) with a max temperature of $\sim$ 1750 °C. The flows for all the gases are computer

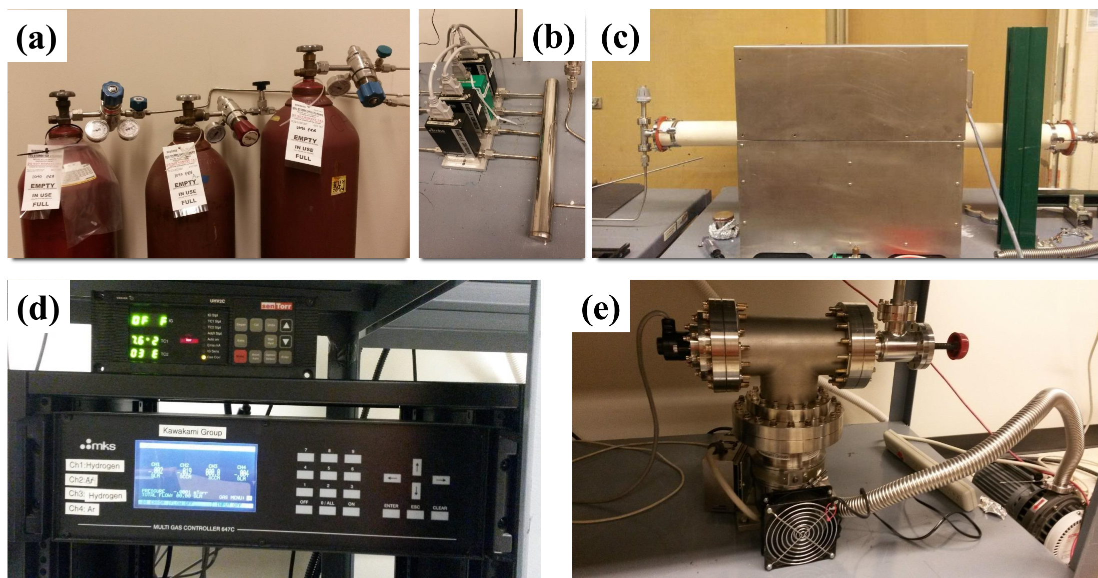

Figure 7.3: Equipments for our CVD graphene growth. **(a)** is gas cylinders for Ar, H_2 and methane. **(b)** is the four flow meters (left) and manifold (right) for controlling the flow and composition of the gas. **(c)** is the tube furnace equipped with 2.75" OD Al_2O_3 horizontal tube. **(d)** is MKS gas flow controller. **(e)** is the tubo pump with a cooling fan.

controlled through mks Multi Gas Controller 647C. The turbo pump is Varian TV301 Navigator. Back up pump is a scroll pump.

After loading the copper foil into the furnace, the furnace is pumped down to a base pressure of $\sim 1\times10^{-6}$ Torr using turbo pump at high speed (56 k rpm). After the pressure is reached the turbo is set to low speed (37 k rpm) and ion gauge is turned off. Wait 1 hour for turbo blade to slow down. When turbo is at low speed, it is ready to start graphene growth according to the recipe described in Fig. 7.4. 69 sccm of Ar gas is firstly introduced as a filling gas. Furnace is set to to warm up to 1000 °C with 12 °C/min rate while the Ar is still flowing. After reaching 1000 °C, a mixture of Ar/H_2 (69 sccm : 2 sccm) is introduced for 1 hour while temperature remains at 1000 °C. This is to remove the oxide on top of copper surface and increase the copper grain size[256]. For the stage 1 of the graphene growth, gas mixture of CH_4/H_2 (1.3 sccm : 2 sccm) is introduced for 1 hour. Large graphene grains ($\sim$ 50 μm) are formed during this stage. After stage 1, gas mixture of CH_4/H_2 (35 sccm : 2 sccm) is introduced

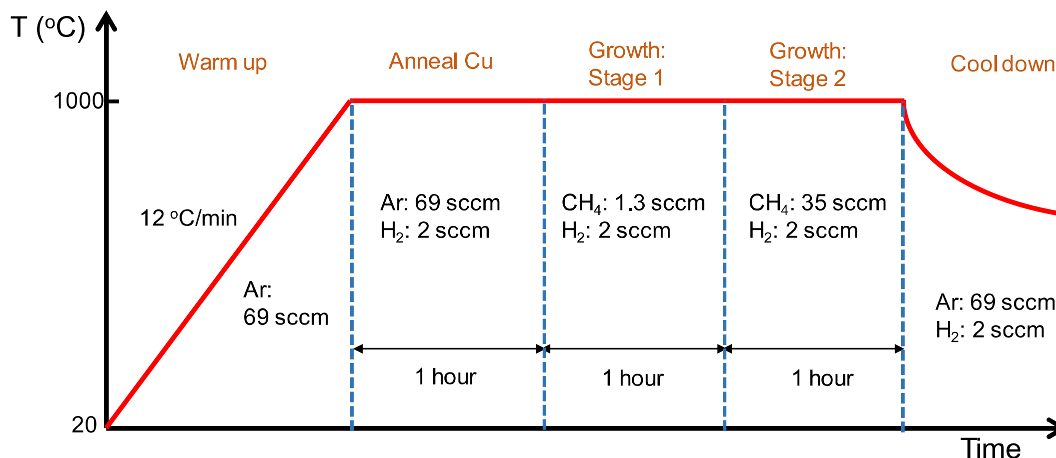

Figure 7.4: Growth recipe for our CVD graphene. Red line shows how the system temperature changes with growth time. They are five steps in a complete growth process.

for another 1 hour to form a continuous graphene film. After the graphene growth, furnace is cooled down to room temperature under the flow of Ar/H_2 (69 sccm: 2 sccm). In the cooling down stage, the presence of H_2 was found to be important to get continuous graphene film.

SEM image of some graphene grown on copper is show in Fig. 7.5. InLense mode (detecting backscattered electrons) was found to give better graphene visibility than secondary electron detector. Fig. 7.5(**a**) is copper foil before anneal in the furnace. The surface is very rough and has plane structures with different orientation. Fig. 7.5(**b**) is copper foil after 45 sec graphene growth without a bag. The graphene is seem as the dark area polygons. Graphene size is $\sim 2\ \mu$m. Fig. 7.5(**c**) shows the graphene on the outside of the copper bag with low flow of methane. The grain size of the graphene is bigger compared to Fig. 7.5(**b**). Fig. 7.5(**d**) shows the graphene on the inside of the bag. Even bigger graphene grains can be seem. Graphene grown on the copper piece that is placed inside of the bag looks similar to Fig. 7.5(**d**).

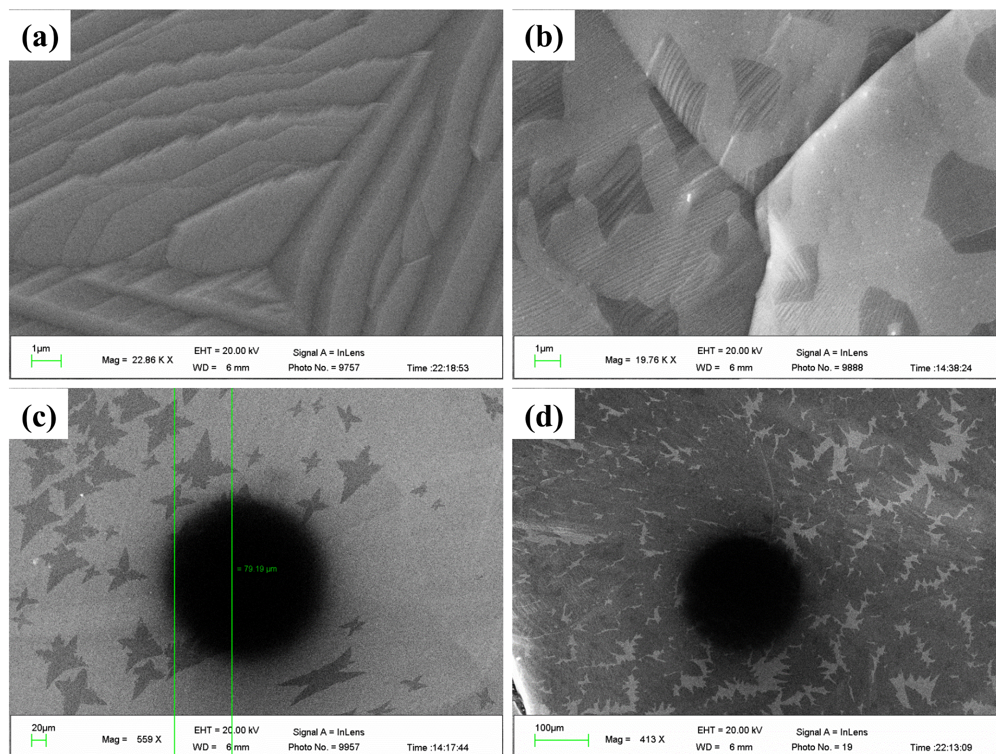

Figure 7.5: SEM image of copper foil and grown graphene on top. See the main text for more details about each graph.

7.3 Transfer

After graphene is grown on copper foil, it needs to be transferred to other substrates for electrical characterization. The transfer process is illustrated in Fig. 7.6. Firstly, copper foil with graphene grown on both sides is cut into pieces of $\sim 1\times1$ cm. Then a thin PMMA layer is spin coated on the top side of copper foil at 2000 rpm for 45 sec, followed by baking at 180 °C for 1 min. After baking copper foil is placed onto ammonium persulfate ($(NH_4)_2S_2O_8$) solution with 1 - 2 mol/L concentration. Copper foil floats on top of the solution. 5 min sonication is applied to the solution with copper foil to get rid of the back side graphene. Another 5 - 10 min without sonication is given to remove much of the copper. While the copper foil starts to become transparent, it is transferred to another ammonium persulfate solution with 0.1 mol/L concentration. Usually after $\sim$ 3 hours the graphene with PMMA film looks free of copper.

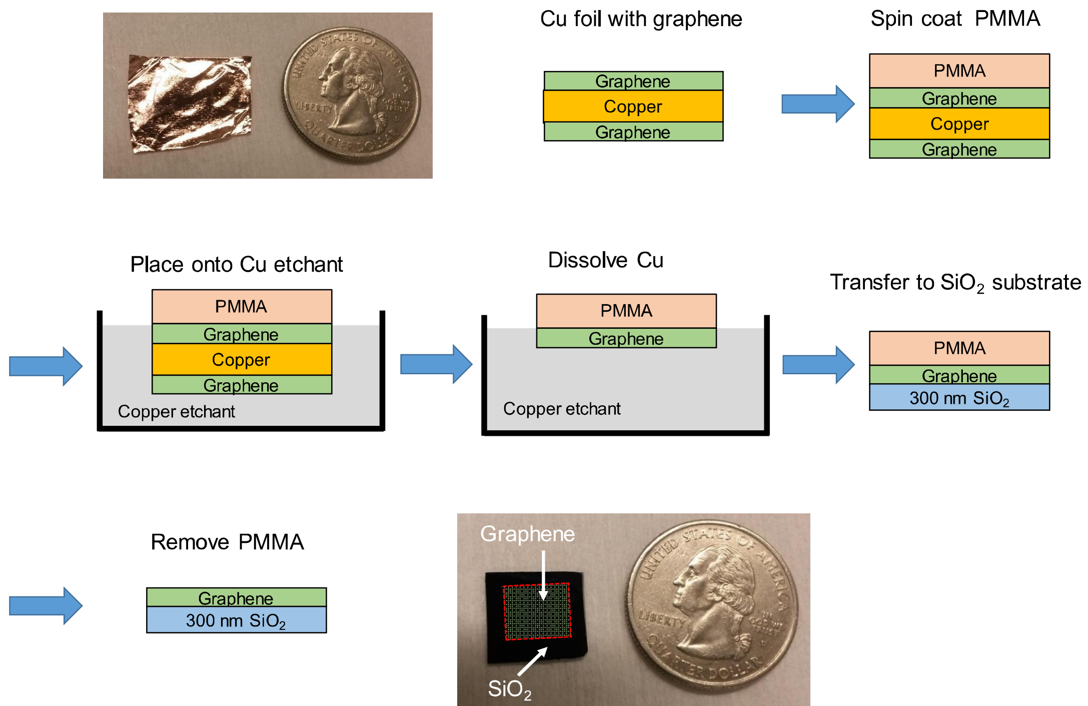

Figure 7.6: Transfer of as-grown graphene to SiO_2 substrate. The bottom right picture shows graphene on SiO_2 substrate.

Then the graphene/PMMA film is transferred to deionized (DI) water solution using a spoon. Spoon is helpful because graphene will only touch the flexible solution instead of any solid parts. After rinsing in DI water for 30 mins, graphene/PMMA film is transferred onto a clean SiO_2 substrate by placing SiO_2 substrate underneath the graphene and gently pulled out. This is the step that determines how good the graphene is attaching to the substrate. Then the substrate with graphene/PMMA ontop is baked at 50 °C for 20 mins. to get rid of the water. Finally, PMMA is removed by placing the substrate in room temperature acetone for 20 min. (In this step, Remover PG was found to create crakes on LAG when it was used to remove the PMMA layer compared to acetone.) Substrate is then blow dry with nitrogen after removing PMMA. The image of transferred graphene on SiO_2 substrate is shown in bottom right of Fig. 7.6.

Optical microscope was firstly used to check the quality of graphene. Normally there is no crakes across an areas of $\sim$ mm$\times$mm. An optical image is show in Fig. 7.7(**a**). Graphene

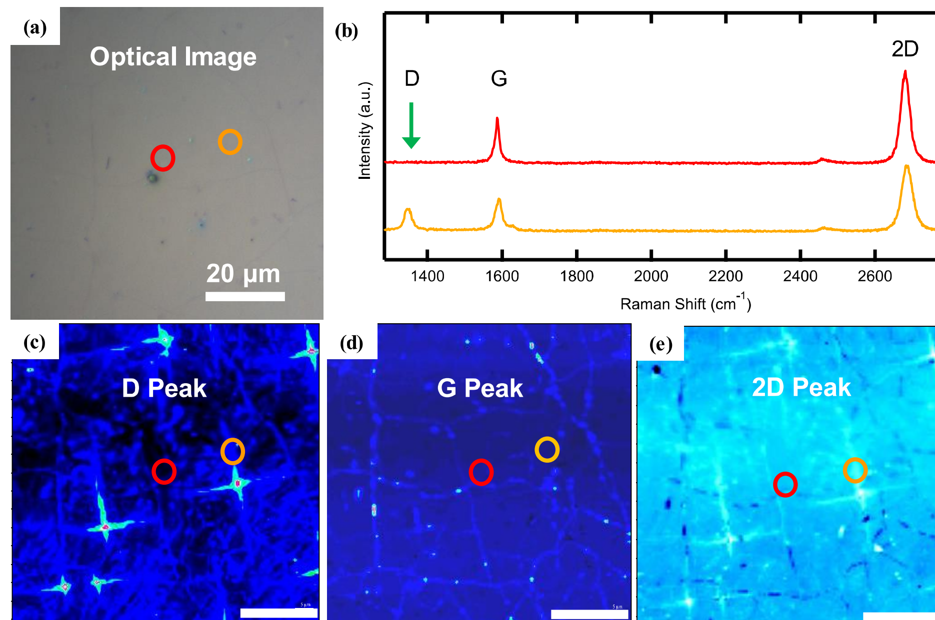

Figure 7.7: Raman spectra for transferred graphene on SiO_2. **(a)** Optical Image of a transferred LAG on SiO_2 substrate. **(b)** Raman spectra for two different graphene spots as show in **(a)** (yellow and red circled area). **(c)**-**(e)** Raman mapping of D, G and 2D peak, respectively, for the graphene in **(a)**. Scale bar is 20 μm.

is continuous over 100 μm. Raman spectra was examined on the transferred graphene as show in Fig. 7.7**(b)**. The two Raman spectra were taken at two spots indicated in Fig. 7.7**(a)**. Except the area close to nucleation sites, defect peak (D peak) is absent. Lorentz fit for the 2D peak confirms the grown graphene is single layer. Raman mapping of the graphene area in Fig. 7.7**(a)** is shown in Fig. 7.7**(c)**-**(e)** for D peak, G peak and 2D peak, respectively. Over the scanned area the majority of the graphene film has no or small D peak, indicating good quality of the graphene.

7.4 Graphene Spin Valves Fabrication

In order to fabricate a device using transferred LAG, etching is need to remove graphene that may shunt the electrical measurement. The steps are show in Fig. 7.8. Firstly, bilayer of

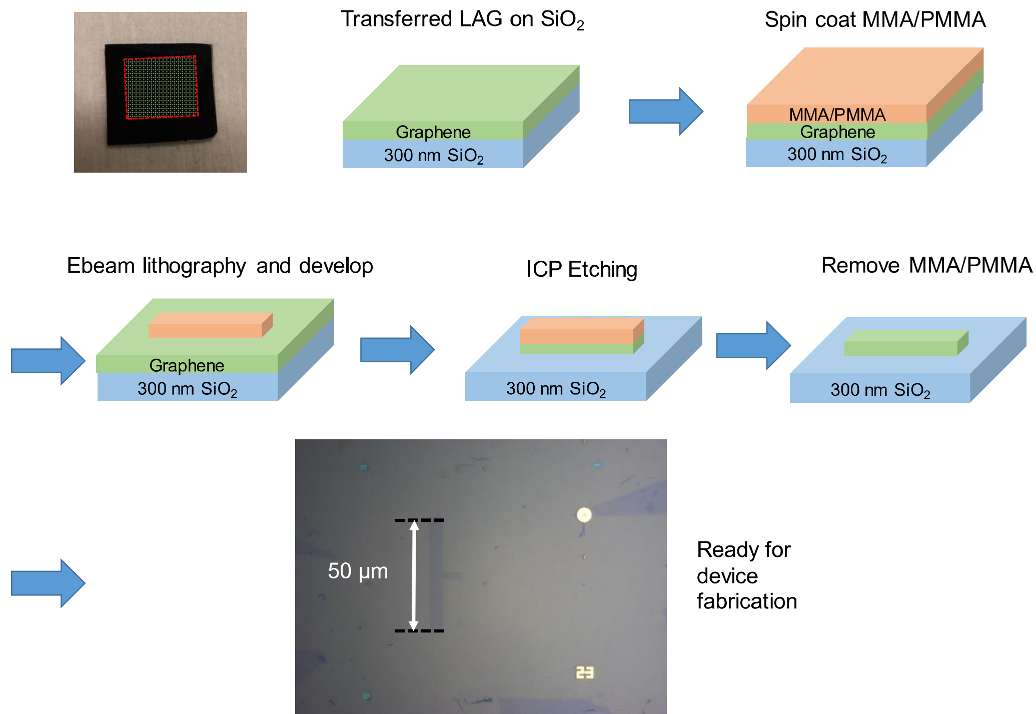

Figure 7.8: Etch down LAG for device fabrication. MMA/PMMA is used as etching mask. The final image of the etched graphene is shown in the middle bottom figure. A strip of $\sim 3.5\times 50$ μm graphene is left after the etching.

MMA/PMMA is spin coated on LAG using the same recipe as described in chapter 3. EBL is used to pattern the graphene parts that needs to be etched away. After develop, graphene that needs to stay are covered with MMA/PMMA and the rest is exposed to air. Reactive ion etching (RIE) and Inductively coupled plasma (ICP) are the two common ways to remove graphene in large volume. In this thesis ICP (1 sec, 50 W ICP power) is used to remove graphene. Finally, MMA/PMMA protecting layer is removed in acetone. The final device image is shown in the middle bottom of Fig. 7.8. A strip of $\sim 3.5\times 50$ μm graphene is left after the etching.

Spin valve device on etched LAG is fabricated as described in chapter 3. Both tunnel barrier and transparent spin valves[148] were fabricated on etched LAG but spin transport signals were only obtained using transparent contacts. The structure of transparent contact is shown in Fig. 7.9(**b**). In this case Co is directly contacting graphene with 2 nm MgO as masking

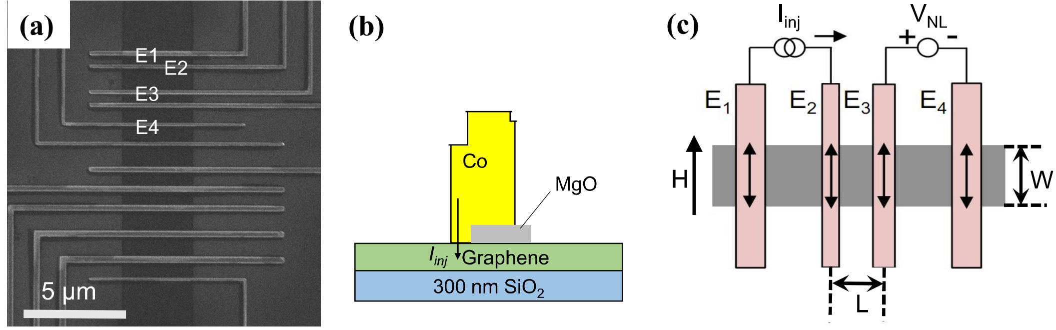

Figure 7.9: Fabricated LAG spin valves. **(a)** SEM image of a fabricated spin valve on etched CVD graphene. All the Co electrodes are transparent contacts. **(b)** Schematic diagram of transparent contact structure. **(c)** Schematic diagram of nonlocal MR measurement.

layer to reduce the contact area. Angle deposition in MBE chamber is utilized to achieve this structure. SEM image of the final device is shown in Fig. 7.9(**a**). Twelve Co electrodes were fabricated on etched LAG with spacing 1 - 3 μm.

7.5 Spin Valve Measurement

Nonlocal measurement geometry is used to probe spin transport in fabricated graphene spin valve on LAG, as shown in Fig. 7.9(**c**). Width (W) of the graphene is 3.5 μm and length of the graphene channel (L) between E_2 and E_3 is 2 μm. Contact resistance of E_2 and E_3 are 675 Ω and 529 Ω, respectively.

100 μA AC current I_{inj} is applied between E_2 and E_1, and nonlocal voltage V_{NL} is detected between E_3 and E_4 using a lock-in amplifier. Clear switchings in detected MR signal (4 - 12 mΩ) shows the spin transport in LAG (Fig. 7.10(**a**)). Gate dependence of measured ΔR_{NL} is shown in Fig. 7.10(**b**). In the limit of $R_{Contact} \ll R_{Graphene}$, ΔR_{NL} is predicted to be[44]:

$$\Delta R_{NL} = 4P_{J2}P_{J3}R_{C2}R_{C3}W\sigma_G e^{-L/\lambda_G}\left[\lambda_G(1-e^{-L/\lambda_G})\right]^{-1} \sim \sigma_G \tag{7.1}$$

where σ_G is conductivity of graphene, P_{J2} and P_{J2} are the interfacial spin polarization for electrodes E_2 and E_3, respectively, R_{C2} and R_{C3} are the contact resistance for electrodes E_2 and E_3,

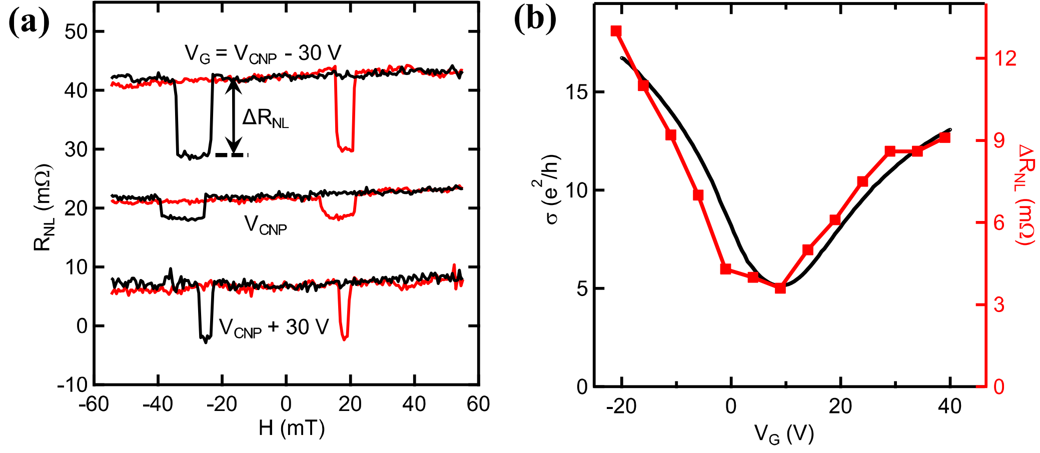

Figure 7.10: Nonlocal spin transport signal on the device. **(a)** Nonlocal resistance at electron, hole and charge neutrality graphene. V_{CNP} is at +9 V gate voltage. **(b)** ΔR_{NL} as a function of gate voltage. It shows the typical transparent contact behavior.

respectively and λ_G is the spin diffusion length in graphene. The results agrees with the theory very well.

7.6 Conclusion

We have achieved successful spin injection and detection in CVD grown large area graphene at room temperature using transparent ferromagnetic contact. The measured spin transport signal is described well by a one-dimensional drift-diffusion equation. This provides an important step toward future integration of spintronic devices with large area graphene.

Chapter 8

Conclusions

This thesis has discussed several steps moving towards realizing magneto-logic gate in graphene. Normal lateral graphene spin valve was used as the model system and starting point.

Firstly, current-based detection of spin transport in graphene was demonstrated. A way to systematically tune the detection from voltage based to current based was developed. Theoretical analysis was performed in the frame of one dimensional drift-diffusion model. Experimental observation was found to agree well with the model. The capability of using current to detection spins is important for the proposed magneto-logic device.

Secondly, bias dependent spin injection in Co/MgO/Graphene junction was observed. Positive bias on the junction (current flow from Co to graphene) was found to increase the observed spin signal, and negative bias was found to decrease, even reverse the measured AC spin signal. This strong bias dependence has been observed over contacts that have significant different contact resistance (5 - 80 kΩ). Further studies on this is on going.

Thirdly, XOR logic operation is demonstrated in graphene devices with three ferromagnetic electrodes. The magnetization direction of two of the ferromagnetic electrodes are

used as logic input and the logic output is a current signal. When the two inputs are the same ('00' or '11'), the output current is zero, representing logic '0'. When the two inputs are not the same ('01' or '10'), the output current is not zero, representing logic '1'. One of the challenges is to tune the two inputs to have same contribution on the output. This was achieved by adding bias in the current injection loop, and utilize the bias dependent spin injection discussed above.

Lastly, spin transport across large area epitaxy graphene was achieved. Graphene was grown by chemical vapor deposition on copper foil, transferred to SiO_2 substrate, and etched for device fabrication. Transparent spin valves were fabricated on the etched graphene. Successful spin injection and transport was observed, which agrees well with the behavior for transparent contacts. This work demonstrates the ability of using epitaxy graphene as spin transport channel.

In terms of moving forward, they are several things need to be done to achieve the full five terminal magneto-logic gate. The first thing is to demonstrate XOR logic on small devices. Logic performance is predicted to improve because current for logic '1' output is going to be much bigger. The second one is to expand two inputs to four inputs, so the full logic operation can be achieved. The third one is to integrate spin transfer torque in the device so the inputs can be set by electrical current instead of external magnetic field.

Bibliography

[1] S. A. Wolf, D. D. Awschalom, R. A. Buhrman, J. M. Daughton, S. von Molnr, M. L. Roukes, A. Y. Chtchelkanova, and D. M. Treger. Spintronics: A spin-based electronics vision for the future. *Science*, 294(5546):1488–1495, 2001.

[2] Igor Žutić, Jaroslav Fabian, and S. Das Sarma. Spintronics: Fundamentals and applications. *Rev. Mod. Phys.*, 76:323–410, Apr 2004.

[3] E. C. Stoner and E. P. Wohlfarth. A mechanism of magnetic hysteresis in heterogeneous alloys. *Philosophical Transactions of the Royal Society of London A: Mathematical, Physical and Engineering Sciences*, 240(826):599–642, 1948.

[4] Mark Johnson and R. H. Silsbee. Coupling of electronic charge and spin at a ferromagnetic-paramagnetic metal interface. *Phys. Rev. B*, 37:5312–5325, Apr 1988.

[5] N. F. Mott. The electrical conductivity of transition metals. *Proceedings of the Royal Society of London. Series A, Mathematical and Physical Sciences*, 153(880):pp. 699–717, 1936.

[6] N. F. Mott. The resistance and thermoelectric properties of the transition metals. *Proceedings of the Royal Society of London. Series A, Mathematical and Physical Sciences*, 156(888):pp. 368–382, 1936.

[7] I. A. Campbell, A. Fert, and R. Pomeroy. Evidence for two current conduction iron. *Philosophical Magazine*, 15(137):977–983, 1967.

[8] A. Fert and I. Campbell. Two-current conduction in nickel. *Phys. Rev. Lett.*, 21:1190–1192, Oct 1968.

[9] M. N. Baibich, J. M. Broto, A. Fert, F. Nguyen Van Dau, F. Petroff, P. Etienne, G. Creuzet, A. Friederich, and J. Chazelas. Giant magnetoresistance of (001)fe/(001)cr magnetic superlattices. *Phys. Rev. Lett.*, 61:2472–2475, Nov 1988.

[10] G. Binasch, P. Grünberg, F. Saurenbach, and W. Zinn. Enhanced magnetoresistance in layered magnetic structures with antiferromagnetic interlayer exchange. *Phys. Rev. B*, 39:4828–4830, Mar 1989.

[11] R. Camley and J. Barnaś. Theory of giant magnetoresistance effects in magnetic layered structures with antiferromagnetic coupling. *Phys. Rev. Lett.*, 63:664–667, Aug 1989.

[12] T. Valet and A. Fert. Theory of the perpendicular magnetoresistance in magnetic multilayers. *Phys. Rev. B*, 48:7099–7113, Sep 1993.

[13] M. Julliere. Tunneling between ferromagnetic films. *Physics Letters A*, 54(3):225 – 226, 1975.

[14] T. Miyazaki and N. Tezuka. Giant magnetic tunneling effect in fe/al2o3/fe junction. *Journal of Magnetism and Magnetic Materials*, 139(3):L231 – L234, 1995.

[15] J. S. Moodera, Lisa R. Kinder, Terrilyn M. Wong, and R. Meservey. Large magnetoresistance at room temperature in ferromagnetic thin film tunnel junctions. *Phys. Rev. Lett.*, 74:3273–3276, Apr 1995.

[16] W. H. Butler, X.-G. Zhang, T. C. Schulthess, and J. M. MacLaren. Spin-dependent tunneling conductance of Fe|MgO|Fe sandwiches. *Phys. Rev. B*, 63:054416, Jan 2001.

[17] J. Mathon and A. Umerski. Theory of tunneling magnetoresistance of an epitaxial fe/mgo/fe(001) junction. *Phys. Rev. B*, 63:220403, May 2001.

[18] Stuart S. P. Parkin, Christian Kaiser, Alex Panchula, Philip M. Rice, Brian Hughes, Mahesh Samant, , and See-Hun Yang. Giant tunnelling magnetoresistance at room temperature with mgo (100) tunnel barriers. *Nature Materials*, 3(10):862–867, 2004.

[19] Shinji Yuasa, Taro Nagahama, Akio Fukushima, Yoshishige Suzuki, and Koji Ando. Giant room-temperature magnetoresistance in single-crystal Fe/MgO/Fe magnetic tunnel junctions. *Nat Mater*, 3(12):868–871, December 2004.

[20] David D. Djayaprawira, Koji Tsunekawa, Motonobu Nagai, Hiroki Maehara, Shinji Yamagata, Naoki Watanabe, Shinji Yuasa, Yoshishige Suzuki, and Koji Ando. 230magnetic tunnel junctions. *Applied Physics Letters*, 86(9):–, 2005.

[21] Shinji Yuasa, Akio Fukushima, Hitoshi Kubota, Yoshishige Suzuki, and Koji Ando. Giant tunneling magnetoresistance up to 410fully epitaxial comgoco magnetic tunnel junctions with bcc co(001) electrodes. *Applied Physics Letters*, 89(4):–, 2006.

[22] S. Yuasa and D. D. Djayaprawira. Giant tunnel magnetoresistance in magnetic tunnel junctions with a crystalline mgo(001) barrier. *Journal of Physics D: Applied Physics*, 40(21):R337, 2007.

[23] S. Ikeda, J. Hayakawa, Y. Ashizawa, Y. M. Lee, K. Miura, H. Hasegawa, M. Tsunoda, F. Matsukura, and H. Ohno. Tunnel magnetoresistance of 604% at 300k by suppression of ta diffusion in cofebmgocofeb pseudo-spin-valves annealed at high temperature. *Applied Physics Letters*, 93(8), 2008.

[24] S Ikeda, K Miura, H Yamamoto, K Mizunuma, H D Gan, M Endo, S Kanai, J Hayakawa, F Matsukura, and H Ohno. A perpendicular-anisotropy CoFeBMgO magnetic tunnel junction. *Nat Mater*, 9(9):721–724, September 2010.

[25] Albert Fert. Nobel lecture: Origin, development, and future of spintronics. *Rev. Mod. Phys.*, 80:1517–1530, Dec 2008.

[26] Claude Chappert, Albert Fert, and Frdric Nguyen Van Dau. The emergence of spin electronics in data storage. *Nature Materials*, 6:813–823, 2007.

[27] S.D. Bader and S.S.P. Parkin. Spintronics. *Annual Review of Condensed Matter Physics*, 1(1):71–88, 2010.

[28] Supriyo Datta and Biswajit Das. Electronic analog of the electrooptic modulator. *Applied Physics Letters*, 56(7):665–667, 1990.

[29] H. Dery, P. Dalal, L. Cywinski, and L. J. Sham. Spin-based logic in semiconductors for reconfigurable large-scale circuits. *Nature*, 447:573–576, 2007.

[30] Behtash Behin-Aein, Deepanjan Datta, Sayeef Salahuddin, and Supriyo Datta. Proposal for an all-spin logic device with built-in memory. *Nat Nano*, 5(4):266–270, April 2010.

[31] Mark Johnson and R. Silsbee. Thermodynamic analysis of interfacial transport and of the thermomagnetoelectric system. *Phys. Rev. B*, 35:4959–4972, Apr 1987.

[32] P. C. van Son, H. van Kempen, and P. Wyder. Boundary resistance of the ferromagnetic-nonferromagnetic metal interface. *Phys. Rev. Lett.*, 58:2271–2273, May 1987.

[33] Selman Hershfield and Hui Zhao. Charge and spin transport through a metallic ferromagnetic-paramagnetic-ferromagnetic junction. *Phys. Rev. B*, 56:3296–3305, Aug 1997.

[34] E. I. Rashba. Theory of electrical spin injection: Tunnel contacts as a solution of the conductivity mismatch problem. *Phys. Rev. B*, 62:R16267–R16270, Dec 2000.

[35] G. Schmidt, D. Ferrand, L. W. Molenkamp, A. T. Filip, and B. J. van Wees. Fundamental obstacle for electrical spin injection from a ferromagnetic metal into a diffusive semiconductor. *Phys. Rev. B*, 62:R4790–R4793, Aug 2000.

[36] F. Bloch. Nuclear induction. *Phys. Rev.*, 70:460–474, Oct 1946.

[37] H. Torrey. Bloch equations with diffusion terms. *Phys. Rev.*, 104:563–565, Nov 1956.

[38] Mark Johnson and R. H. Silsbee. Interfacial charge-spin coupling: Injection and detection of spin magnetization in metals. *Phys. Rev. Lett.*, 55:1790–1793, Oct 1985.

[39] Wilhelm Hanle. ber magnetische beeinflussung der polarisation der resonanzfluoreszenz. *Zeitschrift fr Physik*, 30(1):93–105, 1924.

[40] FJ Jedema, AT Filip, and BJ Van Wees. Electrical spin injection and accumulation at room temperature in an all-metal mesoscopic spin valve. *Nature*, 410(6826):345–348, 2001.

[41] FJ Jedema, HB Heersche, AT Filip, JJ Baselmans, BJ van Wees, et al. Electrical detection of spin precession in a metallic mesoscopic spin valve. *Nature*, 416(6882):713, 2002.

[42] F. J. Jedema, M. S. Nijboer, A. T. Filip, and B. J. van Wees. Spin injection and spin accumulation in all-metal mesoscopic spin valves. *Phys. Rev. B*, 67:085319, Feb 2003.

[43] A. Filip, B. Hoving, F. Jedema, B. J. van Wees, B. Dutta, and S. Borghs. Experimental search for the electrical spin injection in a semiconductor. *Phys. Rev. B*, 62:9996–9999, Oct 2000.

[44] S. Takahashi and S. Maekawa. Spin injection and detection in magnetic nanostructures. *Phys. Rev. B.*, 67:052409, 2003.

[45] Tao Yang, Takashi Kimura, and Yoshichika Otani. Giant spin-accumulation signal and pure spin-current-induced reversible magnetization switching. *Nat Phys*, 4(11):851–854, November 2008.

[46] H. Idzuchi, Y. Fukuma, L. Wang, and Y. Otani. Spin relaxation mechanism in silver nanowires covered with mgo protection layer. *Applied Physics Letters*, 101(2):–, 2012.

[47] Y Ohno, D K Young, B Beschoten, F Matsukura, H Ohno, and D D Awschalom. Electrical spin injection in a ferromagnetic semiconductor heterostructure. *Nature*, 402(6763):790–792, December 1999.

[48] V. F. Motsnyi, J. De Boeck, J. Das, W. Van Roy, G. Borghs, E. Goovaerts, and V. I. Safarov. Electrical spin injection in a ferromagnet/tunnel barrier/semiconductor heterostructure. *Applied Physics Letters*, 81(2):265–267, 2002.

[49] Xiaohua Lou, Christoph Adelmann, Scott A. Crooker, Eric S. Garlid, Jianjie Zhang, K. S. Madhukar Reddy, Soren D. Flexner, Chris J. Palmstrm, and Paul A. Crowell. Electrical detection of spin transport in lateral ferromagnetsemiconductor devices. *Nature Physics*, 3:197–202, 2007.

[50] Ian Appelbaum, Biqin Huang, and Douwe J Monsma. Electronic measurement and control of spin transport in silicon. *Nature*, 447(7142):295–298, May 2007.

[51] Berend T Jonker, George Kioseoglou, Aubrey T Hanbicki, Connie H Li, and Phillip E Thompson. Electrical spin-injection into silicon from a ferromagnetic metal/tunnel barrier contact. *Nat Phys*, 3(8):542–546, August 2007.

[52] Yi Zhou, Wei Han, Li-Te Chang, Faxian Xiu, Minsheng Wang, Michael Oehme, Inga Fischer, Joerg Schulze, Roland. Kawakami, and Kang Wang. Electrical spin injection and transport in germanium. *Phys. Rev. B*, 84:125323, Sep 2011.

[53] Z H Xiong, Di Wu, Z Valy Vardeny, and Jing Shi. Giant magnetoresistance in organic spin-valves. *Nature*, 427(6977):821–824, February 2004.

[54] Kazuhito Tsukagoshi, Bruce W Alphenaar, and Hiroki Ago. Coherent transport of electron spin in a ferromagnetically contacted carbon nanotube. *Nature*, 401(6753):572–574, October 1999.

[55] N. Tombros, C. Jozsa, M. Popinciuc, H. T. Jonkman, and B. J. Van Wees. Electronic spin transport and spin precession in single graphene layers at room temperature. *Nature*, 448:571–574, 2007.

[56] Kin Fai Mak, Changgu Lee, James Hone, Jie Shan, and Tony F. Heinz. Atomically thin mos_2: A new direct-gap semiconductor. *Phys. Rev. Lett.*, 105:136805, Sep 2010.

[57] Kin Fai Mak, Keliang He, Jie Shan, and Tony F Heinz. Control of valley polarization in monolayer MoS2 by optical helicity. *Nat Nano*, 7(8):494–498, aug 2012.

[58] M. H. D. Guimarães, P. J. Zomer, J. Ingla-Aynés, J. C. Brant, N. Tombros, and B. J. van Wees. Controlling spin relaxation in hexagonal bn-encapsulated graphene with a transverse electric field. *Phys. Rev. Lett.*, 113:086602, Aug 2014.

[59] B. Dlubak, M.-B. Martin, C. Deranlot, B. Servet, S. Xavier, R. Mattana, M. Sprinkle, C. Berger, W. A. De Heer, F. Petroff, A. Anane, P. Seneor, and A. Fert. Highly efficient spin transport in epitaxial graphene on sic. *Nature Phys.*, 8:557–561, 2012.

[60] Wei Han, K. Pi, K. M. McCreary, Yan Li, J. J. I. Wong, A. G. Swartz, and R. K. Kawakami. Tunneling spin injection into single layer graphene. *Phys. Rev. Lett.*, 105:167202, 2010.

[61] A K Geim and K S Novoselov. The rise of graphene. *Nat Mater*, 6(3):183–191, March 2007.

[62] A. H. Castro Neto, F. Guinea, N. M. R. Peres, K. S. Novoselov, and A. K. Geim. The electronic properties of graphene. *Rev. Mod. Phys.*, 81:109–162, Jan 2009.

[63] S. Das Sarma, Shaffique Adam, E. Hwang, and Enrico Rossi. Electronic transport in two-dimensional graphene. *Rev. Mod. Phys.*, 83:407–470, May 2011.

[64] A. Hull. A new method of x-ray crystal analysis. *Phys. Rev.*, 10:661–696, Dec 1917.

[65] P. R. Wallace. The band theory of graphite. *Phys. Rev.*, 71:622, 1947.

[66] D. DiVincenzo and E. Mele. Self-consistent effective-mass theory for intralayer screening in graphite intercalation compounds. *Phys. Rev. B*, 29:1685–1694, Feb 1984.

[67] S Y Zhou, G.-H. Gweon, J Graf, A V Fedorov, C D Spataru, R D Diehl, Y Kopelevich, D.-H. Lee, Steven G Louie, and A Lanzara. First direct observation of Dirac fermions in graphite. *Nat Phys*, 2(9):595–599, September 2006.

[68] R. Deacon, K.-C. Chuang, R. Nicholas, K. Novoselov, and A. Geim. Cyclotron resonance study of the electron and hole velocity in graphene monolayers. *Phys. Rev. B*, 76:081406, Aug 2007.

[69] Z. Jiang, E. Henriksen, L. Tung, Y.-J. Wang, M. Schwartz, M. Han, P. Kim, and H. Stormer. Infrared spectroscopy of landau levels of graphene. *Phys. Rev. Lett.*, 98:197403, May 2007.

[70] E. H. Hwang and S. Das Sarma. Acoustic phonon scattering limited carrier mobility in two-dimensional extrinsic graphene. *Phys. Rev. B*, 77:115449, Mar 2008.

[71] Jian-Hao Chen, Chaun Jang, Shudong Xiao, Masa Ishigami, and Michael S Fuhrer. Intrinsic and extrinsic performance limits of graphene devices on SiO2. *Nat Nano*, 3(4):206–209, apr 2008.

[72] Xu Du, Ivan Skachko, Anthony Barker, and Eva Y Andrei. Approaching ballistic transport in suspended graphene. *Nat Nano*, 3(8):491–495, August 2008.

[73] R. Peierls. Quelques proprits typiques des corps solides. *Annales de l'institut Henri Poincar*, 5(3):177–222, 1935.

[74] L. D. Landau. Zur Theorie der phasenumwandlungen II. *Phys. Z. Sowjetunion*, 11:26–35, 1937.

[75] K. S. Novoselov, A. K. Geim, S. V. Morozov, D. Jiang, Y. Zhang, S. V. Dubonos, I. V. Grigorieva, and A. A. Firsov. Electric field effect in atomically thin carbon films. *Science*, 306(5696):666–669, 2004.

[76] I. W. Frank, D. M. Tanenbaum, A. M. van der Zande, and P. L. McEuen. Mechanical properties of suspended graphene sheets. *Journal of Vacuum Science & Technology B*, 25(6):2558–2561, 2007.

[77] Jannik C Meyer, A K Geim, M I Katsnelson, K S Novoselov, T J Booth, and S Roth. The structure of suspended graphene sheets. *Nature*, 446(7131):60–63, March 2007.

[78] Changgu Lee, Xiaoding Wei, Jeffrey W. Kysar, and James Hone. Measurement of the elastic properties and intrinsic strength of monolayer graphene. *Science*, 321(5887):385–388, 2008.

[79] Changyao Chen, Sami Rosenblatt, Kirill I Bolotin, William Kalb, Philip Kim, Ioannis Kymissis, Horst L Stormer, Tony F Heinz, and James Hone. Performance of monolayer graphene nanomechanical resonators with electrical readout. *Nat Nano*, 4(12):861–867, December 2009.

[80] Xuesong Li, Weiwei Cai, Jinho An, Seyoung Kim, Junghyo Nah, Dongxing Yang, Richard Piner, Aruna Velamakanni, Inhwa Jung, Emanuel Tutuc, Sanjay K. Banerjee, Luigi Colombo, and Rodney S. Ruoff. Large-area synthesis of high-quality and uniform graphene films on copper foils. *Science*, 324(5932):1312–1314, 2009.

[81] Sukang Bae, Hyeongkeun Kim, Youngbin Lee, Xiangfan Xu, Jae-Sung Park, Yi Zheng, Jayakumar Balakrishnan, Tian Lei, Hye Ri Kim, Young Il Song, Young-Jin Kim, Kwang S Kim, Barbaros Ozyilmaz, Jong-Hyun Ahn, Byung Hee Hong, and Sumio Iijima. Roll-to-roll production of 30-inch graphene films for transparent electrodes. *Nat Nano*, 5(8):574–578, August 2010.

[82] F Schedin, A K Geim, S V Morozov, E W Hill, P Blake, M I Katsnelson, and K S Novoselov. Detection of individual gas molecules adsorbed on graphene. *Nat Mater*, 6(9):652–655, September 2007.

[83] Martin Pumera. Electrochemistry of graphene: new horizons for sensing and energy storage. *The Chemical Record*, 9(4):211–223, 2009.

[84] Jun Yao, Yu Sun, Mei Yang, and Yixiang Duan. Chemistry, physics and biology of graphene-based nanomaterials: new horizons for sensing, imaging and medicine. *J. Mater. Chem.*, 22:14313–14329, 2012.

[85] Ruben Mas-Balleste, Cristina Gomez-Navarro, Julio Gomez-Herrero, and Felix Zamora. 2d materials: to graphene and beyond. *Nanoscale*, 3:20–30, 2011.

[86] Sheneve Z. Butler, Shawna M. Hollen, Linyou Cao, Yi Cui, Jay A. Gupta, Humberto R. Gutirrez, Tony F. Heinz, Seung Sae Hong, Jiaxing Huang, Ariel F. Ismach, Ezekiel Johnston-Halperin, Masaru Kuno, Vladimir V. Plashnitsa, Richard D. Robinson, Rodney S. Ruoff, Sayeef Salahuddin, Jie Shan, Li Shi, Michael G. Spencer, Mauricio Terrones, Wolfgang Windl, and Joshua E. Goldberger. Progress, challenges, and opportunities in two-dimensional materials beyond graphene. *ACS Nano*, 7(4):2898–2926, 2013. PMID: 23464873.

[87] Gianluca Fiori, Francesco Bonaccorso, Giuseppe Iannaccone, Tomas Palacios, Daniel Neumaier, Alan Seabaugh, Sanjay K Banerjee, and Luigi Colombo. Electronics based on two-dimensional materials. *Nat Nano*, 9(10):768–779, October 2014.

[88] Manish Chhowalla, Hyeon Suk Shin, Goki Eda, Lain-Jong Li, Kian Ping Loh, and Hua Zhang. The chemistry of two-dimensional layered transition metal dichalcogenide nanosheets. *Nat Chem*, 5(4):263–275, April 2013.

[89] Andre K Geim. Nobel lecture: Random walk to graphene. *Reviews of Modern Physics*, 83(3):851, 2011.

[90] K. S. Novoselov, A. K. Geim, S. V. Morozov, D. Jiang, M. I. Katsnelson, I. V. Grigorieva, S. V. Dubonos, and A. A. Firsov. Two-dimensional gas of massless dirac fermions in graphene. *Nature*, 438:197, 2005.

[91] Y. Zhang, Y.-W. Tan, H. L. Stormer, and P. Kim. Experimental observation of the quantum hall effect and berry's phase in graphene. *Nature*, 438:201, 2005.

[92] Di Xiao, Ming-Che Chang, and Qian Niu. Berry phase effects on electronic properties. *Rev. Mod. Phys.*, 82:1959–2007, Jul 2010.

[93] K. S. Novoselov, Z. Jiang, Y. Zhang, S. V. Morozov, H. L. Stormer, U. Zeitler, J. C. Maan, G. S. Boebinger, P. Kim, and A. K. Geim. Room-temperature quantum hall effect in graphene. *Science*, 315(5817):1379, 2007.

[94] Y.-W. Tan, Y. Zhang, K. Bolotin, Y. Zhao, S. Adam, E. H. Hwang, S. Das Sarma, H. L. Stormer, and P. Kim. Measurement of scattering rate and minimum conductivity in graphene. *Phys. Rev. Lett.*, 99:246803, Dec 2007.

[95] L. A. Ponomarenko, R. Yang, T. M. Mohiuddin, M. I. Katsnelson, K. S. Novoselov, S. V. Morozov, A. A. Zhukov, F. Schedin, E. W. Hill, and A. K. Geim. Effect of a high-κ environment on charge carrier mobility in graphene. *Phys. Rev. Lett.*, 102:206603, May 2009.

[96] Kentaro Nomura and A. H. MacDonald. Quantum transport of massless dirac fermions. *Phys. Rev. Lett.*, 98:076602, Feb 2007.

[97] Tsuneya Ando. Screening effect and impurity scattering in monolayer graphene. *Journal of the Physical Society of Japan*, 75(7):074716, 2006.

[98] E. H. Hwang, S. Adam, and S. Das Sarma. Carrier transport in two-dimensional graphene layers. *Phys. Rev. Lett.*, 98:186806, May 2007.

[99] C. Jang, S. Adam, J.-H. Chen, E. D. Williams, S. Das Sarma, and M. S. Fuhrer. Tuning the effective fine structure constant in graphene: Opposing effects of dielectric screening on short- and long-range potential scattering. *Phys. Rev. Lett.*, 101:146805, Oct 2008.

[100] Masa Ishigami, J. H. Chen, W. G. Cullen, M. S. Fuhrer, and E. D. Williams. Atomic structure of graphene on sio2. *Nano Letters*, 7(6):1643–1648, 2007. PMID: 17497819.

[101] S. V. Morozov, K. S. Novoselov, M. I. Katsnelson, F. Schedin, D. C. Elias, J. A. Jaszczak, and A. K. Geim. Giant intrinsic carrier mobilities in graphene and its bilayer. *Phys. Rev. Lett.*, 100:016602, Jan 2008.

[102] M.I Katsnelson and A.K Geim. Electron scattering on microscopic corrugations in graphene. *Philosophical Transactions of the Royal Society A: Mathematical, Physical and Engineering Sciences*, 366(1863):195–204, 2008.

[103] S. Fratini and F. Guinea. Substrate-limited electron dynamics in graphene. *Phys. Rev. B*, 77:195415, May 2008.

[104] J Martin, N Akerman, G Ulbricht, T Lohmann, J H Smet, K von Klitzing, and A Yacoby. Observation of electron-hole puddles in graphene using a scanning single-electron transistor. *Nat Phys*, 4(2):144–148, feb 2008.

[105] Yuanbo Zhang, Victor W Brar, Caglar Girit, Alex Zettl, and Michael F Crommie. Origin of spatial charge inhomogeneity in graphene. *Nat Phys*, 5(10):722–726, October 2009.

[106] K.I. Bolotin, K.J. Sikes, Z. Jiang, M. Klima, G. Fudenberg, J. Hone, P. Kim, and H.L. Stormer. Ultrahigh electron mobility in suspended graphene. *Solid State Communications*, 146(910):351 – 355, 2008.

[107] CR Dean, AF Young, I. Meric, C. Lee, L. Wang, S. Sorgenfrei, K. Watanabe, T. Taniguchi, P. Kim, KL Shepard, et al. Boron nitride substrates for high-quality graphene electronics. *Nature nanotechnology*, 5(10):722–726, 2010.

[108] L. Wang, I. Meric, P. Y. Huang, Q. Gao, Y. Gao, H. Tran, T. Taniguchi, K. Watanabe, L. M. Campos, D. A. Muller, J. Guo, P. Kim, J. Hone, K. L. Shepard, and C. R. Dean. One-dimensional electrical contact to a two-dimensional material. *Science*, 342(6158):614–617, 2013.

[109] Douglas Hofstadter. Energy levels and wave functions of bloch electrons in rational and irrational magnetic fields. *Phys. Rev. B*, 14:2239–2249, Sep 1976.

[110] L. A. Ponomarenko, R. V. Gorbachev, G. L. Yu, D. C. Elias, R. Jalil, A. A. Patel, A. Mishchenko, A. S. Mayorov, C. R. Woods, J. R. Wallbank, M. Mucha-Kruczynski, B. A. Piot, M. Potemski, I. V. Grigorieva, K. S. Novoselov, F. Guinea, V. I. Falko, and A. K. Geim. Cloning of dirac fermions in graphene superlattices. *Nature*, 497:594, 2013.

[111] C. R. Dean, L. Wang, P. Maher, C. Forsythe, F. Ghahari, Y. Gao, J. Katoch, M. Ishigami, P. Moon, M. Koshino, T. Taniguchi, K. Watanabe, K. L. Shepard, J. Hone, and P. Kim. Hofstadters butterfly and the fractal quantum hall effect in moir superlattices. *Nature*, 497:598, 2013.

[112] B. Hunt, J. D. Sanchez-Yamagishi, A. F. Young, M. Yankowitz, B. J. LeRoy, K. Watanabe, T. Taniguchi, P. Moon, M. Koshino, P. Jarillo-Herrero, and R. C. Ashoori. Massive dirac fermions and hofstadter butterfly in a van der waals heterostructure. *Science*, 340(6139):1427–1430, 2013.

[113] C. Riedl, C. Coletti, T. Iwasaki, A. Zakharov, and U. Starke. Quasi-free-standing epitaxial graphene on sic obtained by hydrogen intercalation. *Phys. Rev. Lett.*, 103:246804, Dec 2009.

[114] Chun Hung Lui, Li Liu, Kin Fai Mak, George W Flynn, and Tony F Heinz. Ultraflat graphene. *Nature*, 462(7271):339–341, November 2009.

[115] Chih-Pin Lu, Guohong Li, K. Watanabe, T. Taniguchi, and Eva Y. Andrei. mos_2. *Phys. Rev. Lett.*, 113:156804, Oct 2014.

[116] Claire Berger, Zhimin Song, Xuebin Li, Xiaosong Wu, Nate Brown, Ccile Naud, Didier Mayou, Tianbo Li, Joanna Hass, Alexei N. Marchenkov, Edward H. Conrad, Phillip N. First, and Walt A. de Heer. Electronic confinement and coherence in patterned epitaxial graphene. *Science*, 312(5777):1191–1196, 2006.

[117] Peter W Sutter, Jan-Ingo Flege, and Eli A Sutter. Epitaxial graphene on ruthenium. *Nat Mater*, 7(5):406–411, May 2008.

[118] Qingkai Yu, Jie Lian, Sujitra Siriponglert, Hao Li, Yong P. Chen, and Shin-Shem Pei. Graphene segregated on ni surfaces and transferred to insulators. *Applied Physics Letters*, 93(11):–, 2008.

[119] Keun Soo Kim, Yue Zhao, Houk Jang, Sang Yoon Lee, Jong Min Kim, Kwang S Kim, Jong-Hyun Ahn, Philip Kim, Jae-Young Choi, and Byung Hee Hong. Large-scale pattern growth of graphene films for stretchable transparent electrodes. *Nature*, 457(7230):706–710, February 2009.

[120] Alfonso Reina, Xiaoting Jia, John Ho, Daniel Nezich, Hyungbin Son, Vladimir Bulovic, Mildred S. Dresselhaus, and Jing Kong. Large area, few-layer graphene films on arbitrary substrates by chemical vapor deposition. *Nano Letters*, 9(1):30–35, 2009. PMID: 19046078.

[121] Cecilia Mattevi, Hokwon Kim, and Manish Chhowalla. A review of chemical vapour deposition of graphene on copper. *J. Mater. Chem.*, 21:3324–3334, 2011.

[122] Xuesong Li, Yanwu Zhu, Weiwei Cai, Mark Borysiak, Boyang Han, David Chen, Richard D. Piner, Luigi Colombo, and Rodney S. Ruoff. Transfer of large-area graphene films for high-performance transparent conductive electrodes. *Nano Letters*, 9(12):4359–4363, 2009. PMID: 19845330.

[123] Xuesong Li, Carl W. Magnuson, Archana Venugopal, Rudolf M. Tromp, James B. Hannon, Eric M. Vogel, Luigi Colombo, and Rodney S. Ruoff. Large-area graphene single crystals grown by low-pressure chemical vapor deposition of methane on copper. *Journal of the American Chemical Society*, 133(9):2816–2819, 2011. PMID: 21309560.

[124] Yufeng Hao, M. S. Bharathi, Lei Wang, Yuanyue Liu, Hua Chen, Shu Nie, Xiaohan Wang, Harry Chou, Cheng Tan, Babak Fallahazad, H. Ramanarayan, Carl W. Magnuson, Emanuel Tutuc, Boris I. Yakobson, Kevin F. McCarty, Yong-Wei Zhang, Philip Kim, James Hone, Luigi Colombo, and Rodney S. Ruoff. The role of surface oxygen in the growth of large single-crystal graphene on copper. *Science*, 342(6159):720–723, 2013.

[125] Oleg V Yazyev and Yong P Chen. Polycrystalline graphene and other two-dimensional materials. *Nat Nano*, 9(10):755–767, October 2014.

[126] Daniel Huertas-Hernando, F. Guinea, and Arne Brataas. Spin-orbit coupling in curved graphene, fullerenes, nanotubes, and nanotube caps. *Phys. Rev. B*, 74:155426, Oct 2006.

[127] Hongki Min, J. E. Hill, N. A. Sinitsyn, B. R. Sahu, Leonard Kleinman, and A. H. MacDonald. Intrinsic and rashba spin-orbit interactions in graphene sheets. *Phys. Rev. B*, 74:165310, Oct 2006.

[128] Yugui Yao, Fei Ye, Xiao-Liang Qi, Shou-Cheng Zhang, and Zhong Fang. Spin-orbit gap of graphene: First-principles calculations. *Phys. Rev. B*, 75:041401, Jan 2007.

[129] Bjorn Trauzettel, Denis V Bulaev, Daniel Loss, and Guido Burkard. Spin qubits in graphene quantum dots. *Nat Phys*, 3(3):192–196, March 2007.

[130] M. Wojtaszek, I. J. Vera-Marun, E. Whiteway, M. Hilke, and B. J. van Wees. Absence of hyperfine effects in ^{13}c-graphene spin-valve devices. *Phys. Rev. B*, 89:035417, Jan 2014.

[131] Megumi Ohishi, Masashi Shiraishi, Ryo Nouchi, Takayuki Nozaki, Teruya Shinjo, and Yoshishige Suzuki. Spin injection into a graphene thin film at room temperature. *Japanese Journal of Applied Physics*, 46(7L):L605, 2007.

[132] W. H. Wang, K. Pi, Y. Li, Y. F. Chiang, P. Wei, J. Shi, and R. K. Kawakami. Magnetotransport properties of mesoscopic graphite spin valves. *Phys. Rev. B*, 77:020402, Jan 2008.

[133] E.W. Hill, A.K. Geim, K. Novoselov, F. Schedin, and P. Blake. Graphene spin valve devices. *Magnetics, IEEE Transactions on*, 42(10):2694–2696, Oct 2006.

[134] Sungjae Cho, Yung-Fu Chen, and Michael S. Fuhrer. Gate-tunable graphene spin valve. *Applied Physics Letters*, 91(12):–, 2007.

[135] C. Józsa, T. Maassen, M. Popinciuc, P. J. Zomer, A. Veligura, H. T. Jonkman, and B. J. van Wees. Linear scaling between momentum and spin scattering in graphene. *Phys. Rev. B*, 80:241403, Dec 2009.

[136] Wei Han and R. K. Kawakami. Spin relaxation in single-layer and bilayer graphene. *Phys. Rev. Lett.*, 107:047207, 2011.

[137] Wei Han, Jen-Ru Chen, Deqi Wang, Kathleen M. McCreary, Hua Wen, Adrian G. Swartz, Jing Shi, and Roland K. Kawakami. Spin relaxation in single-layer graphene with tunable mobility. *Nano Letters*, 12(7):3443–3447, 2012. PMID: 22725628.

[138] T.-Y. Yang, J. Balakrishnan, F. Volmer, A. Avsar, M. Jaiswal, J. Samm, S. R. Ali, A. Pachoud, M. Zeng, M. Popinciuc, G. Guntherodt, B. Beschoten, and B. Ozyilmaz. Observation of long spin-relaxation times in bilayer graphene at room temperature. *Phys. Rev. Lett.*, 107:047206, 2011.

[139] F. Volmer, M. Drögeler, E. Maynicke, N. von den Driesch, M. L. Boschen, G. Güntherodt, and B. Beschoten. Role of mgo barriers for spin and charge transport in co/mgo/graphene nonlocal spin-valve devices. *Phys. Rev. B*, 88:161405, Oct 2013.

[140] F. Volmer, M. Drögeler, E. Maynicke, N. von den Driesch, M. L. Boschen, G. Güntherodt, C. Stampfer, and B. Beschoten. Suppression of contact-induced spin dephasing in graphene/mgo/co spin-valve devices by successive oxygen treatments. *Phys. Rev. B*, 90:165403, Oct 2014.

[141] K. Pi, K. M. McCreary, W. Bao, Wei Han, Y. F. Chiang, Yan Li, S.-W. Tsai, C. N. Lau, and R. K. Kawakami. Electronic doping and scattering by transition metals on graphene. *Phys. Rev. B*, 80:075406, Aug 2009.

[142] Adrian G. Swartz, Jen-Ru Chen, Kathleen M. McCreary, Patrick M. Odenthal, Wei Han, and Roland K. Kawakami. Effect of in situ deposition of mg adatoms on spin relaxation in graphene. *Phys. Rev. B*, 87:075455, Feb 2013.

[143] Kathleen M. McCreary, Adrian G. Swartz, Wei Han, Jaroslav Fabian, and Roland K. Kawakami. Magnetic moment formation in graphene detected by scattering of pure spin currents. *Phys. Rev. Lett.*, 109:186604, Nov 2012.

[144] Jayakumar Balakrishnan, Gavin Kok Wai Koon, Manu Jaiswal, A H Castro Neto, and Barbaros Ozyilmaz. Colossal enhancement of spin-orbit coupling in weakly hydrogenated graphene. *Nat Phys*, 9(5):284–287, may 2013.

[145] C. Józsa, M. Popinciuc, N. Tombros, H. T. Jonkman, and B. J. van Wees. Controlling the efficiency of spin injection into graphene by carrier drift. *Phys. Rev. B*, 79:081402, Feb 2009.

[146] Wei Han, W. H. Wang, K. Pi, K. M. McCreary, W. Bao, Yan Li, F. Miao, C. N. Lau, and R. K. Kawakami. Electron-hole asymmetry of spin injection and transport in single-layer graphene. *Phys. Rev. Lett.*, 102:137205, Apr 2009.

[147] C. Józsa, M. Popinciuc, N. Tombros, H. Jonkman, and B. van Wees. Electronic spin drift in graphene field-effect transistors. *Phys. Rev. Lett.*, 100:236603, Jun 2008.

[148] Wei Han, K. Pi, W. Bao, K. M. McCreary, Yan Li, W. H. Wang, C. N. Lau, and R. K. Kawakami. Electrical detection of spin precession in single layer graphene spin valves with transparent contacts. *Applied Physics Letters*, 94(22):–, 2009.

[149] Adrian G. Swartz, Patrick M. Odenthal, Yufeng Hao, Rodney S. Ruoff, and Roland K. Kawakami. Integration of the ferromagnetic insulator euo onto graphene. *ACS Nano*, 6(11):10063–10069, 2012. PMID: 23083411.

[150] K. M. McCreary, K. Pi, A. G. Swartz, Wei Han, W. Bao, C. N. Lau, F. Guinea, M. I. Katsnelson, and R. K. Kawakami. Effect of cluster formation on graphene mobility. *Phys. Rev. B*, 81:115453, Mar 2010.

[151] W. H. Wang, W. Han, K. Pi, K. M. McCreary, F. Miao, W. Bao, C. N. Lau, and R. K. Kawakami. Growth of atomically smooth mgo films on graphene by molecular beam epitaxy. *Applied Physics Letters*, 93(18):–, 2008.

[152] Wei Han, K. M. McCreary, K. Pi, W. H. Wang, Yan Li, Hua Wen, and R. K. Kawakami. Spin transport and relaxation in graphene. *J. Magn. Magn. Mater.*, 324:369–381, 2012.

[153] M. Gmitra, S. Konschuh, C. Ertler, C. Ambrosch-Draxl, and J. Fabian. Band-structure topologies of graphene: Spin-orbit coupling effects from first principles. *Phys. Rev. B*, 80:235431, Dec 2009.

[154] J. Boettger and S. Trickey. First-principles calculation of the spin-orbit splitting in graphene. *Phys. Rev. B*, 75:121402, Mar 2007.

[155] Samir Abdelouahed, A. Ernst, J. Henk, I. Maznichenko, and I. Mertig. Spin-split electronic states in graphene: Effects due to lattice deformation, rashba effect, and adatoms by first principles. *Phys. Rev. B*, 82:125424, Sep 2010.

[156] R. J. Elliott. Theory of the effect of spin-orbit coupling on magnetic resonance in some semiconductors. *Phys. Rev.*, 96:266–279, Oct 1954.

[157] Y Yafet. g-factors and spin-lattice relaxation of conduction electrons. *Solid state physics*, 14:1–98, 1963.

[158] H. Ochoa, A. H. Castro Neto, and F. Guinea. Elliot-yafet mechanism in graphene. *Phys. Rev. Lett.*, 108:206808, May 2012.

[159] MI Dyakonov and VI Perel. Spin relaxation of conduction electrons in noncentrosymmetric semiconductors. *Soviet Physics Solid State, Ussr*, 13(12):3023–3026, 1972.

[160] T. Maassen, F. Dejene, M. Guimarães, C. Józsa, and B. van Wees. Comparison between charge and spin transport in few-layer graphene. *Phys. Rev. B*, 83:115410, Mar 2011.

[161] D. Huertas-Hernando, F. Guinea, and Arne Brataas. Spin-orbit-mediated spin relaxation in graphene. *Phys. Rev. Lett.*, 103:146801, Sep 2009.

[162] Dinh Van Tuan, Frank Ortmann, David Soriano, Sergio O Valenzuela, and Stephan Roche. Pseudospin-driven spin relaxation mechanism in graphene. *Nat Phys*, 10(11):857–863, November 2014.

[163] Denis Kochan, Martin Gmitra, and Jaroslav Fabian. Spin relaxation mechanism in graphene: Resonant scattering by magnetic impurities. *Phys. Rev. Lett.*, 112:116602, Mar 2014.

[164] A Avsar, J Y Tan, T Taychatanapat, J Balakrishnan, G K W Koon, Y Yeo, J Lahiri, A Carvalho, A S Rodin, E C T OFarrell, G Eda, A H Castro Neto, and B Özyilmaz. Spinorbit proximity effect in graphene. *Nat Commun*, 5, September 2014.

[165] Hua Wen, Tiancong Zhu, Yunqiu (Kelly) Luo, Walid Amamou, and Roland K. Kawakami. Current-based detection of nonlocal spin transport in graphene for spin-based logic applications. *Journal of Applied Physics*, 115(17):–, 2014.

[166] H. Dery, H. Wu, B. Cifcioglu, M. Huang, Y. Song, R. K. Kawakami, J. Shi, I. Krivorotov, I. Zutic, and L. J. Sham. Nanospintronics based on magnetologic gates. *IEEE Trans. Elec. Dev.*, 59:259, 2012.

[167] Wei Han, Roland K Kawakami, Martin Gmitra, and Jaroslav Fabian. Graphene spintronics. *Nat Nano*, 9(10):794–807, October 2014.

[168] Hanan Dery, Hui Wu, Berkehan Ciftcioglu, Michael Huang, Yang Song, Roland K. Kawakami, Jing Shi, Ilya N. Krivorotov, Donald A. Telesca, Igor uti, and Lu J. Sham. Reconfigurable nanoelectronics using graphene based spintronic logic gates. *Proc. SPIE*, 8100:81000W–81000W–11, 2011.

[169] M. H. D. Guimarães, P. J. Zomer, J. Ingla-Aynés, J. C. Brant, N. Tombros, and B. J. van Wees. Controlling spin relaxation in hexagonal bn-encapsulated graphene with a transverse electric field. *Phys. Rev. Lett.*, 113:086602, Aug 2014.

[170] R. P. Cowburn and M. E. Welland. Room temperature magnetic quantum cellular automata. *Science*, 287(5457):1466–1468, 2000.

[171] A. T. Hanbicki, R. Magno, S.-F. Cheng, Y. D. Park, A. S. Bracker, and B. T. Jonker. Nonvolatile reprogrammable logic elements using hybrid resonant tunneling diodegiant magnetoresistance circuits. *Applied Physics Letters*, 79(8):1190–1192, 2001.

[172] R. Richter, L. Br, J. Wecker, and G. Reiss. Nonvolatile field programmable spin-logic for reconfigurable computing. *Applied Physics Letters*, 80(7):1291–1293, 2002.

[173] A Ney, C Pampuch, R Koch, and K H Ploog. Programmable computing with a single magnetoresistive element. *Nature*, 425(6957):485–487, October 2003.

[174] A. Imre, G. Csaba, L. Ji, A. Orlov, G. H. Bernstein, and W. Porod. Majority logic gate for magnetic quantum-dot cellular automata. *Science*, 311(5758):205–208, 2006.

[175] Arne Brataas, Gerrit E.W. Bauer, and Paul J. Kelly. Non-collinear magnetoelectronics. *Physics Reports*, 427(4):157 – 255, 2006.

[176] Peng Xu, Ke Xia, Changzhi Gu, Ling Tang, Haifang Yang, and Junjie Li. An all-metallic logic gate based on current-driven domain wall motion. *Nat Nano*, 3(2):97–100, February 2008.

[177] Joohyung Bae, Kyung-Ho Kim, Jung-Min Han, Hyun Cheol Koo, Byoung-Chul Min, Hyung-jun Kim, Joonyeon Chang, Suk Hee Han, and Sang Ho Lim. Transport of perpendicular spin in a semiconductor channel via a fully electrical method. *Applied Physics Letters*, 102(6):–, 2013.

[178] Shwetha G Bhat and P S Anil Kumar. Room temperature electrical spin injection into GaAs by an oxide spin injector. *Sci. Rep.*, 4, July 2014.

[179] J.C. Slonczewski. Current-driven excitation of magnetic multilayers. *Journal of Magnetism and Magnetic Materials*, 159(12):L1 – L7, 1996.

[180] L. Berger. Emission of spin waves by a magnetic multilayer traversed by a current. *Phys. Rev. B*, 54:9353–9358, Oct 1996.

[181] J. A. Katine, F. J. Albert, R. A. Buhrman, E. B. Myers, and D. C. Ralph. Current-driven magnetization reversal and spin-wave excitations in co /cu /co pillars. *Phys. Rev. Lett.*, 84:3149–3152, Apr 2000.

[182] D.C. Ralph and M.D. Stiles. Spin transfer torques. *Journal of Magnetism and Magnetic Materials*, 320(7):1190 – 1216, 2008.

[183] H. Dery and L. J. Sham. Spin extraction theory and its relevance to spintronics. *Phys. Rev. Lett.*, 98:046602, Jan 2007.

[184] L. Cywiski, H. Dery, and L. J. Sham. Electric readout of magnetization dynamics in a ferromagnet-semiconductor system. *Applied Physics Letters*, 89(4):–, 2006.

[185] Gwan-Hyoung Lee, Young-Jun Yu, Changgu Lee, Cory Dean, Kenneth L. Shepard, Philip Kim, and James Hone. Electron tunneling through atomically flat and ultrathin hexagonal boron nitride. *Applied Physics Letters*, 99(24):–, 2011.

[186] Liam Britnell, Roman V. Gorbachev, Rashid Jalil, Branson D. Belle, Fred Schedin, Mikhail I. Katsnelson, Laurence Eaves, Sergey V. Morozov, Alexander S. Mayorov, Nuno M. R. Peres, Antonio H. Castro Neto, Jon Leist, Andre K. Geim, Leonid A. Ponomarenko, and Kostya S. Novoselov. Electron tunneling through ultrathin boron nitride crystalline barriers. *Nano Letters*, 12(3):1707–1710, 2012. PMID: 22380756.

[187] B. Dlubak, M.-B. Martin, C. Deranlot, K. Bouzehouane, S. Fusil, R. Mattana, F. Petroff, A. Anane, P. Seneor, and A. Fert. Homogeneous pinhole free 1nm al2o3 tunnel barriers on graphene. *Applied Physics Letters*, 101(20):–, 2012.

[188] Takehiro Yamaguchi, Yoshihisa Inoue, Satoru Masubuchi, Sei Morikawa, Masahiro Onuki, Kenji Watanabe, Takashi Taniguchi, Rai Moriya, and Tomoki Machida. Electrical spin injection into graphene through monolayer hexagonal boron nitride. *Applied Physics Express*, 6(7):073001, 2013.

[189] M Venkata Kamalakar, André Dankert, Johan Bergsten, Tommy Ive, and Saroj P Dash. Enhanced Tunnel Spin Injection into Graphene using Chemical Vapor Deposited Hexagonal Boron Nitride. *Sci. Rep.*, 4, August 2014.

[190] Wangyang Fu, Pter Makk, Romain Maurand, Matthias Bruninger, and Christian Schnenberger. Large-scale fabrication of bn tunnel barriers for graphene spintronics. *Journal of Applied Physics*, 116(7):–, 2014.

[191] M. Venkata Kamalakar, Andr Dankert, Johan Bergsten, Tommy Ive, and Saroj P. Dash. Spintronics with graphene-hexagonal boron nitride van der waals heterostructures. *Applied Physics Letters*, 105(21):–, 2014.

[192] Takehiro Yamaguchi, Satoru Masubuchi, Kazuyuki Iguchi, Rai Moriya, and Tomoki Machida. Tunnel spin injection into graphene using al2o3 barrier grown by atomic layer deposition on functionalized graphene surface. *Journal of Magnetism and Magnetic Materials*, 324(5):849 – 852, 2012.

[193] A. C. Ferrari, J. C. Meyer, V. Scardaci, C. Casiraghi, M. Lazzeri, F. Mauri, S. Piscanec, D. Jiang, K. S. Novoselov, S. Roth, and A. K. Geim. Raman spectrum of graphene and graphene layers. *Phys. Rev. Lett.*, 97:187401, Oct 2006.

[194] Rahul Rao, Ramakrishna Podila, Ryuichi Tsuchikawa, Jyoti Katoch, Derek Tishler, Apparao M. Rao, and Masa Ishigami. Effects of layer stacking on the combination raman modes in graphene. *ACS Nano*, 5(3):1594–1599, 2011.

[195] T. Kimura, Y. Otani, and J. Hamrle. Enhancement of spin accumulation in a nonmagnetic layer by reducing junction size. *Phys. Rev. B*, 73(4):132405, Apr 2006.

[196] Evan Sosenko, Huazhou Wei, and Vivek Aji. Effect of contacts on spin lifetime measurements in graphene. *Phys. Rev. B*, 89:245436, Jun 2014.

[197] P. J. Zomer, M. H. D. Guimarães, N. Tombros, and B. J. van Wees. Long-distance spin transport in high-mobility graphene on hexagonal boron nitride. *Phys. Rev. B*, 86:161416, Oct 2012.

[198] Maroun Khoury and David K. Ferry. Effect of molecular weight on poly(methyl methacrylate) resolution. *Journal of Vacuum Science & Technology B*, 14(1):75–79, 1996.

[199] Shazia Yasin, D.G. Hasko, and H. Ahmed. Comparison of mibk/ipa and water/ipa as pmma developers for electron beam nanolithography. *Microelectronic Engineering*, 6162(0):745 – 753, 2002. Micro- and Nano-Engineering 2001.

[200] Wei Chen and Haroon Ahmed. Fabrication of 57 nm wide etched lines in silicon using 100 kev electronbeam lithography and polymethylmethacrylate resist. *Applied Physics Letters*, 62(13):1499–1501, 1993.

[201] Wenchuang (Walter) Hu, Koshala Sarveswaran, Marya Lieberman, and Gary H. Bernstein. Sub-10 nm electron beam lithography using cold development of poly (methylmethacrylate). *Journal of Vacuum Science & Technology B*, 22(4):1711–1716, 2004.

[202] Masashi Shiraishi, Megumi Ohishi, Ryo Nouchi, Takayuki Nozaki, Teruya Shinjo, and Yoshishige Suzuki. Robustness of spin polarization in graphene-based spin valves. *Adv. Func. Mater.*, 19:1, 2009.

[203] H. Dery, L. Cywinski, and L. J. Sham. Spin transference and magnetoresistance amplification in a transistor. *Phys. Rev. B*, 73:161307(R), 2006.

[204] B. Behin-Aein, D. Datta, S. Salahuddin, and S. Datta. Proposal for an all-spin logic device with built-in memory. *Nature Nano.*, 5:266–270, 2010.

[205] J. Backus. Can programming be liberated from the von neumann style? a functional style and its algebra of programs. *Communications of the ACM*, 21:613, 1978.

[206] Piraux, L., Dubois, S., Fert, A., and Belliard, L. The temperature dependence of the perpendicular giant magnetoresistance in co/cu multilayered nanowires. *Eur. Phys. J. B*, 4(4):413–420, 1998.

[207] Jagadeesh S. Moodera and Lisa R. Kinder. Ferromagneticinsulatorferromagnetic tunneling: Spindependent tunneling and large magnetoresistance in trilayer junctions (invited). *Journal of Applied Physics*, 79(8):4724–4729, 1996.

[208] Jagadeesh S. Moodera, Janusz Nowak, and Rene J. M. van de Veerdonk. Interface magnetism and spin wave scattering in ferromagnet-insulator-ferromagnet tunnel junctions. *Phys. Rev. Lett.*, 80:2941–2944, Mar 1998.

[209] Yu Lu, X. W. Li, Gang Xiao, R. A. Altman, W. J. Gallagher, A. Marley, K. Roche, and S. Parkin. Bias voltage and temperature dependence of magnetotunneling effect. *Journal of Applied Physics*, 83(11):6515–6517, 1998.

[210] J. M. De Teresa, A. Barthélémy, A. Fert, J. P. Contour, R. Lyonnet, F. Montaigne, P. Seneor, and A. Vaurès. Inverse tunnel magnetoresistance in $\mathrm{Co}/\mathrm{srtio}_3/\mathrm{la}_{0.7}\mathrm{sr}_{0.3}\mathrm{mno}_3$: New ideas on spin-polarized tunneling. *Phys. Rev. Lett.*, 82:4288–4291, May 1999.

[211] Jose Maria De Teresa, Agns Barthlmy, Albert Fert, Jean Pierre Contour, Franois Montaigne, and Pierre Seneor. Role of metal-oxide interface in determining the spin polarization of magnetic tunnel junctions. *Science*, 286(5439):507–509, 1999.

[212] H. Boeve, E. Girgis, J. Schelten, J. De Boeck, and G. Borghs. Strongly reduced bias dependence in spintunnel junctions obtained by ultraviolet light assisted oxidation. *Applied Physics Letters*, 76(8):1048–1050, 2000.

[213] X. H. Xiang, T. Zhu, J. Du, G. Landry, and John Q. Xiao. Effects of density of states on bias dependence in magnetic tunnel junctions. *Phys. Rev. B*, 66:174407, Nov 2002.

[214] J. Moser, M. Zenger, C. Gerl, D. Schuh, R. Meier, P. Chen, G. Bayreuther, W. Wegscheider, D. Weiss, C.-H. Lai, R.-T. Huang, M. Kosuth, and H. Ebert. Bias dependent inversion of tunneling magnetoresistance in fegaasfe tunnel junctions. *Applied Physics Letters*, 89(16):–, 2006.

[215] M. Kohda, T. Kita, Y. Ohno, F. Matsukura, and H. Ohno. Bias voltage dependence of the electron spin injection studied in a three-terminal device based on a (ga,mn)asn+-gaas esaki diode. *Applied Physics Letters*, 89(1):–, 2006.

[216] Hitoshi Kubota, Akio Fukushima, Kay Yakushiji, Taro Nagahama, Shinji Yuasa, Koji Ando, Hiroki Maehara, Yoshinori Nagamine, Koji Tsunekawa, David D Djayaprawira, Naoki Watanabe, and Yoshishige Suzuki. Quantitative measurement of voltage dependence of spin-transfer torque in MgO-based magnetic tunnel junctions. *Nat Phys*, 4(1):37–41, jan 2008.

[217] S. O. Valenzuela, D. J. Monsma, C. M. Marcus, V. Narayanamurti, and M. Tinkham. Spin polarized tunneling at finite bias. *Phys. Rev. Lett.*, 94:196601, May 2005.

[218] S. A. Crooker, M. Furis, X. Lou, C. Adelmann, D. L. Smith, C. J. Palmstrm, and P. A. Crowell. Imaging spin transport in lateral ferromagnet/semiconductor structures. *Science*, 309(5744):2191–2195, 2005.

[219] M. C. Hickey, S. N. Holmes, T. Meng, I. Farrer, G. A. C. Jones, D. A. Ritchie, and M. Pepper. Strongly bias-dependent spin injection from fe into n-type gaas. *Phys. Rev. B*, 75:193204, May 2007.

[220] S. A. Crooker, E. S. Garlid, A. N. Chantis, D. L. Smith, K. S. M. Reddy, Q. O. Hu, T. Kondo, C. J. Palmstrøm, and P. A. Crowell. Bias-controlled sensitivity of ferromagnet/semiconductor electrical spin detectors. *Phys. Rev. B*, 80:041305, Jul 2009.

[221] M. Ciorga, A. Einwanger, U. Wurstbauer, D. Schuh, W. Wegscheider, and D. Weiss. Electrical spin injection and detection in lateral all-semiconductor devices. *Phys. Rev. B*, 79:165321, Apr 2009.

[222] B. Endres, F. Hoffmann, C. Wolf, A. Einwanger, M. Utz, D. Schuh, G. Woltersdorf, M. Ciorga, D. Weiss, C. H. Back, and G. Bayreuther. Bias dependence of spin injection into gaas from fe, feco, and (ga,mn)as contacts. *Journal of Applied Physics*, 109(7):–, 2011.

[223] Makoto Kameno, Yuichiro Ando, Eiji Shikoh, Teruya Shinjo, Tomoyuki Sasaki, Tohru Oikawa, Yoshishige Suzuki, Toshio Suzuki, and Masashi Shiraishi. Effect of spin drift on spin accumulation voltages in highly doped silicon. *Applied Physics Letters*, 101(12):–, 2012.

[224] Kazuya Muramoto, Masashi Shiraishi, Nobuhiko Mitoma, Takayuki Nozaki, Teruya Shinjo, and Yoshishige Suzuki. Analysis of degradation in graphene-based spin valves. *Applied Physics Express*, 2(12):123004, 2009.

[225] Athanasios N. Chantis, Kirill D. Belashchenko, Darryl L. Smith, Evgeny Y. Tsymbal, Mark van Schilfgaarde, and Robert C. Albers. Reversal of spin polarization in Fe/GaAs (001) driven by resonant surface states: First-principles calculations. *Phys. Rev. Lett.*, 99:196603, Nov 2007.

[226] Athanasios N. Chantis and Darryl L. Smith. Theory of electrical spin-detection at a ferromagnet/semiconductor interface. *Phys. Rev. B*, 78:235317, Dec 2008.

[227] D. L. Smith and P. P. Ruden. Spin-polarized tunneling through potential barriers at ferromagnetic metal/semiconductor schottky contacts. *Phys. Rev. B*, 78:125202, Sep 2008.

[228] Z. G. Yu and M. E. Flatte. Electric-field dependent spin diffusion and spin injection into semiconductors. *Phys. Rev. B*, 66:201202(R), 2002.

[229] Z. G. Yu, J. Baker, and S. Krishnamurthy. Transfer lengths and spin injection from a three-dimensional ferromagnet into graphene. *Phys. Rev. B*, 82:035425, Jul 2010.

[230] Francisco Batallan, Izio Rosenman, and C. B. Sommers. Band structure and fermi surface of hcp ferromagnetic cobalt. *Phys. Rev. B*, 11:545–557, Jan 1975.

[231] D. Bagayoko, A. Ziegler, and J. Callaway. Band structure of bcc cobalt. *Phys. Rev. B*, 27:7046–7049, Jun 1983.

[232] P. Laczkowski, L. Vila, V.-D. Nguyen, A. Marty, J.-P. Attané, H. Jaffrès, J.-M. George, and A. Fert. Enhancement of the spin signal in permalloy/gold multiterminal nanodevices by lateral confinement. *Phys. Rev. B*, 85:220404, Jun 2012.

[233] M. H. D. Guimares, P. J. Zomer, I. J. Vera-Marun, and B. J. van Wees. Spin-dependent quantum interference in nonlocal graphene spin valves. *Nano Letters*, 14(5):2952–2956, 2014. PMID: 24762101.

[234] Jian-Hao Chen, W. G. Cullen, C. Jang, M. S. Fuhrer, and E. D. Williams. Defect scattering in graphene. *Phys. Rev. Lett.*, 102:236805, Jun 2009.

[235] Gun-Do Lee, C. Wang, Euijoon Yoon, Nong-Moon Hwang, Doh-Yeon Kim, and K. Ho. Diffusion, coalescence, and reconstruction of vacancy defects in graphene layers. *Phys. Rev. Lett.*, 95:205501, Nov 2005.

[236] Jian-Hao Chen, Liang Li, William G Cullen, Ellen D Williams, and Michael S Fuhrer. Tunable Kondo effect in graphene with defects. *Nat Phys*, 7(7):535–538, jul 2011.

[237] Dacheng Wei, Yunqi Liu, Yu Wang, Hongliang Zhang, Liping Huang, and Gui Yu. Synthesis of n-doped graphene by chemical vapor deposition and its electrical properties. *Nano Letters*, 9(5):1752–1758, 2009. PMID: 19326921.

[238] Seung Jin Chae, Fethullah Gne, Ki Kang Kim, Eun Sung Kim, Gang Hee Han, Soo Min Kim, Hyeon-Jin Shin, Seon-Mi Yoon, Jae-Young Choi, Min Ho Park, Cheol Woong Yang, Didier Pribat, and Young Hee Lee. Synthesis of large-area graphene layers on poly-nickel substrate by chemical vapor deposition: Wrinkle formation. *Advanced Materials*, 21(22):2328–2333, 2009.

[239] Libo Gao, Wencai Ren, Huilong Xu, Li Jin, Zhenxing Wang, Teng Ma, Lai-Peng Ma, Zhiyong Zhang, Qiang Fu, Lian-Mao Peng, Xinhe Bao, and Hui-Ming Cheng. Repeated growth and bubbling transfer of graphene with millimetre-size single-crystal grains using platinum. *Nat Commun*, 3:699, Feb 2012.

[240] E Loginova, N C Bartelt, P J Feibelman, and K F McCarty. Factors influencing graphene growth on metal surfaces. *New Journal of Physics*, 11(6):063046, 2009.

[241] Johann Coraux, Alpha T N'Diaye, Martin Engler, Carsten Busse, Dirk Wall, Niemma Buckanie, Frank-J Meyer zu Heringdorf, Raoul van Gastel, Bene Poelsema, and Thomas Michely. Growth of graphene on ir(111). *New Journal of Physics*, 11(2):023006, 2009.

[242] Claire Berger, Zhimin Song, Tianbo Li, Xuebin Li, Asmerom Y. Ogbazghi, Rui Feng, Zhenting Dai, Alexei N. Marchenkov, Edward H. Conrad, Phillip N. First, and Walt A. de Heer. Ultrathin epitaxial graphite: 2d electron gas properties and a route toward graphene-based nanoelectronics. *The Journal of Physical Chemistry B*, 108(52):19912–19916, 2004.

[243] Konstantin V Emtsev, Aaron Bostwick, Karsten Horn, Johannes Jobst, Gary L Kellogg, Lothar Ley, Jessica L McChesney, Taisuke Ohta, Sergey A Reshanov, Jonas Rohrl, Eli Rotenberg, Andreas K Schmid, Daniel Waldmann, Heiko B Weber, and Thomas Seyller. Towards wafer-size graphene layers by atmospheric pressure graphitization of silicon carbide. *Nat Mater*, 8(3):203–207, March 2009.

[244] Jae-Hyun Lee, Eun Kyung Lee, Won-Jae Joo, Yamujin Jang, Byung-Sung Kim, Jae Young Lim, Soon-Hyung Choi, Sung Joon Ahn, Joung Real Ahn, Min-Ho Park, Cheol-Woong Yang, Byoung Lyong Choi, Sung-Woo Hwang, and Dongmok Whang. Wafer-scale growth of single-crystal monolayer graphene on reusable hydrogen-terminated germanium. *Science*, 344(6181):286–289, 2014.

[245] Sneha Gaddam, Cameron Bjelkevig, Siping Ge, Keisuke Fukutani, Peter A Dowben, and Jeffry A Kelber. Direct graphene growth on mgo: origin of the band gap. *Journal of Physics: Condensed Matter*, 23(7):072204, 2011.

[246] Jeonghyun Hwang, Virgil B. Shields, Christopher I. Thomas, Shriram Shivaraman, Dong Hao, Moonkyung Kim, Arthur R. Woll, Gary S. Tompa, and Michael G. Spencer. Epitaxial growth of graphitic carbon on c-face sic and sapphire by chemical vapor deposition (cvd). *Journal of Crystal Growth*, 312(21):3219 – 3224, 2010.

[247] Hui Bi, Shengrui Sun, Fuqiang Huang, Xiaoming Xie, and Mianheng Jiang. Direct growth of few-layer graphene films on sio2 substrates and their photovoltaic applications. *J. Mater. Chem.*, 22:411–416, 2012.

[248] Sungjin Park and Rodney S Ruoff. Chemical methods for the production of graphenes. *Nat Nano*, 4(4):217–224, April 2009.

[249] Xianfeng Zhang, Jing Ning, Xianglong Li, Bin Wang, Long Hao, Minghui Liang, Meihua Jin, and Linjie Zhi. Hydrogen-induced effects on the cvd growth of high-quality graphene structures. *Nanoscale*, 5:8363–8366, 2013.

[250] Joshua D. Wood, Scott W. Schmucker, Austin S. Lyons, Eric Pop, and Joseph W. Lyding. Effects of polycrystalline cu substrate on graphene growth by chemical vapor deposition. *Nano Letters*, 11(11):4547–4554, 2011. PMID: 21942318.

[251] Sreekar Bhaviripudi, Xiaoting Jia, Mildred S. Dresselhaus, and Jing Kong. Role of kinetic factors in chemical vapor deposition synthesis of uniform large area graphene using copper catalyst. *Nano Letters*, 10(10):4128–4133, 2010. PMID: 20812667.

[252] Ivan Vlassiouk, Murari Regmi, Pasquale Fulvio, Sheng Dai, Panos Datskos, Gyula Eres, and Sergei Smirnov. Role of hydrogen in chemical vapor deposition growth of large single-crystal graphene. *ACS Nano*, 5(7):6069–6076, 2011. PMID: 21707037.

[253] Xiuyun Zhang, Lu Wang, John Xin, Boris I. Yakobson, and Feng Ding. Role of hydrogen in graphene chemical vapor deposition growth on a copper surface. *Journal of the American Chemical Society*, 136(8):3040–3047, 2014. PMID: 24499486.

[254] Xuesong Li, Carl W. Magnuson, Archana Venugopal, Jinho An, Ji Won Suk, Boyang Han, Mark Borysiak, Weiwei Cai, Aruna Velamakanni, Yanwu Zhu, Lianfeng Fu, Eric M. Vogel, Edgar Voelkl, Luigi Colombo, and Rodney S. Ruoff. Graphene films with large domain size by a two-step chemical vapor deposition process. *Nano Letters*, 10(11):4328–4334, 2010. PMID: 20957985.

[255] Ahmet Avsar, Tsung-Yeh Yang, Sukang Bae, Jayakumar Balakrishnan, Frank Volmer, Manu Jaiswal, Zheng Yi, Syed Rizwan Ali, Gernot Guntherodt, Byung Hee Hong, Bernd Beschoten, and Barbaros Ozyilmaz. Toward wafer scale fabrication of graphene based spin valve devices. *Nano Letters*, 11(6):2363–2368, 2011. PMID: 21563787.

[256] Jongweon Cho, Li Gao, Jifa Tian, Helin Cao, Wei Wu, Qingkai Yu, Esmeralda N. Yitamben, Brandon Fisher, Jeffrey R. Guest, Yong P. Chen, and Nathan P. Guisinger. Atomic-scale investigation of graphene grown on cu foil and the effects of thermal annealing. *ACS Nano*, 5(5):3607–3613, 2011. PMID: 21500843.